Interaction of Magnetic Field and Flow in the Outer Shells of Giant Planets

Thesis by

Junjun Liu

In Partial Fulfillment of the Requirements

for the Degree of

Doctor of Philosophy

California Institute of Technology

Pasadena, California

2006

(Submitted May 16, 2006)

Acknowledgements

It has been six years since I came to Caltech. I would like to express my gratitude to all the people I met during this period. It has been a great journey.

First of all, I am indebted to my advisor, Dave Stevenson, who guided me into this very interesting research area and has been extraordinarily supportive, inspiring and patient all these years. Under his support, I had the opportunity to attend the GFD summer school at Woods Hole in 2003 and Computational Fluid Mechanics summer school at Helmholtz Institute in 2004. Both of them are very beneficial.

I would like to thank my advisor, Peter Goldreich, for his mentorship, guidance, support and encouragement during my time at Caltech. His enthusiasm for science, his positive attitude for life, and his belief that his students are capable of anything, continue to inspire me.

I thank Andy Ingersoll for serving as my academic advisors through the years. Thank Mark Richardson for introducing me interesting projects related with Mars and many enjoyable conversations. Thank Yuk Yung for being my research advisor for the first two years. I thank my thesis advisory committee - Andy Ingersoll, Peter Goldreich, Tapio Schneider, Re'em Sari and Dave Stevenson for all the time and thoughts they devoted to my TAC meetings.

I must thank Mike Black for resolving my numerous computer problems and am very grateful for the care and support from the staff members, Leticia Calderon, Irma Black, Nora Oshima, Loreta Young.

I thank Sarah Stewart, Ashwin Vasavada, Anthony Toigo, Zhiming Kuang, Lori Fenton, Huiqun Wang, Antonin Bouchez, Shane Byrne, Xianglei Huang for help and discussions. I also thank my officemates, Ah-San Wong, Mao-Chang Liang, Shabari Basu, Jiafang Xiao, Dan Feldman, Nicholas Heavens and Michael Busch for many enjoyable moments.

I would like to thank my parents, Zhuguo and Shuqin, as well as my sister

Yuanyuan and my brother Dixun for their unconditional support and encouragements throughout the years of my education. I thank my daughter, Amy, for all the joy and love she brings to my life. Finally, I am very grateful for the love and support that my husband gave to me. Thank you, Lifeng, for being my husband and sharing the wonderful journey with me. It is them that this thesis is dedicated to.

Abstract

This study of the interaction of magnetic field and flow in the outer shells of giant planets consists of three parts.

Part one: The atmospheres of Jupiter and Saturn exhibit strong and stable zonal winds. Busse suggested that they might be the surface expression of deep flows on cylinders. However, the deep flow hypothesis experiences difficulty when account is taken of the electrical conductivity of molecular hydrogen as measured in shockwave experiments. The deep zonal flow of an electrically conducting fluid would produce a toroidal magnetic field, an associated poloidal electrical current, and Ohmic dissipation. In steady state, the total Ohmic dissipation cannot exceed the planet's net luminosity. If we assume that the observed zonal flow penetrates along cylinders until it is truncated to (near) zero at some spherical radius, the upper bound on Ohmic dissipation constrains this radius to be no smaller than 0.95 Jupiter radius and 0.87 Saturn radius. The truncation of the cylindrical flow in the convective envelope requires an appropriate force to break the Taylor-Proudman constraint. We have been unable to identify any plausible candidate. Thus we conclude that deep-seated cylindrical flows do not exist.

Part two: A fluid shell with sufficient electrical conductivity and azimuthal velocity shear outside of the dynamo generation region can attenuate the non-axisymmetric component of the magnetic field. However, the interaction of the axisymmetric component of the magnetic field and the zonal flow is able to reduce the magnitude of zonal flow. The dimensionless number characterizing this reduction is the Chandrasekhar number. The smaller Saturnian field may allow a larger velocity shear and a greater attenuation of the non-axisymmetric field, thereby providing a possible explanation for the nearly axisymmetric field.

Part three: Combining the study for the attenuation effect produced by the semi-conducting layer and the observation of the magnetic field by Galileo and Voyager,

we find the possible outer boundary of the dynamo generation zone is at 0.86 Jupiter radius. The magnetic fields generated in the outer shell are dictated by a length scale comparable to the scale height of electrical conductivity, which is much smaller than the radius of the planet.

Contents

List of Figures

Chapter 1   Introduction

Jupiter, Saturn, Uranus and Neptune are giant planets in our solar system. They are made of a fluid envelope and possibly a small dense central core. For Jupiter and Saturn, the fluid envelope is composed of hydrogen ($\sim 92\%$ atomic) and helium ($\sim 8\%$), and a small amount of heavy elements. For Uranus and Neptune, the fluid envelope may be divided into two layers: the gas layer, which is mainly composed of hydrogen and helium; and the ice layer, which is primarily made of "ices" including molecular species such as water, methane, and ammonia in the fluid state. In contrast to the terrestrial planets, the viscosity can be neglected in the fluid envelope.

The interiors of giant planets are expected to evolve with time from a high entropy, hot initial state to a low entropy, cold degenerate state. They have hot interiors and emit more energy than they absorb from the Sun (Guillot, 2005). The heat source is mainly gravitational-either in the form of primordial heat generated during the collapse leading to planetary formation, or in the form of outgoing differentiation of heavy material from light material. The heat from the interior can be transported through diffusion, radiation and convection. Since the opacity is too high for effective radiative transfer and the thermal diffusivity is too small for effective diffusion, thermal convection was identified to be the main transport mechanism (Hubbard, 1968). Furthermore, the presence of alkali metals ensures convective interiors (Burrows et al., 2000; Guillot et al., 2004; Guillot, 2005).

1.1   Main observation data

Table 1.1 indicates the characteristics of the gravitational fields and orbits for giant planets. The masses of the giant planets can be determined from their external gravity fields. Observation of the motions of their natural satellites gives their masses

with great accuracy: 317.834, 95.161, 14.538, 17.148 times the mass of the Earth for Jupiter, Saturn, Uranus, and Neptune, respectively (Campbell & Synnott, 1985; Campbell & Anderson, 1989; Anderson et al., 1987; Tyler et al., 1989). These four giant planets comprise about 99.5% of the planetary mass in our solar system.

The radii of the giant planets corresponding to the 1 bar pressure level are obtained by radio occultation experiments (Lindal et al., 1981, 1985; Lindal, 1992). Figure (1.1) shows their relative sizes. All four giant planets are relatively fast rotators, with periods of approximately 10 hours for Jupiter and Saturn and approximately 17 hours for Uranus and Neptune. For Jupiter, Uranus and Neptune, the rotation rate is taken to be the magnetic field rotation rate, which is tied to the deep interior (Dessler, 1983; Davies et al., 1986; Warwick et al., 1986, 1989). However, Saturn's observed magnetic field is nearly axisymmetric, which prevents a rotation rate determination by Pioneer 11. The flyby of Voyager I and II detected period Saturn's kilometric radio emission (SKR), which had led to a magnetically defined rotation period for that planet (Desch & Kaiser, 1981). Since then the SKR period has varied by 1% (Galopeau & Lecacheux, 2000) and is currently 10 hour 45 min 45 s (Gurnett et al., 2005). It is unclear that SKR emission really represents Saturn's rotation and the reason for the period drift between 1980-1981 and 1994-2000 is unknown.

The mean density $\bar{\rho}$ listed in table 1.1 provides an important constraint on internal composition. The $\bar{\rho}$ values for Jupiter and Saturn imply that hydrogen is the major constituent, whereas Uranus and Neptune require more dense constituents.

Table 1.2 shows the energy balance as determined from Voyager IRIS data (Pearl & Conrath, 1991). Jupiter, Saturn and Neptune are observed to emit significantly more energy than they receive from the Sun (see Table 1.2). The case of Uranus is less clear. Its intrinsic heat flux F_{int} is one to two orders of magnitude smaller than that of the other giant planets. However, detailed modeling by a radiative-convective equilibrium model to the thermal structure of Uranus' atmosphere sug-
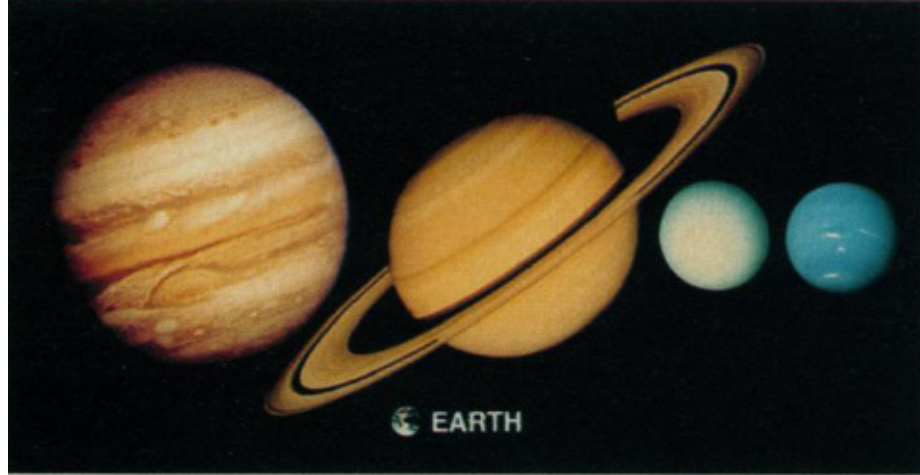
Figure 1.1 The relative size of four giant planets: Jupiter, Saturn, Uranus, and Neptune. Adapted from Ingersoll (1990).

Table 1.1.   Characteristics of the gravity fields and orbits.

Parameter, symbol	Jupiter	Saturn	Uranus	Neptune
Mass, $M(M_\oplus)$	317.834 [a]	95.161 [b]	14.538 [c]	17.148 [d]
Equatorial radius, r_e (10^3 km)	71.4 [e]	60.3 [f]	25.6 [g]	24.8 [g]
Equatorial gravity, g(m s^{-1})	22.9	9.1	8.8	11.1
Mean density, $\bar{\rho}$(g cm^{-3})	1.3275	0.6880	1.2704	1.6377
Rotation frequency, $\Omega(10^{-4}$ s)	3.57297(41) [h]	3.83577(47) [h]	6.206(4) [i]	5.800(20) [j]
Orbital period, $2\pi\Omega_o^{-1}$ (year)	11.9	29.5	84.0	164.8

[a]Campbell & Synott, 1995

[b]Campbell & Anderson, 1989

[c]Anderson et al., 1987

[d]Tyler et al., 1989

[e]Lindal et al., 1981

[f]Lindal et al., 1985

[g]Lindal, 1992

[h]Davis et al., 1986

[i]Warwick et al., 1986

[j]Warwick et al., 1989

Table 1.2. Energy balance as determined from Voyager IRIS data [a]

Parameter, symbol	Jupiter	Saturn	Uranus	Neptune
Absorbed power $[10^{23}$ erg s$^{-1}]$	50.14(248)	11.14(50)	0.526(37)	0.204(19)
Emitted power $[10^{23}$ erg s$^{-1}]$	83.65(84)	19.77(32)	0.560(11)	0.534(29)
Intrinsic power $[10^{23}$ erg s$^{-1}]$	33.5(26)	8.63(60)	0.034(38)	0.330(35)
Intrinsic flux [erg s^{-1} cm$^{-2}]$	5440.(430)	2010.(140)	42.(47)	433.(36)
Effective temperature [K]	124.4(3)	95.0(4)	59.1(3)	59.3(8)
1-bar temperature [b][K]	165.(5)	135.(5)	76.(2)	72.(2)

[a]Pearl & Conrath, 1991

[b]Lindal, 1992

gests that $F_{int} \geq 60$ erg cm^{-2} s^{-1} (Marley & McKay, 1999). Following this result, all four giant planets can be said to emit more energy than they receive from the Sun.

In the outer shells of giant planets, hydrogen (the dominant component) is supercritical, which indicates that there is no gas-liquid or gas-solid phase transition at that region. These planets have bottomless atmospheres, which is fundamentally different from terrestrial planets. The circulation in the atmosphere is powered by solar energy and internal energy left over from the formation of solar system. The observed zonal winds are very strong and stable. They reache ~ 100 m s^{-1} and ~ 400 m s^{-1} in the equatorial region of Jupiter and Saturn respectively. Uranus' zonal winds peak in the mid-latitude reaching ~ 200 m s^{-1}. Neptune's zonal flows peak in equatorial region reaching ~ 400 m s^{-1} (Ingersoll et al., 1995). The profiles of zonal (azimuthal) velocity versus latitude for all four giant planets are shown in figure (1.2).

Prograde equatorial jets have been observed for Jupiter and Saturn's equatorial region, whereas Uranus and Neptune have retrograde equatorial jets. At mid-latitudes, Jupiter's jets exhibit alternating prograde and retrograde bands, whereas Saturn's major jets are all prograde. Uranus and Neptune have smoother profiles than Jupiter or Saturn, and Neptune's winds are almost entirely retrograde (Ingersoll, 1990).

For the deep winds, the Galileo probe descended at $7.4°N$ on Jupiter and measured the speed from 0.4 to 22 bars. At the 0.4 bar level, the measured wind speed is 90 m s^{-1} (Atkinson et al., 1997, 1998). The velocity of winds increased with depth to 180 m s^{-1} and remained nearly constant until 22 bars. Although these measurements indicate that winds increase below the cloud level, they are not deep enough to reveal the vertical structure except for less than 1% of the planetary radius.

Giant planets have strong and complex magnetic fields. The observed dipole component of the surface field for Jupiter is about 4.2 G; and it is about 0.2 G for Saturn, Uranus and Neptune. The observed magnetic field is predominantly dipolar for Jupiter and Saturn. The tilt of the dipole relative to the rotation axis is on the order of 10° for Jupiter and near zero for Saturn. For Uranus and Neptune, the field is about equally dipole and quadrupole and the tilt of the dipole is 40°-60°, which demonstrates large variation on the surface (Connerney, 1993).

As in Earth, the observed magnetic field is generated in the high electrical conducting region. In the interiors of giant planets, the pressure and temperature increase with depth. Shockwave experiments have measured the electrical conductivity of hydrogen from 0.93 Mbar to 1.8 Mbar and an estimated temperature at 3000 Kelvin, representative of conditions inside Jupiter and Saturn (Nellis et al., 1996). Since hydrogen is expected to be in thermal equilibrium in this measurement, the results are applicable to the planetary interior. This experiment suggests that hydrogen undergoes a continuous transition from semi-conducting molecular state to metallic state as the pressure increases. The electrical conductivity increases exponentially to 2.0×10^5 S m^{-1} at 1.4Mbar where hydrogen becomes metallic. This conductivity of metallic hydrogen is one to two orders of magnitude lower than that of good metals (such as copper) at room temperature, and is about the lowest possible value for a metal. For Uranus and Neptune, measurements were made of electrical conductivity and equation of state of the planetary "ices": water, ammonia, methane
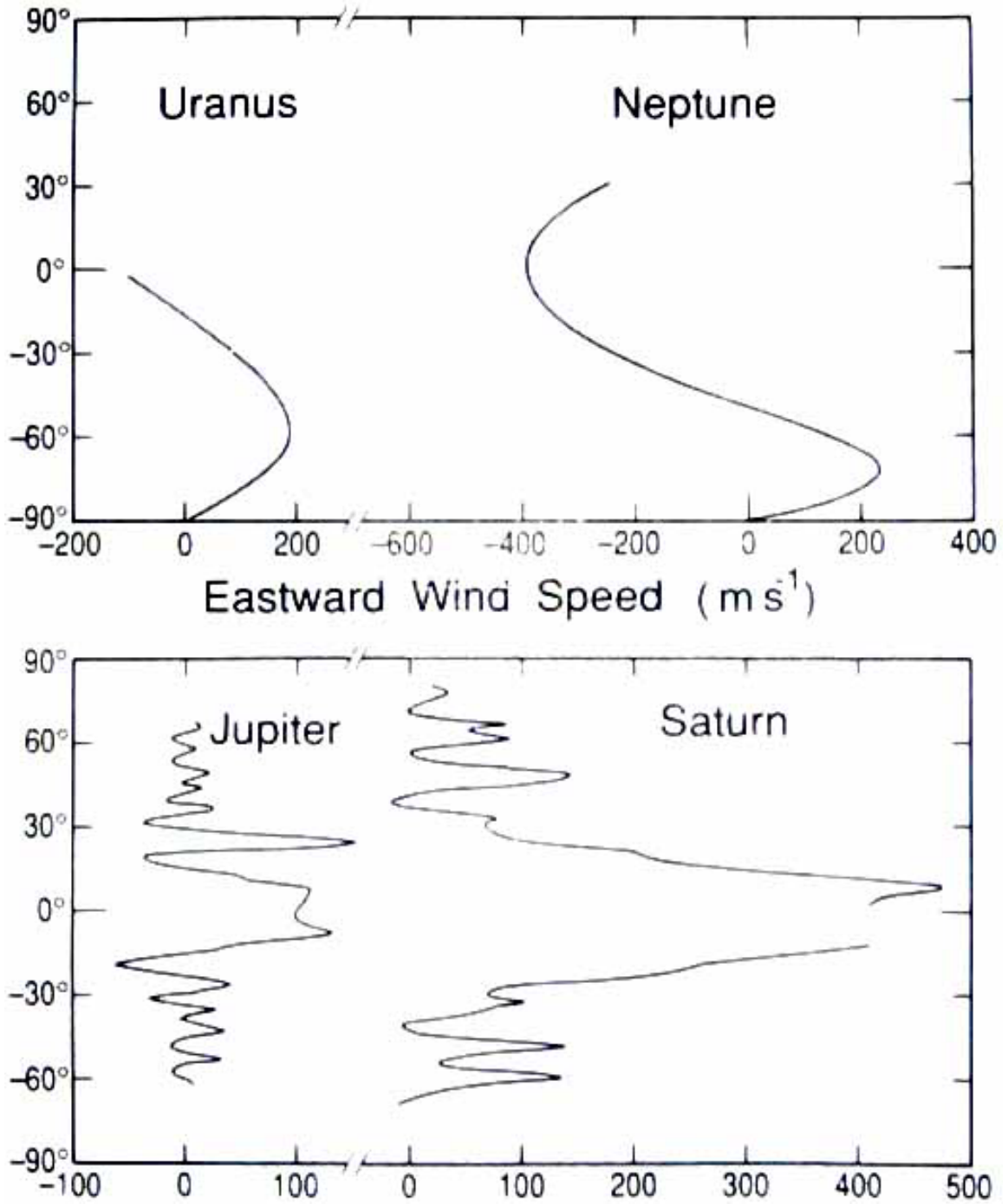
Figure 1.2 Zonal velocity versus latitude for all four giant planets. Velocity is measured relative to the planetary interiors, whose rotations are inferred from the periodic radio emissions. The measurements involve tracking cloud image sequences. Adapted from Ingersoll et al. (1995).

and "synthetic Uranus" at shock pressures and temperatures up to 75 GPa and 5000 K. The electrical conductivity increases with depth and reaches a constant value of 2×10^3 S m^{-1} above 40 GPa (Nellis et al., 1988).

For Jupiter, Uranus and Neptune, the magnitude of the wind speeds is determined relative to the planetary magnetic field, which is called System III (Dessler, 1983; Davies et al., 1986; Warwick et al., 1986, 1989). In the deep interior, the conductivity of metallic hydrogen is high, which implies the magnetic diffusivity is low. The magnetic field lines are fixed in the fluid and advected by the flow. The relative velocity between the magnetic field and the fluid is small, i.e., the magnetic field is nearly in a solid rotating state in this region. Comparing the measurements from Voyager and Galileo, the dipole tilt increases 0.3 deg and the magnitude of the dipole moment increases up to 1.5% over the period from 1975 to 2000 (Russell et al., 2001ab), inferring an upper bound for the relative velocity between the magnetic field and the flow in the deep interior to be about 0.1 cm s^{-1} (Guillot et al., 2004). For Saturn, the magnitude of the wind speeds is determined relative to SKR since Saturn's observed magnetic field is nearly axisymmetric (Desch & Kaiser, 1981).

1.2   Fundamental questions

How deep do the zonal winds extend? What are the possible generation mechanisms for the zonal winds? If the observed flow penetrates to the deep interior along the Taylor-Proudman cylinders as suggested by Busse (1976, 1983, 1994), the azimuthal flow will interact with the pre-existing poloidal magnetic field, produce toroidal magnetic field and the associated Ohmic dissipation. The total Ohmic dissipation cannot be larger than the planetary net luminosity, which gives a constraint for the maximum penetration depth of the zonal flow. The zonal wind has to be truncated before reaching the maximum penetration depth to avoid producing excessive Ohmic dissipation. By investigating the possible forces available to truncate the Taylor-Proudman col-

umn, we give a constraint for the depth of the zonal wind, as well as the generation mechanism.

On the other hand, the deeper and higher conductivity region would force the magnetic field lines to be almost fixed in the fluid and advected with the flow. The relative velocity between the fluid and the field is small. The magnetic field behaves like elastic strings. A large velocity between the fluid and magnetic field is not allowed since it produces large elastic stress acting on the fluid and reduces the velocity shear. Also, the velocity outside of the dynamo generation region is able to attenuate the temporal variation of the outgoing magnetic field, as well as the non-axisymmetric magnetic field. So, the following competing effects exist: The magnetic field is able to reduce the shear flow; and the shear flow is able to attenuate the temporal variation of the outgoing magnetic field and the non-axisymmetric magnetic field. Can the magnetically limited shear flow significantly attenuate the temporal variation of magnetic field and the non-axisymmetric magnetic field?

In this thesis, we explore the interaction of magnetic field and flow in the outer shells of giant planets. This study is motivated by the following fundamental questions:

1. Does the observed zonal flow penetrate to the deep interior along Taylor cylinders?

2. How does the interaction between the magnetic field and zonal flow change the Taylor cylinders?

3. Does the zonal flow attenuate the non-axisymmetric magnetic field? How?

4. Does the zonal flow attenuate the temporal variation of the outgoing magnetic field? How?

5. What are the characteristics of dynamo generation in a region with rapidly varying electrical conductivity?

Chapter 2   Electrical conductivity distribution in the interior of giant planets

2.1   Electrical conductivity distribution in the interior of Jupiter and Saturn

The electrical conductivity in the interiors of Jupiter and Saturn is due mainly to hydrogen. Near their surfaces it might be significantly enhanced relative to pure hydrogen by heavier elements because they are more readily ionized. Helium is unimportant due to its high ionization energy.

Condensed molecular hydrogen is a wide band-gap insulator at room temperature and pressure, with a band gap, E_g, of about 15 eV, corresponding to the ionization energy of the hydrogen molecule. As the pressure increases, this gap is expected to diminish and finally close to zero, resulting in an insulator-to-metal transition. In experiments, this transition appears to be gradual. As the energy gap closes, hydrogen molecules begin to dissociate to monatomic hydrogen and electrons start to be delocalized from H_2^+ ions (Nellis et al., 1996; Weir et al., 1996). The insulator-to-metal transition is expected to occur even though the hydrogen molecules have not been fully pressure-dissociated. At much higher pressure and temperature, molecular dissociation becomes complete and it is presumed that pure monatomic hydrogen forms a metallic Coulomb plasma (Stevenson & Ashcroft, 1974; Hubbard et al., 1997), but this is irrelevant to our analysis.

The conductivity of hydrogen has been measured in reverberating shockwave experiments in the following pressure ranges: from $0.93 - 1.8$ Mbar (Weir et. al., 1996)

and from $0.1 - 0.2$ Mbar (Nellis et al., 1992).[1] In these experiments, hydrogen is in thermal equilibrium at pressures and temperatures similar to those in the interiors of giant planets. From 0.93 to 1.8 Mbar, the measured electrical conductivity of hydrogen increases four orders of magnitude. Above 1.4 Mbar up to 1.8 Mbar, the conductivity is constant at 2×10^5 S m^{-1}, similar to that of liquid Cs and Rb at 2000 K and two orders of magnitude lower than that of a good metal (e.g., Cu) at room temperature. The constant conductivity suggests that the energy gap has been thermally smeared out (Weir et al., 1996). Temperatures of shock-compressed liquid hydrogen have been measured optically in separate experiments (Nellis et al., 1995; Holmes et al., 1995). At the highest obtained pressure of 0.83 Mbar, the measured temperature of 5200 K falls below that predicted for pure molecular hydrogen. This is due to the dissociation of molecular hydrogen and enables us to estimate the fractional dissociation as a function of pressure. At 1.4 Mbar and 3000 K, the dissociation fraction is $\sim 5\%$. Thus metallization of hydrogen occurs in the diatomic molecular phase and is caused by electrons delocalized from H$_2^+$ ions (Nellis et al., 1996; Ashcroft, 1968).

The electrical conductivity of a semiconductor can be expressed in the form:

$$\sigma = \sigma_0(\rho) \exp\left(-\frac{E_g(\rho)}{2K_B T}\right), \tag{2.1}$$

where σ is electrical conductivity, $E_g(\rho)$ is the energy of the density dependent mobility gap, K_B is Boltzmann constant, T is the temperature, and $\exp\left(-E_g/2K_B T\right)$ expresses the fractional occupancy of the current carrying states.

Between 0.2 Mbar and 1.8 Mbar, we adopt the electrical conductivity profile interpolated by Nellis et al. (1996) based on the experimental data. The relation between the energy gap and volume density is taken to be $E_g = 20.3 - 64.7\rho$, where E_g is in eV, ρ in mol cm^{-3}, and $\sigma_0 \approx 3.4 \times 10^{10} \exp(-44\rho)$ S m^{-1}. It is worth noting that

---

[1]The uncertainty in electrical conductivity is typically 25% but ranges up to 50% (Weir et al., 1996)

Nellis et al. (1996) calculate the conductivity profile along an isentrope of hydrogen starting from conditions deduced from observations of Jupiter's atmosphere, namely $T = 165$ K and $p = 1$ bar. This isentrope has the same entropy as one that has commonly been used to construct interior models of Jupiter (Guillot, 1999). However, it has a lower T for $p > 0.4$ Mbar because the one used in these models neglects the latent heat of hydrogen molecule dissociation (Nellis et al., 1995).[2] For consistency, we use the relation between conductivity and pressure obtained by Nellis et al. (1996). For some p, the σ based on the commonly used isentrope (Guillot, 1999) is about one order of magnitude different near the metallic conducting region and this difference diminishes towards the surface.

$E_g(\rho)$ has also been measured in shockwave experiments from 0.1 to 0.2 Mbar (Nellis et al., 1992). We can interpolate between these measurements of $E_g(\rho)$ and its value at ambient pressure and temperature using $\sigma_0 = 0.5 \times 10^8$ S m^{-1} (which gives the smooth connection of the conductivity measured in two pressure ranges) to extend the conductivity of hydrogen to the surface pressure level.

Based on the $p(r)$ from interior models of Jupiter and Saturn (Guillot, 1999) and $\sigma(p)$ from Nellis et al. (1996), we obtain the electrical conductivity of hydrogen as a function of radius (see figure 2.1). A clear signature of a smooth transition from the semi-conducting to metallic state (with $\sigma = 2 \times 10^5$ S m^{-1}) is observed at $0.84 R_J$ and $0.63 R_S$.

Figure (2.1) may underestimate the electrical conductivity at low pressure because it neglects the contribution from impurities. The electrical conductivity is proportional to the total number density of electrical charge carriers: $\sigma \propto n_e$, which includes

---

[2]Recent interior models of Jupiter and Saturn do account for this latent heat (Saumon & Guillot, 2004).
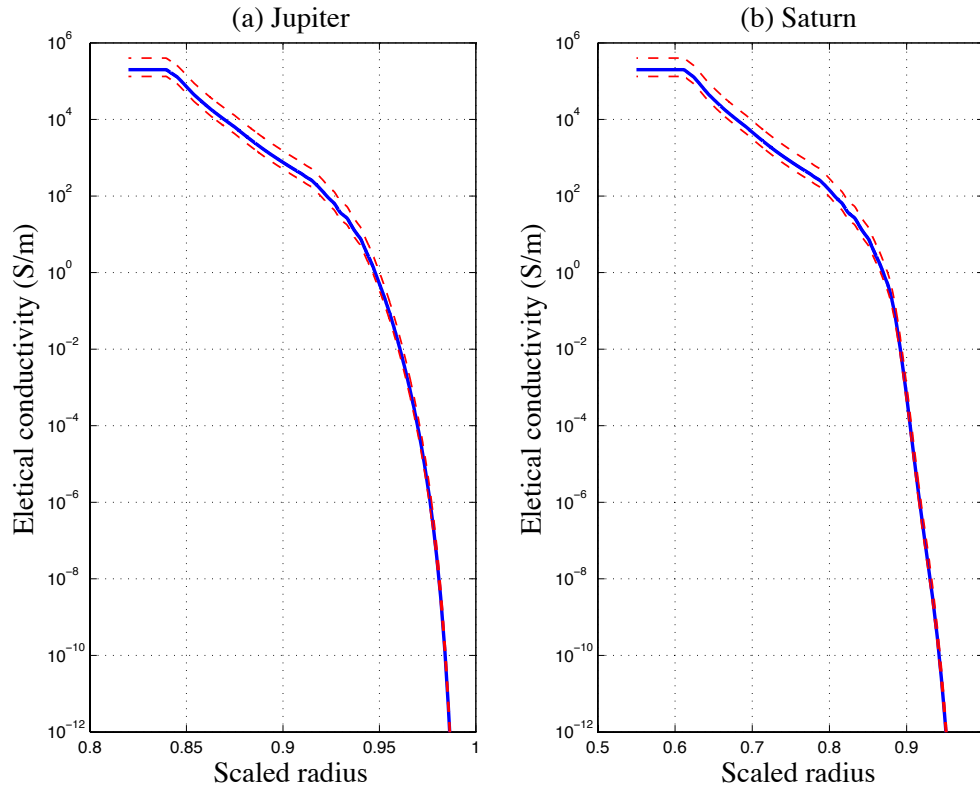
Figure 2.1 Electrical conductivity inside giant planets: (a) Jupiter; (b) Saturn. The solid line is the mean electrical conductivity of hydrogen and the dashed lines bound the range of uncertainty in the measurements. Additional uncertainties at the upper range of pressure arise from the difficulty of associating T and p as measured in the experiment with that inside the planet. Metallization is responsible for the plateau at 2×10^5 S m^{-1} which occurs near 0.84 R_J and 0.63 R_S.

a contribution from impurities x in addition to that from hydrogen:

$$n_e = n_{H_2} \exp\left(-\frac{E_g}{2K_BT}\right) + \sum_x n_x \exp\left(-\frac{E_x}{2K_BT}\right), \tag{2.2}$$

where n_x and E_x express the number density of the electrons and the energy gap due to an impurity. Alkali metals are sources of small band gap impurities. They may also contribute to the radiative opacity thus insuring adiabaticity (Guillot et al., 2004; Guillot, 2005). The mixing ratio of an alkali metal in the interior of a giant planet is presumably similar to that determined from its cosmic abundance. With these abundances, a band gap of a few electron volts would lead to a conductivity of $10^{-6} \sim 10^{-4}$ S m^{-1} at $T \sim 1000$ K, significantly above the value due to hydrogen.

In magnetohydrodynamics it is conventional to characterize the electrical conductivity σ in terms of the magnetic diffusivity $\lambda = (\mu_0\sigma)^{-1}$, where μ_0 is the magnetic permeability. Figure (2.1) shows that the electrical conductivity of hydrogen decreases exponentially outward from the metallic conducting region. Therefore, the magnetic diffusivity increases exponentially outward (see fig. 2.2) We will make use of the scale height of magnetic diffusivity,

$$H_\lambda(r) = \frac{\lambda(r)}{d\lambda(r)/dr}. \tag{2.3}$$

2.2 Electrical conductivity distribution in the interior of Uranus and Neptune

Estimations based on mass, radius, rotational rate, and gravity field of the planets indicate that Uranus and Neptune have similar internal structures (Stevenson, 1982). The planetary gravitational moments require that the density profiles outside the
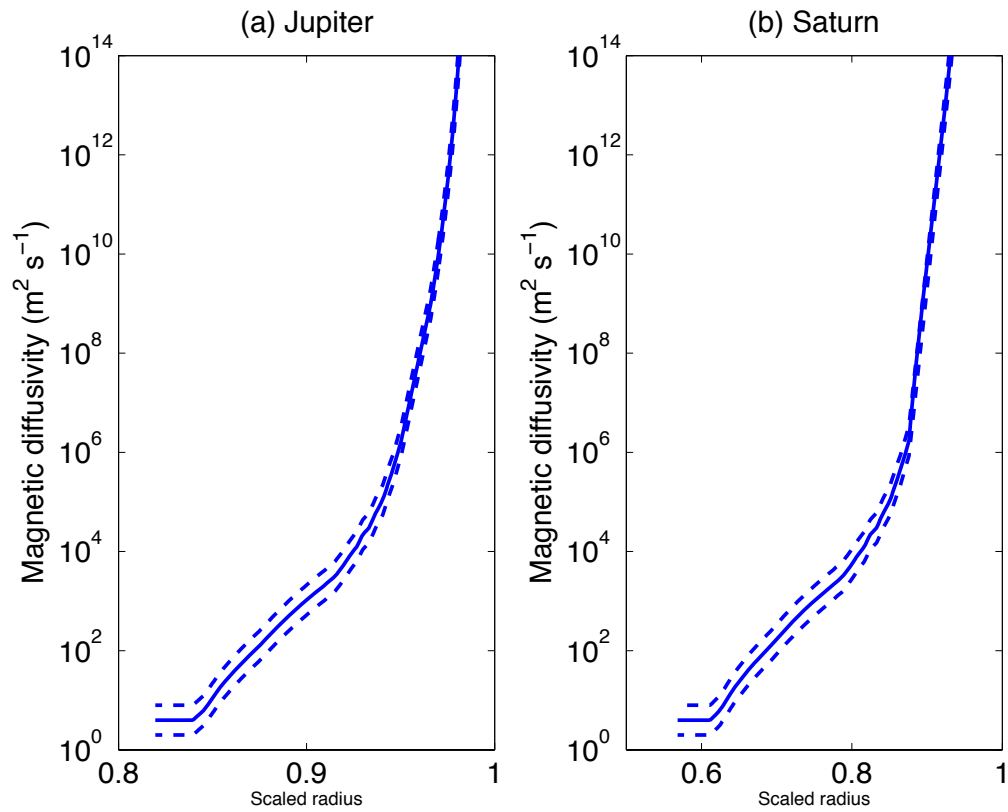
Figure 2.2 Magnetic diffusivity λ in the interiors of Jupiter and Saturn. (a) Jupiter; (b) Saturn. The magnetic diffusivity corresponding to the metallic state of hydrogen is 4 m s^{-2}.
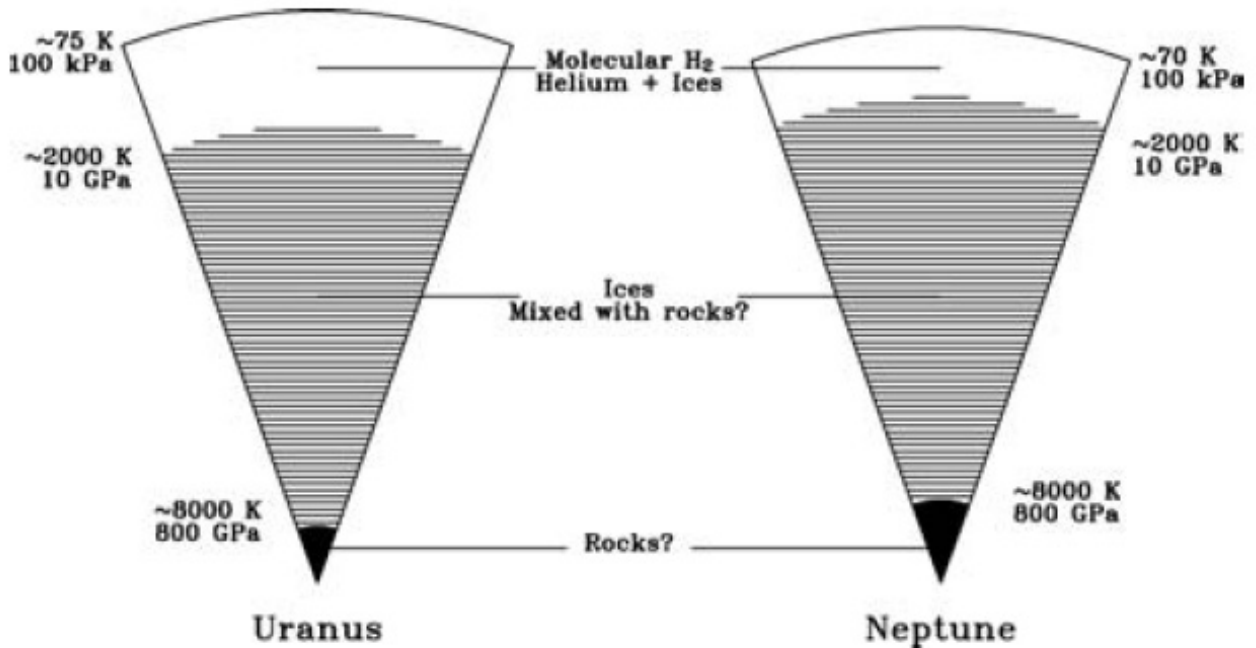
Figure 2.3 The interiors of Uranus and Neptune, adapted from Guillot (2005).

core region lie close to that of ices (a mixture initially composed of H_2O, CH_4 and NH_3, which rapidly becomes an ionic fluid of uncertain chemical composition in the planetary interior), except in the outermost layers, which have a density closer to that of hydrogen and helium (Marley et al., 1995; Podolak et al., 2000). As illustrated in Figure (2.3), a three-layer model of Uranus and Neptune consists of a central rock core (magnesium-silicate and iron material), an ice layer, and a hydrogen-helium gas envelope (Podolak et al., 1991; Hubbard et al., 1995).

To interpret the origin of the planetary magnetic field, measurements were made of electrical conductivity and equation of state of the planetary "ices": water, ammonia, methane and "synthetic Uranus" at shock pressures and temperatures up to 75 Gpa and 5000 K (See fig. 2.4). The electrical conductivities of the planetary "ices" all approach a constant value of 2000 S m^{-1} above 40 GPa. This upper limit is only weakly sensitive to chemical species (Nellis et al., 1988). The high electrical conductivity of shock water, the major ice constituent, is caused by molecular ioniza-

tion. Above 20 GPa, water has been said to be totally ionized into OH^{-1} and H_3O^+. Using a classical conductivity model and a mean free path of a molecular dimension, the degree of dissociation of water has been estimated to be between 10% and 100% above 20 GPa and 1200 K (Nellis et al., 1988).

We calculate the electrical conductivity for the interior of Uranus and Neptune with a three-layer model (Hubbard et al., 1991). In this model, both Uranus and Neptune are assumed to have a central rocky core with chondritic bulk proportions of iron, oxygen, magnesium, and silicon. The intermediate envelope is composed of "ice", which "ice" is defined as a mixture of the molecules H_2O, CH_4, and NH_3 in solar proportions, and almost certainly in liquid phase because of elevated temperatures. The outer shell is mainly made of hydrogen and taken to have a pressure density relation appropriate to solar composition (or to solar composition with a small density enhancement) and at constant specific entropy with the entropy fixed to the value near 1-bar pressure at a temperature of 70 K. The transition radius between the intermediate "ice" layer and the outer gas envelope is taken to be $\sim$ 0.8 Uranus radius and $\sim$ 0.84 Neptune radius, respectively. In the intermediate "ice" layer, which ranges from $\sim$ 0.3Mbar at $\sim$ 3000 K to $\sim$ 6Mbar at $\sim$ 7000 K, we use the conductivity profile for water ice to approximately express the planetary conductivity profile. With $p(r)$ in Hubbard's model (Hubbard et al., 1991) and the conductivity profile of water ice $\sigma(p)$ (Mitchell and Nellis, 1982; Nellis et al., 1988), we obtain $\sigma(r)$ for the ice in Uranus and Neptune respectively. The outer "gas" envelope is mainly composed of hydrogen with a small amount of heavy elements. We mainly consider the influence of hydrogen and water ice to the total conductivity. In this case, the number density of the electrical charge carriers n_e can be written as

$$n_e = n_{H_2} \exp\left(-\frac{(E_g)_{H_2}}{2K_BT}\right) + n_{H_2O} \exp\left(-\frac{(E_g)_{H_2O}}{2K_BT}\right). \qquad (2.4)$$

Since the electrical conductivity is proportional to the number density of electrical charge carriers: $\sigma \propto n_e$, $\sigma(r)$ can be determined from $p(r)$, $\sigma(p)$ for hydrogen (Nellis
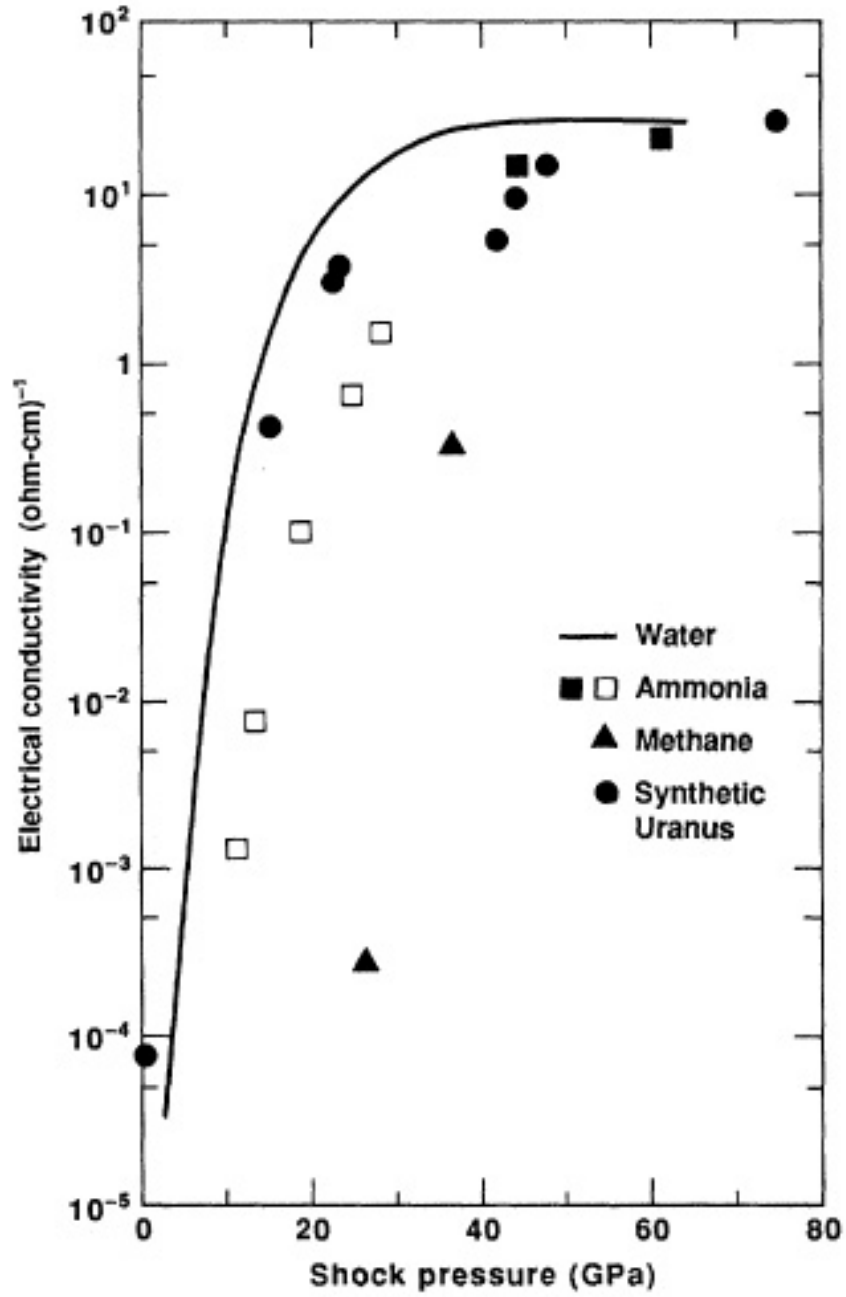
Figure 2.4 Electrical conductivity versus shock pressure for planetary "ices", adapted from (Nellis et al., 1988).

et al., 1996), and $\sigma(p)$ for water ice (Mitchell and Nellis, 1982; Nellis et al., 1988). The conductivity profile $\sigma(r)$ largely depends on the mixing ratio of water ice in the outer "gas" envelope. In figure (2.5), we demonstrate the conductivity profiles for a different assumption of the water ice mixing ratio range from 0% to 10%. If "ice" is present at 10% mixing ratio in the outer envelope, the electrical conductivity of material in the outer envelope is significantly increased by many orders of magnitude.

On the other hand, the mixing of hydrogen in the intermediate "ice" layer can significantly increase the electrical conductivity up to 100 times larger. In this thesis, we are mainly interested in the conductivity profile in the outer envelope of the planets. Therefore, we will not investigate the enhancement of electrical conductivity by mixing of hydrogen in the intermediate "ice" layer.
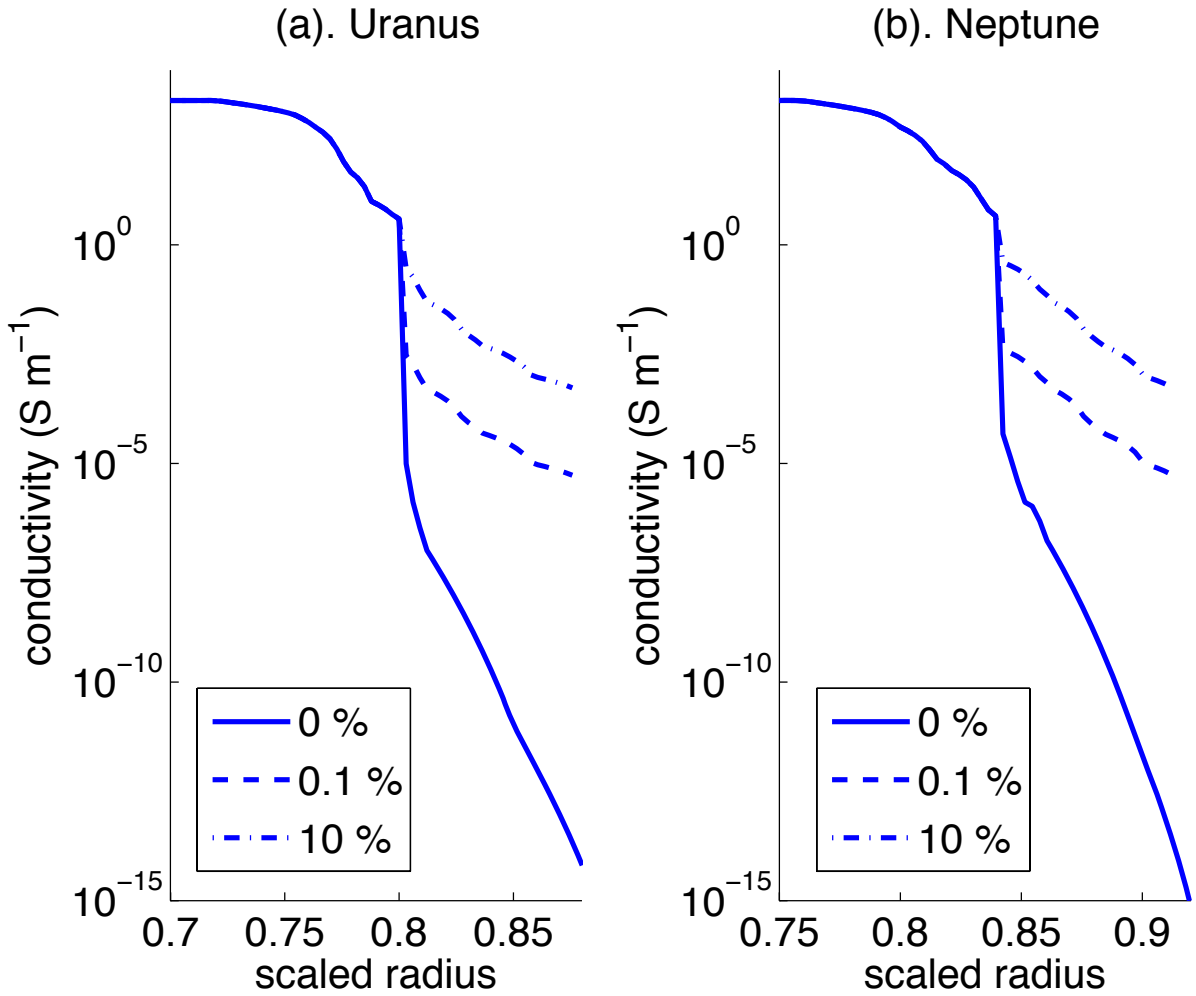
Figure 2.5 Conductivity profiles in the interior of Uranus and Neptune based on different "ice" mixing ratio in the outer "gas" envelope. (a) Uranus; (b) Neptune. The solid line corresponds to no "ice" in the outer "gas" envelope; the dash line represents 0.1% "ice" mixing ratio in the outer envelope; the dash-dot line expresses 10% "ice" mixing ratio in the outer envelope.

Chapter 3 Impossibility of deep-seated zonal winds in Jupiter and Saturn

3.1 Abstract

The atmospheres of Jupiter and Saturn exhibit strong (~ 100 m s^{-1}) and stable (over decadal time scales) zonal winds. Busse (1976, 1983, 1994) suggested that they might be the surface expression of deep flows on cylinders. Wind velocities deduced from the motion of the Galileo probe as it descended through Jupiter's atmosphere offer some support for Busse's suggestion. However, the deep flow hypothesis experiences difficulty when account is taken of the electrical conductivity of molecular hydrogen as measured in shockwave experiments. The deep zonal flow of an electrically conducting fluid would produce a toroidal magnetic field, an associated poloidal electrical current, and Ohmic dissipation. In steady state, the total Ohmic dissipation cannot exceed the planet's net luminosity. If we assume that the observed zonal flow penetrates along cylinders until it is truncated to (near) zero at some spherical radius, the upper bound on Ohmic dissipation constrains this radius to be no smaller than 0.95 of Jupiter's radius and 0.86 of Saturn's radius. At these radii, the electrical conductivity of hydrogen is about 0.1 S m^{-1}. The truncation of the cylindrical flow in the convective envelope requires an appropriate force to break the Taylor-Proudman constraint. We have been unable to identify any plausible candidate. The Lorentz force is much too weak. Although we lack a convincing model for turbulent convection, order of magnitude considerations suggest that both divergence of the Reynolds stress and the buoyancy force are also inadequate. Thus we conclude that deep-seated cylindrical flows do not exist. However, equatorial jets could maintain constant velocities on cylinders through the planet provided their half-widths were no greater than $\approx 21°$ for Jupiter and 31° for Saturn.

3.2   Introduction

Jupiter and Saturn are composed primarily of hydrogen and helium with small additions of heavier elements. Their atmospheres exhibit strong, stable zonal winds composed of multiple jets associated with azimuthal cloud bands (Ingersoll, 1990). Zonal winds peak in the equatorial region reaching $\sim$ 100 m s^{-1} on Jupiter and $\sim$ 400 m s^{-1} on Saturn.[1] The latitudes of Jupiter's jets have not changed for at least 80 years (Smith & Hunt, 1976) and their velocities have been constant within 10% over 25 years (Porco et al., 2003).

The depth of the zonal winds is unknown. Both deep and shallow flow models have been proposed. Wind speeds measured by the Galileo probe at $7.4°N$ on Jupiter increased from 90 m s^{-1} at 0.4 bar to 180 m s^{-1} at $\sim$ 5 bar and then remain nearly constant until 22 bar (Atkinson et al., 1997, 1998). It is important to bear in mind that these measurements only sample the winds in the outer 1% of the planet's radius. Where the electrical conductivity is high, the magnetic field lines are frozen into the fluid. Thus winds in these regions would cause changes in the external magnetic field. By comparing Galileo and Pioneer/Voyager data, Russell et al.(2001a,b) find that increases of 0.3 deg in the dipole tilt and 1.5% in the dipole moment may have taken place between 1975 and 2000. The former could be accounted for by meridional flow speeds on the order of 0.1 cm s^{-1} in the deep interior of Jupiter (Guillot et al., 2004).

Busse (Busse, 1976, 1983, 1994) advocates deep flows. Since Jupiter's interior is believed to be convective (Hubbard, 1968; Guillot et al., 2004), he asserts that the Taylor-Proudman theorem (Taylor, 1923) applies throughout the molecular hydrogen envelope. It follows that the zonal flows extend along cylinders centered on, and parallel to, the rotation axis, which terminates at the outer boundary of the metallic hydrogen core. Hydrogen is assumed to undergo a first order phase transition at the core-envelope boundary at which it abruptly changes from electrically insulating

---

[1]Wind speeds on Jupiter are determined relative to System III coordinates which rotate with the angular speed of the planet's magnetic field (Dessler, 1983).

to electrically conducting.[2] In Busse's model, the magnetic field is generated in the metallic core and passes through the molecular envelope without interaction. But data from shock wave experiments shows that hydrogen undergoes a continuous transition from a semi-conducting molecular state to a highly conducting metallic state as the pressure increases. This contradicts the assumption of a first order phase transition at the core-envelope boundary.

Recently, a modified deep flow model for Jovian zonal flows has been proposed based on simulations of convection in a thin shell with a lower boundary near $0.9R_J$ (Aurnou & Heimpel, 2004; Heimpel et al., 2005). The physical meaning of the lower boundary in the modified deep flow model is obscure. Hydrogen cannot undergo a phase change at that radius (Guillot et al., 2004). So how might the Taylor-Proudman constraint be violated in order to reduce the zonal flow to a near zero value below that boundary? We demonstrate later that the Lorentz force is much too weak to accomplish this.

In shallow flow models, the observed high-speed flow is confined to a thin, baroclinic layer near the cloud level; the interior flow is much slower. Even if the high velocity flow is confined to a shallow layer, its forcing may occur at depth. For example, if the flow were to arise from a process that conserved angular momentum per unit volume, ρU would be approximately conserved, where ρ is the density and U is the magnitude of the flow velocity. Since the density in the interior is several orders of magnitudes larger than that near the surface, the flow velocity could then be much greater near the surface. On the other hand, the observed zonal flow might be generated by shallow forcing due to the turbulence injected at the cloud level by moist convection, differential latitudinal solar heating, latent heat release from condensation of water, or other weather layer processes (Vasavada & Showman, 2005). From the thermal wind equation, a latitudinal temperature gradient of about $5\text{-}10K$

---

[2]In earlier models, this radius was estimated to be about $0.75R_J$ for Jupiter and $0.55R_S$ for Saturn (Zharkov & Trubitsyn, 1976; Stevenson & Salpeter, 1976).

across a few pressure scale heights below the cloud level would cause substantial vertical shear, which makes the flow velocity much greater near the surface than deeper down (Ingersoll & Cuzzi, 1969; Ingersoll et al., 1984; Vasavada & Showman, 2005).

In this paper, we examine the consequences of assuming a deep azimuthal flow consistent with the Taylor-Proudman theorem for an adiabatic interior. We calculate the total Ohmic dissipation associated with the flow and compare it to the planet's net luminosity. This constrains the depth to which the flow can extend. We consider two flow patterns, one in which the flow is truncated to zero at a spherical radius, and the other in which the flow is constant along the entire cylinder but confined to an equatorial jet.

3.3   Order of magnitude analysis

We use order of magnitude analysis to illustrate the relation between the total Ohmic dissipation and the planetary net luminosity. This clarifies the regime in which Jupiter and Saturn operate. Three characteristic velocities are: U, the magnitude of the observed zonal flow; $u_c = (F/\rho)^{1/3}$, a characteristic convective velocity based on the heat flux, F, and density, ρ; $u_B = \left(B_p^2/\mu_0\rho\right)^{1/2}$, a characteristic Alfven velocity based on the magnitude of the observed poloidal magnetic field, B_p. We note that the definition of the convective velocity does not take into account the influences of rotation and magnetic field.

Consider a zonal flow of amplitude U that extends to a depth $d_* = R - r_*$ and weakens below. Define the magnetic Reynolds number $R_m = UH_\lambda/\lambda$. The magnitude of the electrical field associated with the penetrating zonal flow is $\sim UB_p$ and the resulting current density is $\sim \sigma UB_p$. Thus we can estimate the magnitude of the toroidal field B_ϕ to be

$$B_\phi \sim \frac{UH_\lambda}{\lambda}B_p \sim R_m B_p. \qquad (3.1)$$

Since the magnitude of the flow below the penetration depth is several orders of magnitude smaller than U and the magnetic diffusivity is an exponential function of radius, the majority of the total Ohmic dissipation is generated within a spherical shell with thickness H_λ around the penetration depth. Thus the Ohmic dissipation per unit area is $H_\lambda \sigma U^2 B_p^2 \sim R_m U u_B^2 \rho$. Its ratio to the planet's heat flux

$$\Gamma \sim \frac{R_m U u_B^2 \rho}{F} = R_m \left(\frac{U}{u_c}\right) \left(\frac{u_B}{u_c}\right)^2 = R_m \frac{U B_p^2}{\mu_0 F} \tag{3.2}$$

is determined by the magnetic Reynolds number, R_m, and the observable quantities U, B, and F. The total Ohmic dissipation cannot exceed the planet's net luminosity. Thus the flow cannot penetrate below the radius at which $\Gamma \approx 1$. At the level where $R_m \sim 1$, Γ is independent of λ, H_λ and ρ. Can the surface zonal flow penetrate to this depth? For parameters appropriate to Jupiter and Saturn, the answer is no, as shown in figure (3.1). At the level where the total Ohmic dissipation matches the planet's net luminosity, $R_m \sim 0.05$ for Jupiter and $R_m \sim 0.5$ for Saturn.

3.4   Detailed formulation

The current density is

$$\mathbf{J} = \sigma \left(\mathbf{E} + \mathbf{U} \times \mathbf{B}\right), \tag{3.3}$$

where $\mathbf{E}$ is the electrical field in the reference frame in which $\mathbf{U}$ is measured. As discussed earlier, we take the reference frame to be fixed in the approximately uniformly rotating core of the planet.

We decompose the flow velocity $\mathbf{U}$ and the magnetic field $\mathbf{B}$ into the sum of poloidal and toroidal (ϕ) components: $\mathbf{U} = \mathbf{U}_P + \mathbf{U}_T$ and $\mathbf{B} = \mathbf{B}_P + \mathbf{B}_T$. Then

$$\mathbf{J} = \sigma \left(\mathbf{E} + \mathbf{U}_T \times \mathbf{B}_P + \mathbf{U}_P \times \mathbf{B}_T + \mathbf{U}_P \times \mathbf{B}_P\right), \tag{3.4}$$
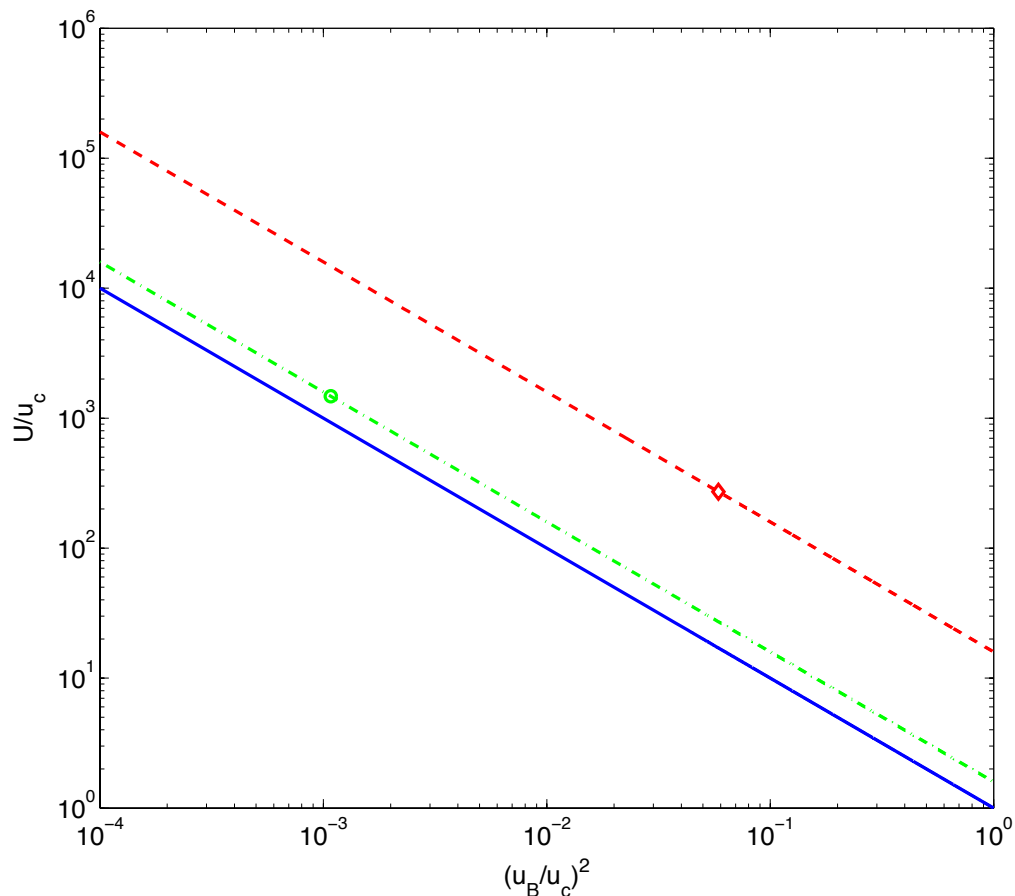
Figure 3.1 Plots of U/u_c versus $(u_B/u_c)^2$ for different values of Γ at the radius where $R_m = 1$. The solid line corresponds to $\Gamma = 1$, and the upper and lower dash lines correspond to value of $\Gamma \approx 20$ and $\Gamma \approx 2$ appropriate to Jupiter and Saturn. The diamond and circle correspond to values of U and u_B normalized by $u_c = (F/\rho)^{1/3}$, where ρ is evaluated at the layer where $R_m = 1$. For Jupiter, $U \sim 100$ m s^{-1}, $F \sim 5$ W m^{-2} and $B_p \sim 10$ G, so $\Gamma \sim 20$. For Saturn, $U \sim 400$ m s^{-1}, $F \sim 2$ W m^{-2} and $B_p \sim 1$ G, so $\Gamma \sim 2$.

where $\sigma \left(\mathbf{E} + \mathbf{U}_T \times \mathbf{B}_P + \mathbf{U}_P \times \mathbf{B}_T \right)$ and $\sigma \left(\mathbf{U}_P \times \mathbf{B}_P \right)$ are the poloidal and toroidal components of $\mathbf{J}$. Jupiter and Saturn are rotating rapidly so the large Coriolis force inhibits motions along the radial and latitudinal directions. Based on the mixing length estimation, the magnitude of the poloidal velocity field is about ~ 1 cm s^{-1} (Guillot et al., 2004), four orders of magnitude smaller than the observed zonal flow speeds ~ 100 m s^{-1}. Thus $|\mathbf{U}_P \times \mathbf{B}_P| \ll |\mathbf{U}_T \times \mathbf{B}_P|$.

Inside the planet, the poloidal magnetic field interacts with the toroidal component of the flow to produce a toroidal magnetic field with magnitude $|\mathbf{B}_T| \sim R_m |\mathbf{B}_P|$. Later we will discover that the magnetic Reynolds number is small $(R_m < 10)$ in the region of relevance to our investigation. So it is reasonable to assume that $|\mathbf{U}_P \times \mathbf{B}_T| \ll |\mathbf{U}_T \times \mathbf{B}_P|$, which implies

$$\mathbf{J} \approx \sigma \left(\mathbf{E} + \mathbf{U}_T \times \mathbf{B}_P \right) . \tag{3.5}$$

In steady state, the electrical field can be written as the gradient of the electrical potential; $\mathbf{E} = -\nabla \varphi$. Substituting this equation and the definition of magnetic diffusivity into equation (3.5), we arrive at

$$\mathbf{J} = \frac{1}{\mu_0 \lambda} \left(-\nabla \varphi + \mathbf{U}_T \times \mathbf{B}_P \right) . \tag{3.6}$$

The current density is divergence free,

$$\nabla \cdot \mathbf{J} = 0 . \tag{3.7}$$

Henceforth we asume that the magnetic field is axisymmetric. This approximation is not bad for Jupiter and quite good for Saturn. Jupiter's dipole tilt is about 10° and Saturn's is less than 0.1° (Connerney, 1993). Since we are concerned with Ohmic dissipation per unit volume P, which is proportional to the square of the magnitude of

the poloidal magnetic field: $P \propto |\mathbf{J}|^2 \propto |\mathbf{B}_P|^2$. Due to the orthogonality of spherical harmonics, a 10% contribution to the field from a dipole tilt gives two orders of magnitude less Ohmic dissipation. Substituting equation (3.6) into equation (3.7), and expanding in spherical coordinates (r, θ, ϕ), we obtain

$$
\frac{1}{r}\frac{\partial}{\partial r}\left[\frac{r^2}{\mu_0\lambda}\left(-\frac{\partial\varphi}{\partial r} + (\mathbf{U}_T \times \mathbf{B}_P)_r\right)\right]
$$
$$
+\frac{1}{r\sin(\theta)}\frac{\partial}{\partial\theta}\left[\frac{\sin(\theta)}{\mu_0\lambda}\left(-\frac{\partial\varphi}{\partial\theta} + (\mathbf{U}_T \times \mathbf{B}_P)_\theta\right)\right] = 0 \,. \tag{3.8}
$$

The magnetic diffusivity increases rapidly outward from the conducting core in the semi-conducting envelope. Therefore, the dominant term in equation (3.8) involves the radial derivative of the magnetic diffusivity. There are no other terms that can balance the magnitude of this term. Therefore,

$$
\frac{1}{\mu_0\lambda^2}\frac{d\lambda}{dr}\left(-\frac{\partial\varphi}{\partial r} + (\mathbf{U}_T \times \mathbf{B}_P)_r\right) \approx 0. \tag{3.9}
$$

As can be seen from equation (3.6), this relation implies that the radial component of the current density is much smaller that the θ component. Physically, this makes sense. The current that flows radially from deep regions is forced to flow meridionally in a thin layer, thereby having large amplitude. There is a close analogy to the standard meteorological scaling that ignores vertical motions relative to horizontal motions in a thin atmosphere. In other words, the rapid variation of magnetic diffusivity along the radial direction forces the current density to be dominant along the θ direction.

We can also obtain an expression for the electrical potential φ from equation (3.9)

$$
\frac{\partial\varphi}{\partial r} = (\mathbf{U}_T \times \mathbf{B}_P)_r \,. \tag{3.10}
$$

Integrating along the r-direction yields

$$\varphi = -\int_r^R \left(\mathbf{U}_T \times \mathbf{B}_P\right)_r dr' + Q(\theta), \qquad (3.11)$$

where R is the planetary radius and $Q(\theta)$ is an arbitrary function of θ. The electrical field in the θ direction can be written as

$$\mathbf{E}_\theta = -\frac{\partial \varphi}{\partial \theta} = \frac{1}{r}\left[\frac{\partial}{\partial \theta}\int_r^R \left(\mathbf{U}_T \times \mathbf{B}_P\right)_r dr' - \frac{dQ(\theta)}{d\theta}\right]. \qquad (3.12)$$

In the above equation (3.12), the first term in the parentheses is a function of both r and θ. However, the second term $Q'(\theta)$ is only a function of θ. These two terms cannot cancel each other at all radii.

From equation (3.6), we acquire the current density along the θ direction

$$\mathbf{J}_\theta = \frac{1}{\mu_0 \lambda} = \left(-\frac{\partial \varphi}{\partial \theta} + \left(\mathbf{U}_T \times \mathbf{B}_P\right)_\theta\right). \qquad (3.13)$$

Substituting the expression for the electrical potential into this equation, we obtain

$$\mathbf{J}_\theta = \frac{1}{\mu_0 \lambda r}\left[\frac{\partial}{\partial \theta}\int_r^R \left(\mathbf{U}_T \times \mathbf{B}_P\right)_r dr' + r\left(\mathbf{U}_T \times \mathbf{B}_P\right)_\theta - \frac{dQ}{d\theta}\right]. \qquad (3.14)$$

The Ohmic dissipation per unit volume, P, is equal to the square of the current density divided by the electric conductivity. Since the current along the θ direction is dominant,

$$P = \frac{J^2}{\sigma} \approx \frac{1}{\mu_0 \lambda r}\left[\frac{\partial}{\partial \theta}\int_r^R \left(\mathbf{U}_T \times \mathbf{B}_P\right)_r dr' + r\left(\mathbf{U}_T \times \mathbf{B}_P\right)_\theta - \frac{dQ}{d\theta}\right]^2. \qquad (3.15)$$

We note that P is inversely proportional to the magnetic diffusivity, λ, which increases exponentially outward from the metallic core with scale height $H_\lambda(r)$.

The total Ohmic dissipation cannot exceed the planet's net luminosity, L_{net}. Ap-

plying this constraint to a spherical shell of radius r and thickness $H_\lambda(r)$ yields

$$\left| \frac{\partial}{\partial \theta} \int_r^R (\mathbf{U}_T \times \mathbf{B}_P)_r \, dr' + r \, (\mathbf{U}_T \times \mathbf{B}_P)_\theta - \frac{dQ}{d\theta} \right| \leq \left(\frac{L_{net}\mu_0\lambda}{4\pi H_\lambda} \right)^{\frac{1}{2}} . \qquad (3.16)$$

Next we individually bound the magnitudes of $dQ/d\theta$ and the two terms that contain $\mathbf{U}_T \times \mathbf{B}_P$. Suppose these terms completely cancel at radius r_*. Across a layer of thickness $H_\lambda(r_*)$, $dQ/d\theta$ doesn't change whereas the other terms undergo fractional variations of order $H_\lambda(r_*)/r_*$. Therefore,

$$|Q'(\theta)| \leq \frac{r_*}{H_\lambda(r_*)} \left(\frac{L_{net}\mu_0\lambda(r_*)}{4\pi H_\lambda(r_*)} \right)^{1/2}, \qquad (3.17)$$

and

$$\left| \frac{\partial}{\partial \theta} \int_{r_*}^R (\mathbf{U}_T \times \mathbf{B}_P)_r \, dr' + r_* \, (\mathbf{U}_T \times \mathbf{B}_P)_\theta \right| \leq \frac{r_*}{H_\lambda(r_*)} \left(\frac{L_{net}\mu_0\lambda(r_*)}{4\pi H_\lambda(r_*)} \right)^{1/2} . \qquad (3.18)$$

Upper bounds on these individual terms are larger than that on their sum by a factor of $r/H_\lambda(r)$ (cf. equation [3.16]).

A tight upper bound can be placed on $|Q'(\theta)|$ by evaluating equation (3.17) near the top of the metallic core where $\lambda \sim 4$ m^2 s^{-1} and $H_\lambda \sim 1000$ km. We find $|Q'(\theta)| \leq 10^4$ Tesla m^2 s^{-1} for both Jupiter and Saturn. In a similar manner, we apply equation (3.18) to bound the zonal velocity at the top of the core finding $|\mathbf{U}_T| \leq 0.2$ m s^{-1} for Jupiter and $|\mathbf{U}_T| \leq 0.5$ m s^{-1} for Saturn.

Zonal wind speeds in the atmospheres of the giant planets reach ~ 100 m s^{-1}. Thus we can ignore the $Q'(\theta)$ term in equations (3.12), (3.14) and (3.15) when considering deep-seated winds that are constant on cylinders. Therefore,

$$\mathbf{J}_\theta(r, \theta) = \frac{1}{\mu_0\lambda} \left[\frac{1}{r} \frac{\partial}{\partial \theta} \int_r^R (\mathbf{U}_T \times \mathbf{B}_P)_r \, dr' + (\mathbf{U}_T \times \mathbf{B}_P)_\theta \right] . \qquad (3.19)$$

The first term is global; it orginates from the electrical field $\mathbf{E}$. The second term is

local. Estimated for the magnitudes of these terms read

$$\frac{1}{\mu_0 \lambda} \left[\frac{1}{r} \frac{\partial}{\partial \theta} \int_r^R (\mathbf{U}_T \times \mathbf{B}_P)_r \, dr' \right] \sim \frac{1}{\mu_0 \lambda} \frac{R - r}{r} |(\mathbf{U}_T \times \mathbf{B}_P)_r| \, , \qquad (3.20)$$

and

$$\frac{1}{\mu_0 \lambda} (\mathbf{U}_T \times \mathbf{B}_P)_\theta \sim \frac{1}{\mu_0 \lambda} |(\mathbf{U}_T \times \mathbf{B}_P)_\theta| \, , \qquad (3.21)$$

where $|(\mathbf{U}_T \times \mathbf{B}_P)_r|(R-r)/r \ll |\mathbf{U}_T \times \mathbf{B}_P|_\theta$, the current density is determined by the local term. Figure (3.2) displays current loops inside a sphere that are determined by the local interaction of a simple zonal flow and an axial dipole magnetic field.

From the current density distribution, we calculate the toroidal magnetic field $\mathbf{B}_T$ produced by the interaction of zonal flow with the poloidal magnetic field. Since the toroidal magnetic field external to the planet vanishes,

$$B_\phi = \frac{\mu_0}{r} \int_r^R J_\theta r' dr' \, . \qquad (3.22)$$

Substituting the equation (3.19) into equation (3.22), we obtain

$$B_\phi = \frac{1}{r} \int_r^R \frac{r' dr'}{\lambda(r')} \left[\frac{1}{r'} \frac{\partial}{\partial \theta} \int_{r'}^R (\mathbf{U}_T \times \mathbf{B}_P)_r \, dr'' + (\mathbf{U}_T \times \mathbf{B}_P)_\theta \right] \, . \qquad (3.23)$$

After we get the magnitude of the induced toroidal field, we can compare its magnitude with that of the pre-existing poloidal magnetic field.

Based on the expression for the current density (equation (3.19)), the total Ohmic dissipation reads

$$P_T = \frac{2\pi}{\mu_0} \int_0^R \frac{dr}{\lambda(r)} \int_0^\pi d\theta \sin(\theta) \left[\frac{\partial}{\partial \theta} \int_r^R (\mathbf{U}_T \times \mathbf{B}_P)_r \, dr' + r (\mathbf{U}_T \times \mathbf{B}_P)_\theta \right]^2 \, . \qquad (3.24)$$
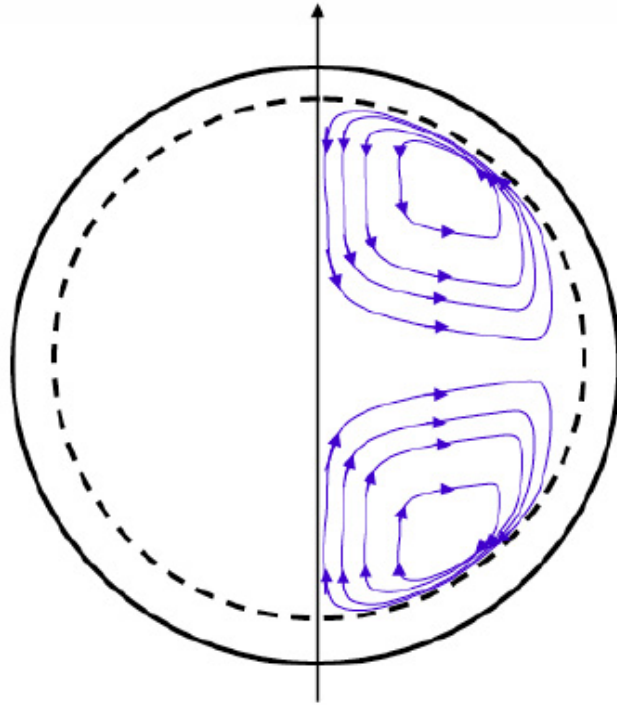
Figure 3.2 The current distribution inside the planets arising from the interaction of a simple zonal flow and a purely axial dipole field. In this illustration, the zonal flow goes to near zero just inside the dashed line. High current density corresponds to closely spaced current flow lines, and the conductivity is lower near the dashed line so that the Ohmic dissipation is predominantly near the dashed line despite the volume filling nature of the current.

3.5 Truncated zonal flows

3.5.1 Total Ohmic dissipation

In this section we assume that the atmospheric zonal flows observed on the giant planets (Porco et al., 2003, 2005) are constant on cylinders outside a spherical radius and vanish inside. Since these flows are not exactly N-S symmetric, we construct N-S symmetric profiles by reflecting the northern hemisphere zonal flow about the equator.[3] The magnetic fields of Jupiter and Saturn have been measured by various spacecrafts and fit by models dominated by a dipole plus smaller quadrupole and octupole components (Connerney, 1993). We adopt the axisymmetric part of these field models in our calculations. [4]

The total Ohmic dissipation calculated from equation (3.24) for Jupiter and Saturn is plotted against the cutoff radius in Figure (3.3). At the minimum cutoff radii of $0.95R_J$ and $0.87R_S$, the total Ohmic dissipation matches the planet's net luminosity. The magnetic diffusivity at the minimum cutoff radius is 2×10^6 m^2 s^{-1} for Jupiter and 1×10^6 m^2 s^{-1} for Saturn. By comparison, at the outer metallic core radii of $0.84R_J$ and $0.63R_S$, the magnetic diffusivity is at about 4 m^2 s^{-1}. As discussed in section 2.1, alkali metals or other impurities might raise the electrical conductivity in the outer envelope of a giant planet. This would decrease the maximum penetration depth.

The magnitudes of the induced toroidal magnetic field and the associated poloidal current are each inversely proportional to λ and thus increase inward. In figure (3.4) we display the toroidal magnetic field as a function of co-latitude at the maximum penetration depth. It reaches a magnitude of about 0.2 G for Jupiter and about 1.2 G for Saturn. Figure (3.5) shows the associated poloidal current density as a function

---

[3]We have verified that using the reflected southern hemisphere zonal flow makes a negligible difference to our results.

[4]In Appendix, we discuss the reasons for choosing these field models.
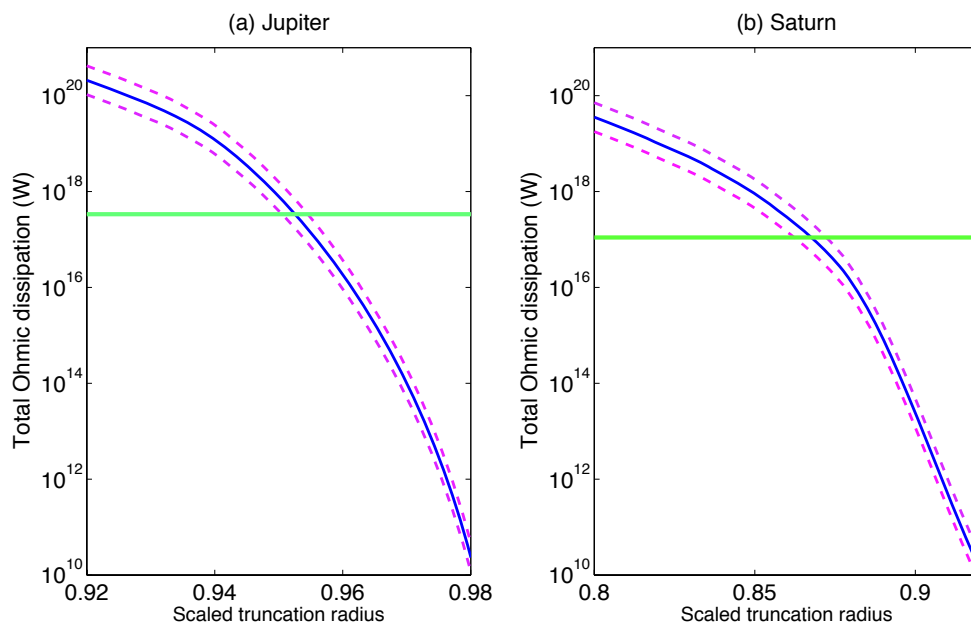
Figure 3.3 We assume that the observed zonal flow penetrates to the interior along cylinders until it is truncated at radius r. The blue curve depicts the total Ohmic dissipation as a function of the fractional truncation radius. The dashed curves indicate the range of uncertainty in the electrical conductivity of hydrogen at a given radius. The horizontal green lines marks to planet's net luminosity, which is 3.35×10^{17} W for Jupiter and 0.86×10^{17} W for Saturn (Guillot et al., 2004). The maximum penetration depth is determined by matching the total Ohmic dissipation to the net luminosity.
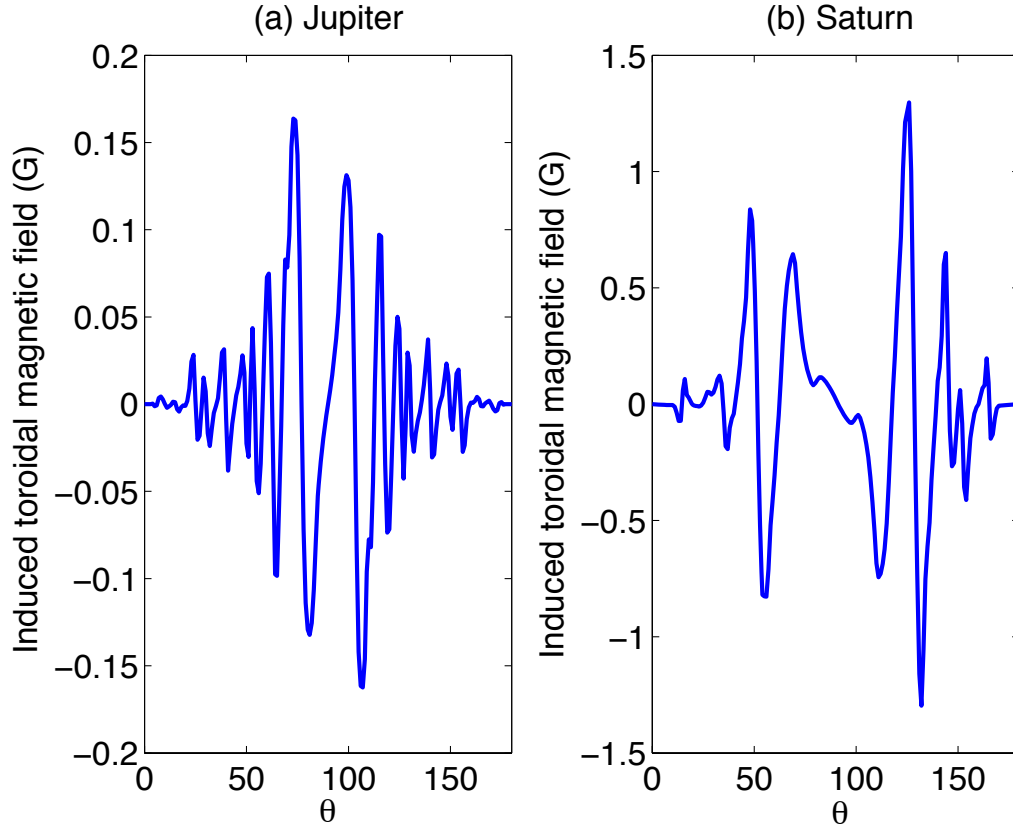
Figure 3.4 The induced toroidal magnetic field as a function of co-latitude at the maximum penetration depth: (a) Jupiter, (b) Saturn.

of co-latitude at the maximum penetration depth. It reaches a magnitude of about 3×10^{-3} A m^{-2} for Jupiter and about 0.015 A m^{-2} for Saturn.

3.5.2   Do deep-seated zonal flows exist?

Cylindrically penetrating zonal flows have to be truncated at some radius to avoid overproducing Ohmic dissipation. Here we investigate the necessary conditions for such a departure from the Taylor-Proudman state to take place.

The Navier-Stokes equation, which governs the motion of the fluid, reads

$$\frac{\partial \mathbf{U}}{\partial t} + (\mathbf{U} \cdot \nabla)\, \mathbf{U} + 2\Omega \mathbf{e}_z \times \mathbf{U} = -\frac{1}{\rho}\nabla p - \nabla \Phi_g + \frac{1}{\rho \mu_0}\, (\nabla \times \mathbf{B}) \times \mathbf{B} + \nabla \cdot \sigma_{vis}\,, \quad (3.25)$$
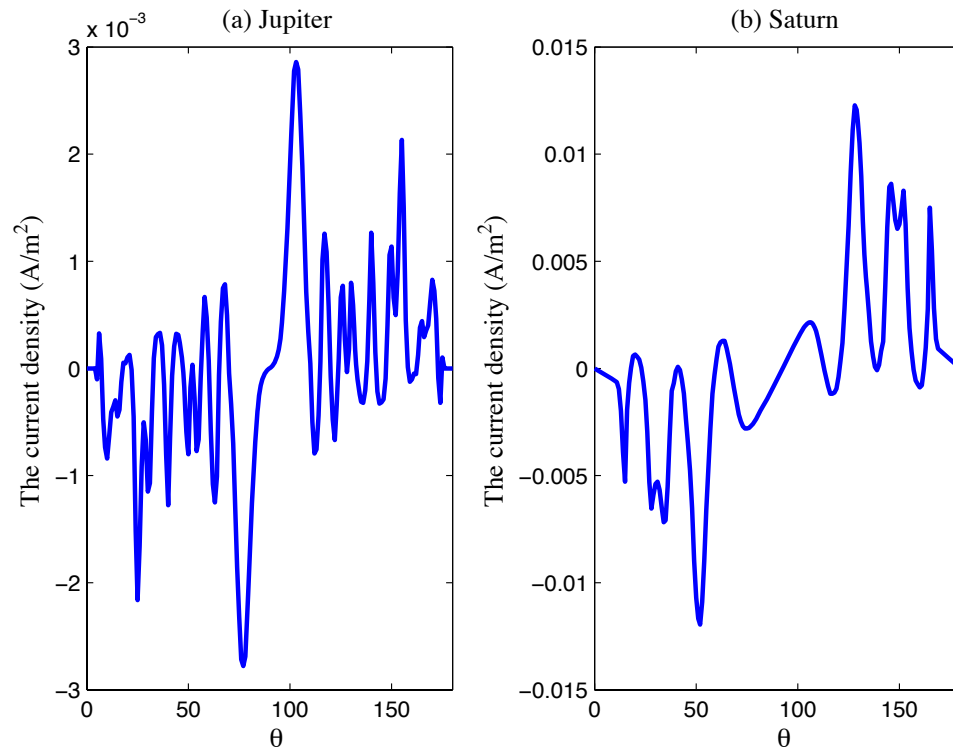
Figure 3.5 The poloidal current density as a function of co-latitude at the maximum penetration depth: (a) Jupiter, (b) Saturn.

where Ω is the (assumed) uniform angular velocity of the planet's metallic core, ρ is the density, p is the pressure, Φ_g is the gravitational plus centrifugal potential, and σ_{vis} is the viscous stress. Jupiter and Saturn are fast-rotating planets, so the Coriolis acceleration is large. Suppose we can neglect the accelerations due to the Maxwell, Reynolds, and viscous stresses. Then the Coriolis acceleration must be balanced by a combination of the accelerations due to the pressure and potential gradients. Thus

$$2\Omega\mathbf{e}_z \times \mathbf{U} = -\frac{1}{\rho}\nabla p - \nabla\Phi_g \,. \tag{3.26}$$

The net luminosity of the giant planets is believed to be transported outward by convection ensuring that their interiors are nearly compositionally uniform isentropes. For a compositionally uniform isentrope, the pressure is only a function of density: $p(\rho)$. Making this approximation and taking curl of equation (3.26), we obtain

$$\frac{\partial U_\phi}{\partial z} = 0 \,. \tag{3.27}$$

Thus, the zonal velocity is constant on cylinders parallel to the rotation axis. This is the Taylor-Proudman state. In previous sections, we have shown that the observed zonal flow cannot penetrate to below the radius at which the total Ohmic dissipation would match the planet's net luminosity. Next we consider causes of possible departures from the Taylor-Proudman state. In this section it proves convenient to work in cylindrical coordinates (ϖ, ϕ, z).

The Lorentz force cannot truncate the cylindrical flow

The induced toroidal magnetic field interacts with the poloidal magnetic field to produce the Lorentz force per unit mass

$$\mathbf{F}_{Lorentz} = \frac{\mathbf{J} \times \mathbf{B}}{\rho} = \frac{(\nabla \times \mathbf{B}) \times \mathbf{B}}{\mu_0 \rho} \,. \tag{3.28}$$

From the Navier-Stokes equation (3.25) and the expression for the Lorentz force, we find

$$2\Omega\frac{\partial U_\phi}{\partial z} = \frac{\partial}{\partial z}\left(\frac{1}{2\mu_0\rho\varpi^2}\frac{\partial}{\partial\varpi}\left(\varpi B_\phi\right)^2\right) . \tag{3.29}$$

Here the ϖ component of the Lorentz force comes from the gradient of the sum of the magnetic pressure plus the hoop stress from magnetic tension. We define by $\mathcal{R}$ the ratio of the right to the left hand side of the above equation. Lifting the z derivative from both sides, setting $\partial/\partial\varpi \sim 1/H_\lambda$, and expressing B_ϕ in terms of B_p using equation (3.1), we arrive at

$$\mathcal{R} \sim \frac{H_\lambda U_\phi}{\Omega\lambda^2}\frac{B_p^2}{\mu_0\rho} . \tag{3.30}$$

$\mathcal{R}$ is $\sim 10^{-4}$ for Jupiter and $\sim 10^{-5}$ for Saturn at the maximum penetration depth for their zonal flows. Moreover, it decreases rapidly outward, Thus the magnetic stress is incapable of truncating the zonal flow.

The Reynolds stress cannot truncate the cylindrical flow

In the order of magnitude analysis conducted in section 3, we introduce two characteristic flow amplitudes that differ by about four orders of magnitude: U, the magnitude of the observed zonal flow; and the much smaller $u_c = (F/\rho)^{1/3}$, a characteristic convective velocity based on the heat flux F and density ρ. In a planet with no magnetic field, it is possible for the Reynolds stress based on the small convective (fluctuating) velocity to excite a much larger stable zonal flow, since one could envisage that both excitation and dissipation are small. The smallness of Reynolds stress would then dictate the timescale for setting up or maintaining the zonal flow and not its amplitude. However, we are asking a different question here: Given the absence of any boundary layer at the appropriate place within the planet, can the variation in the Reynolds stress gradient (or along an axis parallel to the rotation axis) provide the change in the zonal flow from the observed large value in the atmosphere to the required low value in the magnetically coupled deep interior? In order for this to

be possible, we must suppose that the amplitude of the Reynolds stress gradient in the region where it is largest is of the same order of magnitude as the Coriolis force associated with the zonal flow, i.e.,

$$\frac{u^2}{l} \sim \Omega U. \tag{3.31}$$

Here u is the fluctuating component of the velocity field associated with the length scale l. Since turbulence is expected to be present and rotation-dominated convection can have highly dissimilar scales for motion in different directions, we cannot make a priori estimates of the scale l for which the Reynolds stress gradient is largest. We can nonetheless set bounds that demonstrate the implausibility of the hypothesis that equation (3.31) is satisfied.

Consider first the case where the motions are in the regime of rotation dominance where it is plausible that small-scale motions could feed large-scale zonal flow. This requires that $u < \Omega l$. Accordingly, $\Omega U \sim u^2/l < \Omega^2 l$ and $l > U/\Omega \sim 10^6$ m. Then from equation (3.31) it follows that u is at least 10^2 m s^{-1}, of the same order as U. We know of no way to satisfy this constraint, consistent with the buoyancy production (heat flow constraint). We recognize that this is a less rigorous argument than the main thesis of this paper since there is a fundamental difference between true dissipation (e.g., Ohmic dissipation) and the rate at which energy is transferred from one scale of motion to another. Nonetheless, one can appreciate the extraordinary difficulty of a fluctuating velocity of order U by comparing the heat flux F with ρU^3, the appropriate parameter of the same dimensions that one constructs from the velocity proposed. In Jupiter and Saturn, $\rho U^3/F \sim 10^8$ for the maximum penetration depth based on the Ohmic dissipation constraint. The enormity of this ratio makes the hypothesis $u^2/l \sim \Omega U$ implausible.

Consider now the case where the motions are not in the rotation-dominant regime. In this case, we have $u > \Omega l$ and expect that $\rho u^3/l \sim F/H$ where H is the local den-

sity scale height. Simultaneous solution with $u^2/l \sim \Omega U$ requires $u \sim F/(\rho U \Omega H) \sim 10^{-7}$ m s^{-1} and $l \sim 10^{-12}$ m. This is obviously impossible because l is smaller than molecular size. The underlying absurdity here is the enormous difference between the scales of motions that come from heat flow considerations and the actual observed zonal flow.

The buoyancy force might truncate the cylindrical flow

Taking the pressure to be a function of both density and entropy, $p = p(\rho, s)$, the pressure gradient can be written as

$$\nabla p = \left. \frac{\partial p}{\partial \rho} \right|_s \nabla \rho + \left. \frac{\partial p}{\partial s} \right|_\rho \nabla s . \tag{3.32}$$

Substituting the expression for ∇p into equation (3.26), taking a curl and dividing by 2Ω, we obtain

$$\frac{\partial U_\phi}{\partial z} = \frac{1}{2\Omega \rho^2} \left. \frac{\partial p}{\partial s} \right|_\rho (\nabla \rho \times \nabla s) \cdot \mathbf{e}_\phi . \tag{3.33}$$

From the thermodynamic identity

$$\left. \frac{\partial \rho}{\partial s} \right|_p \left. \frac{\partial s}{\partial p} \right|_\rho \left. \frac{\partial p}{\partial \rho} \right|_s = -1 , \tag{3.34}$$

it follows that

$$\left. \frac{\partial p}{\partial s} \right|_\rho = -c_s^2 \left. \frac{\partial \rho}{\partial s} \right|_p , \tag{3.35}$$

where c_s is the adiabatic sound speed. Given these relations, we can write the fractional change in U_ϕ over a density scale height $H_\rho \equiv -(\partial \ln \rho / \partial r)^{-1} \approx c_s^2/g$ as

$$\left| \frac{H_\rho}{U_\phi} \frac{\partial U_\phi}{\partial z} \right| = \frac{g}{2\Omega U_\phi} \left| \left. \frac{\partial \ln \rho}{\partial s} \right|_p H_\rho |\nabla s| \sin \delta . \right. \tag{3.36}$$

Here δ is the angle between $\nabla \rho$ and ∇s.

Convective interior

Because buoyancy drives convection, it might be thought that δ is small. However, this may not be the case. The photospheric effective temperature on Jupiter and Saturn is almost independent of latitude. This suggests that the convective heat flux is substantially deflected poleward of radial.

Next we apply mixing lengths arguments to bound $|\nabla s|$. This is uncertain territory. Our current understanding of turbulent convection is limited even for non-rotating systems. Rotation and especially strong differential rotation add additional complexity. We are guided by the analysis in Ingersoll & Pollard (1982). These authors consider two limiting cases.

Case 1: uniform rotation

In this case the analysis proceeds in a conventional fashion. The convective flux, F, and convective velocity, u, are expressed by

$$F \sim \rho u T \Delta s \sim \rho u T |\nabla s| L \,, \tag{3.37}$$

and

$$u^2 \sim g \frac{\Delta \rho}{\rho} L \sim g \left| \frac{\partial \ln \rho}{\partial s} \right|_p |\nabla s| L^2 \,. \tag{3.38}$$

Solving equations (3.37) and (3.38) for $|\nabla s|$ and substituting the result into equation (3.36) yields

$$\left| \frac{H_\rho}{U_\phi} \frac{\partial U_\phi}{\partial z} \right| \sim \frac{g}{2 \Omega U_\phi} \left(\frac{F}{\rho T c_s} \left| \frac{\partial \ln \rho}{\partial s} \right|_p \frac{H_\rho^2}{L^2} \right)^{2/3} \sin \delta \,. \tag{3.39}$$

Using equation (3.35) together with the Maxwell relation $(\partial p / \partial s)|_\rho = \rho^2 (\partial T / \partial \rho)|_s$,[5] we obtain

$$\left| \frac{\partial \ln \rho}{\partial s} \right|_p = \frac{T}{c_s^2} \left. \frac{\partial \ln T}{\partial \ln \rho} \right|_s = -\frac{\gamma T}{c_s^2} \,, \tag{3.40}$$

---

[5]Derived from the differential internal energy $dU = T ds + p d\rho / \rho^2$.

where γ is the dimensionless Gruneisen parameter. Thus

$$\left|\frac{H_\rho}{U_\phi}\frac{\partial U_\phi}{\partial z}\right| \sim \frac{g}{2\Omega U_\phi}\left(\frac{\gamma F}{\rho c_s^3}\frac{H_\rho^2}{L^2}\right)^{2/3}\sin\delta\,. \tag{3.41}$$

The Coriolis acceleration enters by restricting L to be less than the maximum value[6]

$$L^2 \leq \frac{uR}{\Omega}\,. \tag{3.42}$$

Ingersoll and Pollard (1982) argue that convection will maximize L. With this choice we may solve equations (3.37) and (3.38), along with equation (3.42), to determine L. Then substituting this value of L into equation (3.41), we arrive at

$$\left|\frac{H_\rho}{U_\phi}\frac{\partial U_\phi}{\partial z}\right| \sim \frac{g}{2\Omega U_\phi}\left(\frac{\gamma F}{\rho c_s^3}\frac{\Omega^2 H_\rho^3}{gR^2}\right)^{2/5}\sin\delta\,. \tag{3.43}$$

Numerical evaluation of the above expression is accomplished using data provided by Guillot (1999). There is only a weak radial dependence and at the maximum penetration depth

$$\left|\frac{H_\rho}{U_\phi}\frac{\partial U_\phi}{\partial z}\right| \sim 1.5\times10^{-5} \tag{3.44}$$

for Jupiter, and

$$\left|\frac{H_\rho}{U_\phi}\frac{\partial U_\phi}{\partial z}\right| \sim 4.0\times10^{-6} \tag{3.45}$$

for Saturn.

Case 2: differential rotation

This case is advocated by Ingersoll & Pollard (1982) for application to Jupiter and Saturn. Strong differential rotation stretches convective eddies azimuthally and curtails their radial extent. These details, although interesting, are irrelevant to our needs. All we require is an estimate for the magnitude of the entropy gradient. This

---

[6]This limitation is due to the energy barrier that buoyancy must surmount to effect the interchange of vortex tubes of different lengths.

turns out to satisfy the relation

$$g\left|\frac{\partial \ln \rho}{\partial s}\right|_p |\nabla s| \sim \left(\frac{\partial U_\phi}{\partial \varpi}\right)^2 . \tag{3.46}$$

Remarkably, $|\nabla s|$ is independent of the convective flux. Plugging this value for $|\nabla s|$ into equation (3.36) yields

$$\left|\frac{H_\rho}{U_\phi}\frac{\partial U_\phi}{\partial z}\right| \sim \frac{H_\rho}{2\Omega U_\phi}\left(\frac{\partial U_\phi}{\partial \varpi}\right)^2 \sin\delta . \tag{3.47}$$

At the maximum penetration depth, we have

$$\left|\frac{H_\rho}{U_\phi}\frac{\partial U_\phi}{\partial z}\right| \sim 0.6 \sin\delta \tag{3.48}$$

for Jupiter, and

$$\left|\frac{H_\rho}{U_\phi}\frac{\partial U_\phi}{\partial z}\right| \sim 0.3 \sin\delta \tag{3.49}$$

for Saturn. Buoyancy might produce a modest variation of U_ϕ in the convective interior if $\sin\delta$ is not small. However, it cannot truncate U_ϕ because $(\partial U_\phi/\partial z)_\varpi \propto U_\phi$.

Radiative atmosphere

We start from equation (3.36). Typically, s changes on the same scale as ρ in a radiative region, so we set $H_\rho|\nabla s| \sim k/\mu$. Moreover, since the perfect gas equation of state is a good approximation in the atmosphere, we have

$$\left|\frac{\partial \ln \rho}{\partial s}\right|_p = -\frac{(\gamma-1)}{\gamma}\frac{\mu}{k} , \tag{3.50}$$

where γ is the ratio of the specific heat at constant pressure to that at constant density. Thus

$$\left|\frac{H_\rho}{U_\phi}\frac{\partial U_\phi}{\partial z}\right| \sim \frac{g}{2\Omega U_\phi}\sin\delta . \tag{3.51}$$

We find

$$\left|\frac{H_\rho}{U_\phi}\frac{\partial U_\phi}{\partial z}\right| \sim 600 \sin\delta \tag{3.52}$$

for Jupiter, and

$$\left| \frac{H_\rho}{U_\phi} \frac{\partial U_\phi}{\partial z} \right| \sim 50 \sin \delta \tag{3.53}$$

for Saturn. Thus is appears that the Taylor-Proudman columns might be truncated in the radiative atmosphere.

3.5.3 Maximum width of an equatorial jet

A sufficiently narrow equatorial jet could maintain constant velocity on cylinders throughout the planet. For example, consider the specific velocity profile

$$U_\phi = U_0 \sin \left(\frac{\pi}{2} \frac{(\theta - \theta_0)}{(\pi/2 - \theta_0)} \right)^{\frac{1}{10}} \quad \text{if} \quad \theta < \pi - \theta_0 \tag{3.54}$$

and,

$$U_\phi = 0 \quad \text{if} \quad \theta < \theta_0 \quad \text{and} \quad \theta > \pi - \theta_0; \tag{3.55}$$

so the jet has equatorial velocity U_0 and angular half-width $\pi/2 - \theta_0$. For Jupiter and Saturn, U_0 is approximately 140 m s^{-1} and 400 m s^{-1}, respectively. Figure (3.6) displays the calculated Ohmic dissipation rate as a function of the jet half-width. The maximum half-width is about 21° for Jupiter and 31° for Saturn. There is an obvious relation between these maximum half-widths and the radii of maximum penetration, R_{mp}, calculated in §3.5.1, namely,

$$\cos \theta_0 \approx \frac{R_{mp}}{R} . \tag{3.56}$$
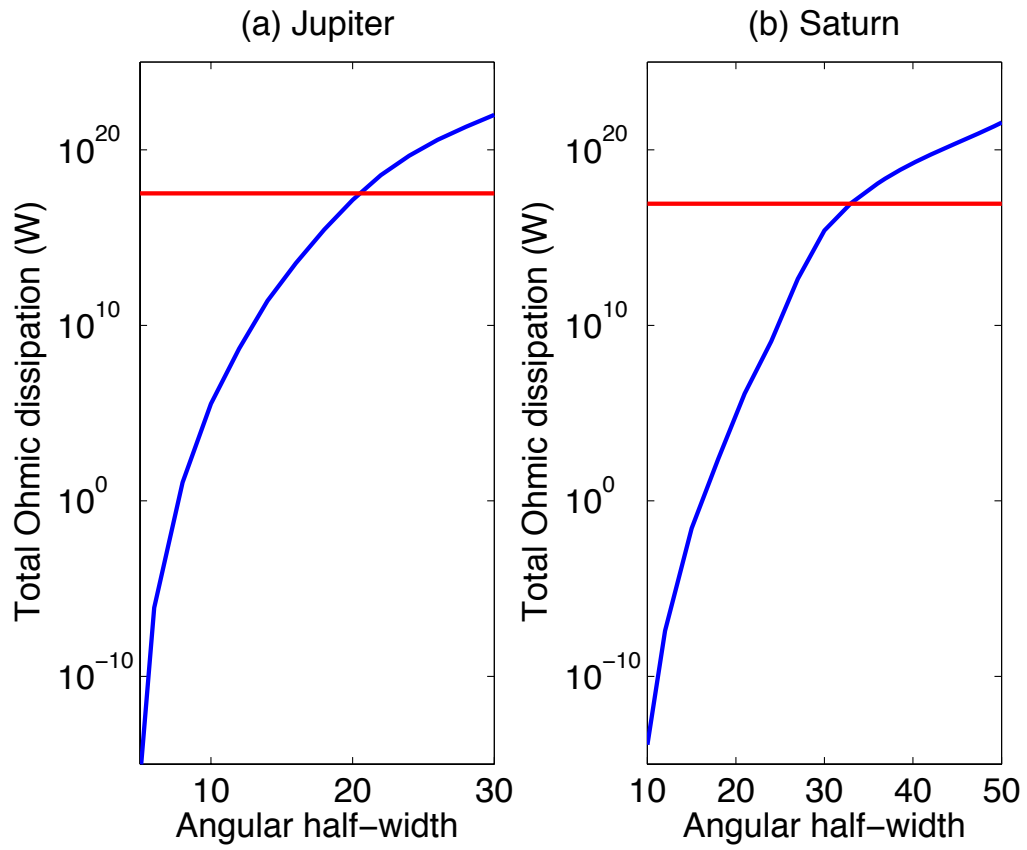
Figure 3.6 Total Ohmic dissipation rate verses jet half-width. The horizontal lines mark the planet's net luminosity.

3.6   Conclusion and discussion

The condition that the total Ohmic dissipation not exceed the planet's net luminosity sets a firm upper bound on the depth to which the zonal flows observed in the atmospheres of Jupiter and Saturn could penetrate. However, it is implausible that the flows extend to these depths because it seems impossible to break the Taylor-Proudman constraint in the convective envelope. Most likely the zonal flows are truncated in a stably stratified layer at shallow depth.

3.7   Appendix: choose the poloidal magnetic field models

External to the planet, the magnetic field may be expressed as the gradient of a scalar potential V ($\mathbf{B} = -\nabla V$) due to the absence of local current ($\nabla \times \mathbf{B} = 0$). The scalar potential V can be expanded in spherical harmonics:

$$V = a \sum_{n=1}^{\infty} \left[\left(\frac{r}{a}\right)^n Y_n^e + \left(\frac{a}{r}\right)^{n+1} Y_n^i \right], \tag{3.57}$$

where a is the equatorial radius of the planets. The first series in increasing power of r represents the contribution due to an external source and the second series in inverse power of r is the contribution due to the internal planetary field, with

$$Y_n^i = \sum_{m=0}^{n} \left(P_n^m \left(\cos(\theta)\right) \left[g_n^m \cos(m\phi) + h_n^m \sin(m\phi) \right] \right), \tag{3.58}$$

where $P_n^m \left(\cos(\theta)\right)$ are Schmidt quasi-normalized associated Legender functions of degree n and order m, and g_n^m, h_n^m are the internal Schmidt coefficients. Here we are only interested in the observed magnetic field produced by the internal magnetic field because the contribution to the field from the external current is negligible small inside the planet.

The magnetic fields of Jupiter and Saturn have been measured by various spacecrafts (Connerney, 1993). These observations are confined to low magnetic latitudes and large radial distance. The closest measurement for Jupiter's magnetic field reaches 1.6 R_J (by Pioneer 11), and is 1.3 R_S for Saturn (by Pioneer 11). Due to the low spatial resolution and poor spatial coverage of the measurements and the difficulties of separating the signals from the internal magnetic field and the external magnetic field, the standard approach is to limit the field model to the coefficients of low degree and order spherical harmonics only (up to $n = 3$). In this approach, the magnetic fields of the giant planets are dominated by a dipole field plus a small amount of non-dipole field that is approximated by quadrupole and octupole component field. This has two possible interpretations: either the higher harmonics are, in fact, small (the usual assumption) or the higher harmonics (including perhaps those beyond octupole) are not in fact small but tend to cancel each other in the (near closest approach) locations where the measurements are made. In the latter case, the downward continuation of the observed field models might be unreliable.

In general, the interaction of the toroidal zonal flow and the poloidal magnetic field will produce the toroidal magnetic field and poloidal electrical current. As we discussed in section (3.4), poloidal electrical current is mainly determined locally and dominated by the component along the θ direction: $(\mathbf{U}_T \times \mathbf{B}_P)_\theta = |\mathbf{U}_T|\,|\mathbf{B}_P \cdot \mathbf{e}_r|$ (see equation (3.19)), where $\mathbf{e}_r$ is the unit vector along the spherical radial direction.

Consider the following special field geometry: The large zonal flow is concentrated in the low latitude region and the magnetic field lines are gathered in the polar region like a sheaf of wheat. For this special field geometry, the spherical radial component of the poloidal field $(\mathbf{B}_P \cdot \mathbf{e}_r)$ is in fact near zero at the region with large zonal flow. The electrical current will be mainly determined by the global term, i.e., by the integration of $(\mathbf{U}_T \times \mathbf{B}_P)_r = |\mathbf{U}_T|\,|\mathbf{B}_P \cdot \mathbf{e}_\theta|$ from the radius r to the planetary surface (see equation (3.19)). Since this radius of the penetration of zonal flow is close to the surface, the magnitude of the electrical current will be about one order of magni-

tude smaller than that produced by a pure dipole field (with non-zero $\mathbf{B}_P \cdot \mathbf{e}_r$), and the Ohmic dissipation will be two orders of magnitude smaller. So, the interesting question is whether this special field geometry is consistent with the magnetic field measurements external to the planet. Before we address this question, it is worth noticing that it is necessary to have large electrical current along the azimuthal direction to confine the magnetic field lines in the polar region. Since the electrical conductivity of hydrogen decreases exponentially towards the surface from the metallic hydrogen region, the magnetic field lines might only be confined in the metallic hydrogen region (with high magnetic Reynolds number) and will spread out in the semi-conducting molecular region. From the order of magnitude analysis in section 3.3 and the detailed calculation in later section, we find that the magnetic Reynolds number is of order unity or less at the place where the total Ohmic dissipation is less than the planet net luminosity. So, it is possible that the magnetic field lines spread out already at that region.

In order to investigate whether this special field geometry is consistent with the observation, we calculate the radial component of the magnetic field along the trajectory of the spacecraft from the given low order spherical harmonics. We use O_6 model for Jupiter and Z_3 model for Saturn (Connerney, 1993). Since the difference between the observation and the low degree spherical harmonics model is within 200 nT (Connerney et al., 1982; Smith et al., 1976), it is reasonable to treat the modeled magnetic field as a representation of the observed field. Then we add in the constraints that the radial field in the low latitude region is near zero at some particular spherical radius inside the planet. Based on these constraints and the observation closest to the planet, we obtain the coefficients for higher order spherical harmonics and recalculate the magnetic field for other points along the spacecraft's trajectory.

For Jupiter, we obtain the trajectory of the Pioneer 11 spacecraft from the website of the NSSDC (National Space Science Data Center). Consider the axisymmetric field. We calculate the radial component of the magnetic field along the trajectory

of the spacecraft by combining the spherical harmonics of $n = 1$ and $n = 3$ from the O_6 model and treat the modeled field as observation. At the equator, the main contribution to the axisymmetric radial field comes from the axial quadrupole. However it is small. The dipole field becomes dominant even for quite small latitude (10 degrees or more). For greatly reducing the Ohmic dissipation, we would have to suppose that the octupole and higher odd harmonics cancel this dipole field (at least partially and for modest latitudes, e.g., 20 to 40 degrees). Therefore, here we look at the possibility of constructing an alternative model that involves quite large harmonics coefficients for $n = 1, 3, 5, 7$. For Jupiter, the closest approach of Pioneer 11 is at $(r, \theta) = (1.6R_J, 103.38°)$. We add in the constraints that the spherical radial field goes to near zero in the low latitude region ($\theta = 60° \sim 120°$) inside the planet $\sim 0.95R_J$. Combine this constraint and the modeled magnetic field at the closest approach. We can calculate g_3^0, g_5^0, and g_7^0 (assuming g_1^0 is well known). The coefficient for the spherical harmonics from model is $g_1^0 = 4.24$ and $g_3^0 = 0.07505$. The calculation with the added constraints gives $g_1^0 = 4.24$, $g_3^0 = -3.2717$, $g_5^0 = -6.5925$, $g_7^0 = -2.5627$. In the field model with added constraints, the coefficients for the higher order spherical harmonics are much larger than those in the O_6 model. Based on those coefficients for higher order spherical harmonics, we can recalculate the magnetic field along the trajectory of the spacecraft and compare it with O_6 model. Figure (3.7) shows the comparison of the magnetic fields. From this figure, we can see that the differences between two magnetic field models are large (up to 0.5 G ~ 50000 nT) at the place close to the planets. Since the r.m.s. for fitting the coefficients of the spherical harmonics model to the observation is generally less than 200 nT (Connerney, 1993; Smith et al., 1976), we claim that this special field geometry is not consistent with the observation.

For Saturn, we model the radial component of the magnetic field along the Voyager 2 trajectory (Connerney, 1993) by combining the spherical harmonics of $n = 1$ and $n = 3$ from Z_3 model and treating the modeled field as observation. For Saturn, the closest approach of Voyager 2 is at: $(r, \theta) = (2.7R_S, 75°)$. We then add in the constraints that the spherical radial field goes to near zero in the low latitude
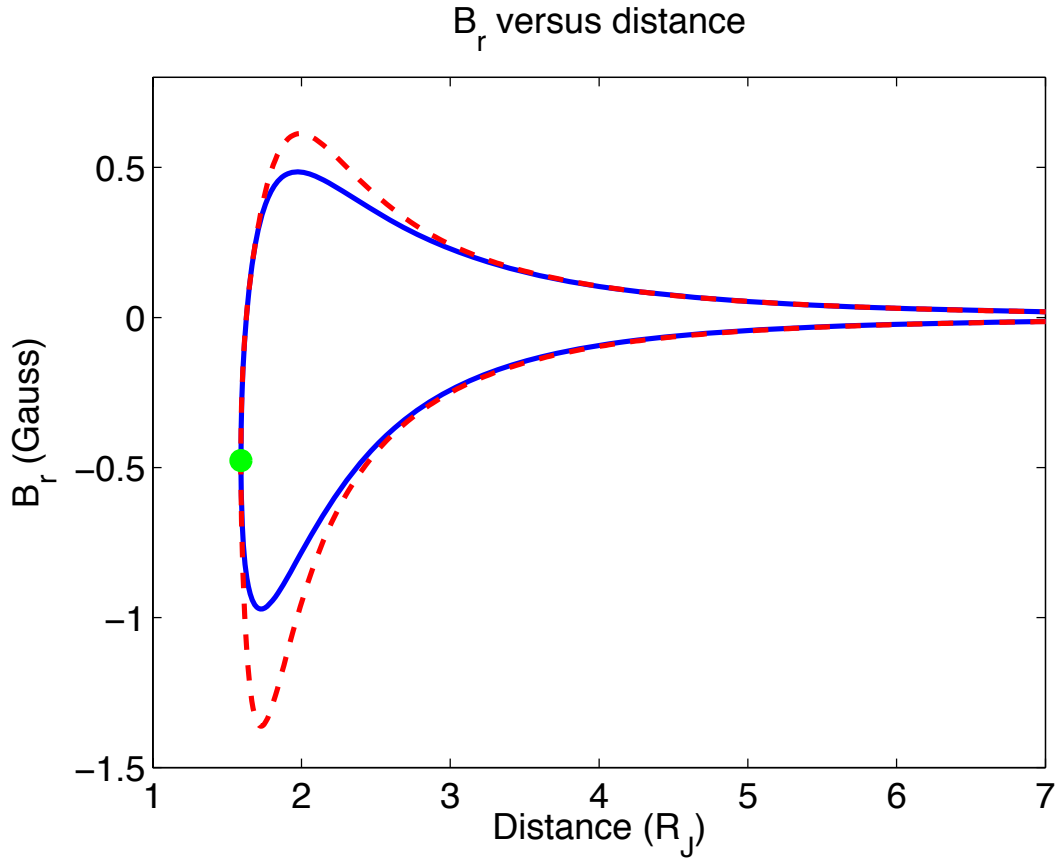
Figure 3.7 This figure shows the comparison of the magnetic fields: the radial component of the magnetic field versus the distance between the spacecraft and the planets. The solid line is the magnetic field obtained from O_6 model; the dash line is the calculated magnetic field with added constraints; and the dot indicates the closest approach of the spacecraft. From this figure, we can see that the differences between two magnetic field models are large (up to 0.5 G $\sim$ 50000 nT) close to the planets. Far away from the planets, the differences are small and cannot be detected.

region ($\theta = 60° \sim 120°$) inside the planet $\sim 0.87R_S$. Combine this constraint and the modeled magnetic field at the closest approach, we can calculate g_3^0, g_5^0, and g_7^0. From the Z_3 model, the coefficients for the spherical harmonics are $g_1^0 = 0.215353$ and $g_3^0 = 0.02743$. The calculation with the added constraints gives $g_1^0 = 0.215353$, $g_3^0 = 0.0131$, $g_5^0 = -0.0740$, $g_7^0 = -0.0280$. In the field model with added constraints, the coefficients for the higher order spherical harmonics are much larger than the Z_3 model. Based on those coefficients, we can recalculate the magnetic field for the second point $(r, \theta) = (3.0R_S, 62°)$ along the trajectory and compare it with the modeled magnetic field. For this point, the modeled magnetic field is 0.0106 G, and the calculated field based on the added constraint is 0.0108 G. So, the difference is about 20 nT, which is a little bit larger than the r.m.s of the least square fitting of the observed magnetic field (~ 3 nT) (Connerney et al., 1982). Because the small amplitude of Saturn's magnetic field, and the large radial distance of the observation, it is hard to tell whether the observed field is consistent with the special field geometry. In order to test this assumption, we need to have spacecraft measurements close to the planet and in the high latitude region.

Our conclusion is that non-dipole terms cannot enormously influence our calculation. This conclusion rests on two facts: first, the electrical conductivity is quite low and the magnetic Reynolds number is of order unity or less where the Ohmic dissipation becomes important (as explained in our order of magnitude analysis in section 3.3) thereby guaranteeing that magnetic fields generated in this region can not affect the field greatly. Second, the observed external fields are inconsistent with small radial field at the near-surface radius of relevance. Therefore, it is enough to use the downward continuation of the dipolar magnetic field.

Chapter 4   Ohmic dissipation constraint on the vertical flow structure for Uranus and Neptune

4.1   Introduction

For Uranus and Neptune, we assume the observed flow penetrating to the deep interior along the Taylor-Proudman cylinders and calculated the associated Ohmic dissipation. The differences from the calculations for Jupiter and Saturn lie in the following aspects: (1) The electrical conductivity distribution in the interior of Uranus and Neptune exhibits large uncertainties; therefore different conclusions can be drawn from the different conductivity profiles. (2) The magnetic fields observed on the surfaces of Uranus and Neptune contain significant amounts of the quadrupole component, thus it is necessary to conduct the calculation for the non-axisymmetric magnetic field, which is different from the axisymmetric calculation in the previous chapter. Based on those considerations, we estimate the amount of Ohmic dissipation produced by the penetrating zonal winds on Uranus and Neptune in this chapter.

The interior model for Uranus and Neptune estimated from mass, radius, rotational rate, and gravity field of the planets consists of three layers: the outer "gas" envelope which is mainly composed of hydrogen and helium; the intermediate "ice" layer made of a mixture of the molecules H_2O, CH_4, and NH_3; and a central rocky core with chondritic bulk proportions of iron, oxygen, magnesium, and silicon (Podolak et al., 1991; Hubbard et al., 1991, 1995). In chapter 2, the electrical conductivity profiles are calculated based on the interior model and the relationship between the conductivity and pressure for hydrogen and water ice (Nellis et al., 1996, 1999;

Mitchell and Nellis, 1982; Nellis et al., 1988). The electrical conductivity profile in the outer "gas" layer is largely determined by the mixing ratio of water ice.

In this Chapter, we find the maximum penetration depth of the zonal winds permitted by the Ohmic dissipation constraint is influenced by the water ice mixing ratio and is close to the transition radius from the outer "gas" envelope to the intermediate "ice" layer.

4.2   Order of magnitude analysis.

Similar with the previous section, we define three characteristic velocities: U, the magnitude of the observed zonal flow; $u_c = (F/\rho)^{1/3}$, a characteristic convective velocity based on the heat flux, F, and density, ρ; and $u_B = \left(B_p^2/\mu_0\rho\right)^{1/2}$, a characteristic Alfven velocity based on the magnitude of the observed poloidal magnetic field, B_p.

Consider a zonal flow of amplitude U that extends to a depth $d_* = R - r_*$ and weakens below. We assume that the magnetic Reynolds number is small at d_*. The magnitude of the electrical field associated with the penetrating zonal flow is $\sim UB_p$ and the resulting current density is $\sim \sigma UB_p$. The Ohmic dissipation per unit area produced by this current is $l\sigma U^2 B_p^2 \sim \left(\frac{Ul}{\lambda}\right) Uu_B^2\rho \sim R_m Uu_B^2\rho$, where l is the scale height of the magnetic diffusivity. We can then estimate the ratio (Γ) of Ohmic dissipation per unit area to the planetary heat flux at d_*:

$$\Gamma = \frac{R_m Uu_B^2\rho}{F} = R_m \left(\frac{U}{u_c}\right)\left(\frac{u_B}{u_c}\right)^2 = R_m \frac{UB_p^2}{\mu_0 F}. \tag{4.1}$$

Notice that this ratio is determined by the magnetic Reynolds number R_m and the observable quantities U, B, and F. Since the magnitude of the flow below the penetration depth is several orders of magnitude smaller than U and the magnetic diffusivity is an exponential function of radius, the majority of the total Ohmic dissipation is generated within the spherical shell with thickness l around the penetration depth.

Taking the surface integral of equation (4.1) over the spherical shell yields the ratio of total Ohmic dissipation to planetary net luminosity, which is the same as Γ. Since the total Ohmic dissipation cannot be larger than the planetary net luminosity, the flow cannot penetrate to the depth at which $\Gamma > 1$. At the place where $R_m \sim 1$, the ratio of Ohmic dissipation to heat flow simplifies to $\frac{UB_p^2}{\mu_0 F}$, which is independent of λ, l and ρ. Can the surface zonal flow penetrate to this depth? The answer is shown in figure (4.1). From Voyager IRIS data, the intrinsic flux of the giant planets has been estimated (Pearl and Conrath, 1991). For Jupiter, $F \sim 5.44$ W m^{-2}; for Saturn, $F \sim 2.01$ W m^{-2}; for Uranus, $F \sim 0.042$ W m^{-2}; for Neptune, $F \sim 0.43$ W m^{-2}. The case of Uranus is less clear. Its intrinsic heat flux F is significantly smaller than that of the other giant planets. Detailed modeling of its atmosphere, however, indicates that $F \geq 0.06$ W m^2 (Marley & McKay, 1999; Guillot, 2005). In this calculation, we use $F \sim 0.06$ W m^{-2} for Uranus.

From figure (4.1), we can see that for Jupiter, Saturn and Uranus, Γ is larger than unity. Therefore, the observed zonal flow cannot penetrate to the depth with $R_m \sim 1$. However, for Neptune, $\Gamma \sim 0.2$, the observed zonal flow on Neptune can penetrate to the depth with $R_m \sim 1$ but cannot penetrate to the depth with $R_m \sim 10$.

The magnetic Reynolds number at the level where the total Ohmic dissipation matches the planet's net luminosity is

$$R_m^* = \Gamma \frac{\mu_0 F}{UB_p^2} = \frac{\mu_0 F}{UB_p^2}. \tag{4.2}$$

For Uranus $R_m^* \sim 0.5$, for Neptune $R_m* \sim 8.5$. In steady state, the toroidal magnetic field produced by the interaction of the penetrating zonal flow and the poloidal magnetic field has magnitude: $B_T \sim B_p R_m^* \sim 0.1$ G for Uranus and $B_T \sim B_p R_m^* \sim 0.8$ G for Neptune.

Next we compare the Lorentz force produced by the magnetic field with the Cori-
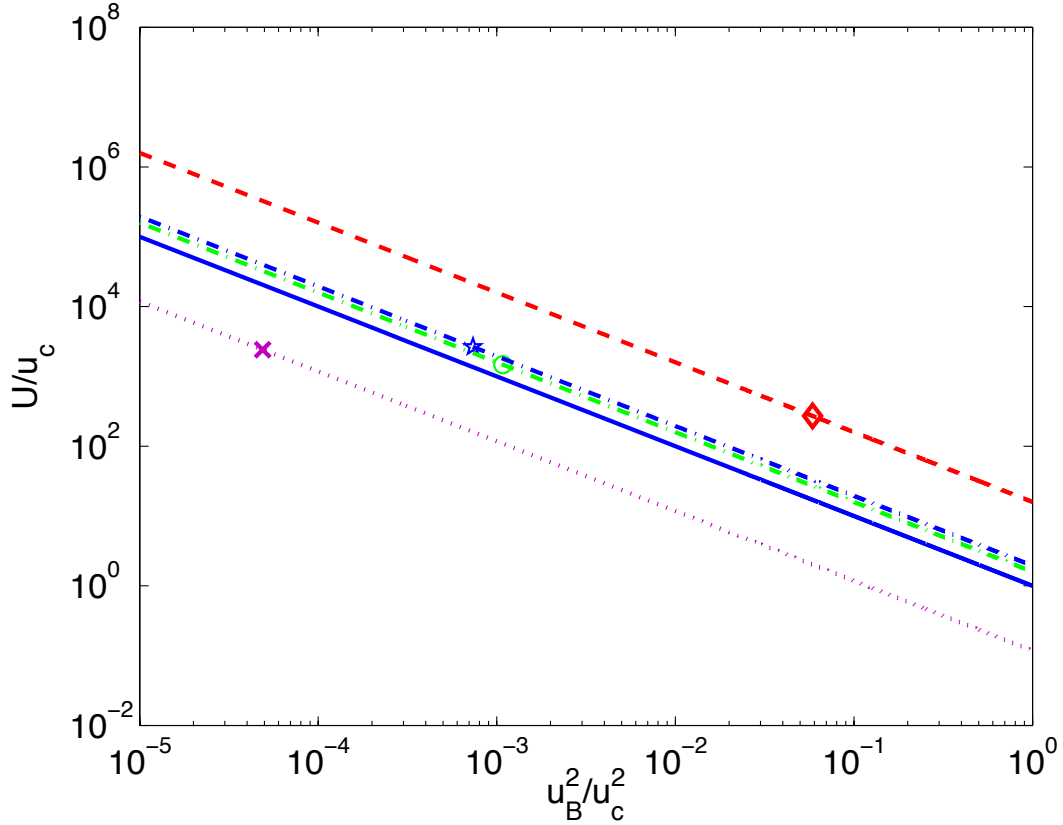
Figure 4.1 This figure plots $\left(\frac{U}{u_c}\right)$ versus $\left(\frac{u_B}{u_c}\right)^2$ for different values of Γ at the radius where $R_m = 1$. The solid line corresponds to $\Gamma = 1$. From top to bottom, the dash lines correspond to value of $\Gamma \approx 20$, $\Gamma \approx 2$, $\Gamma \approx 2.3$ and $\Gamma \approx 0.2$ appropriate to Jupiter, Saturn, Uranus and Neptune, respectively. The diamond, star, circle and cross correspond to values of U and u_B normalized by $u_c = \left(\frac{F}{\rho}\right)^{\frac{1}{3}}$ where ρ is evaluated at the layer where $R_m = 1$. For Uranus, $U \sim 200$ m s^{-1}, $F \sim 0.06$ W m^{-2} and $B_p \sim 0.2$ G, so $\Gamma \sim 2.3$. For Neptune, $U \sim 400$ m s^{-1}, $F \sim 0.45$ W m^{-2} and $B_p \sim 0.1$ G, so $\Gamma \sim 0.2$.

olis force. The Lorentz force is

$$\mathbf{F}_{Lorentz} = \frac{(\nabla \times \mathbf{B}) \times \mathbf{B}}{\mu_0 \rho} \sim \frac{B_T B_p}{l \mu_0 \rho} \sim \frac{R_m^* B_p^2}{l \mu_0 \rho}, \tag{4.3}$$

whereas the Coriolis force is

$$\mathbf{F}_{Coriolis} = 2\Omega \mathbf{e}_z \times \mathbf{U} \sim 2\Omega U. \tag{4.4}$$

Here $\mathbf{e}_z$ is the unit vector along the rotation axis and Ω is the rotation frequency of planet. Their ratio is

$$\Lambda = \frac{|\mathbf{F}_{Lorentz}|}{|\mathbf{F}_{Coriolis}|}. \tag{4.5}$$

For values similar to those where $\Gamma \sim 1$: $\rho \sim 0.01$ g cm^{-3}, $\Omega \sim 2 \times 10^{-4} s^{-1}$ and $l \sim 1000$ km, Λ is about 10^{-7} for both Uranus and Neptune. Therefore, the Lorentz force cannot cause the flow to depart from the cylindrical Taylor-Proudman state.

4.3 Detailed formulation

The electric current density $\mathbf{J}$ can be expressed as

$$\mathbf{J} = \sigma \left(\mathbf{E} + \mathbf{U} \times \mathbf{B} \right) \tag{4.6}$$

where σ is the electrical conductivity; $\mathbf{U}$ is the velocity of the flow; $\mathbf{B}$ is the magnetic field; and $\mathbf{E}$ is the electrical field, which is defined by the force on a charge at rest in the reference frame. For Uranus and Neptune, the reference frame is the deep-seated magnetic field generated by the planetary dynamo.

Both the flow velocity $\mathbf{U}$ and the magnetic field can be decomposed into the sum of poloidal and toroidal components: $\mathbf{U} = \mathbf{U}_P + \mathbf{U}_T$, $\mathbf{B} = \mathbf{B}_P + \mathbf{B}_T$. For the velocity field $\mathbf{U}$, its poloidal component $\mathbf{U}_P$ is in the radial and latitudinal direction: $\mathbf{U}_P = (U_r, U_\theta, 0)$; and its toroidal component $\mathbf{U}_T$ is in the azimuthal direction: $\mathbf{U}_T =$

$(0, 0, U_\phi)$. For the magnetic field $\mathbf{B}$, its poloidal component $\mathbf{B}_P$ is in the radial and latitudinal direction: $\mathbf{B}_P = (B_r, B_\theta, B_\phi)$; and its toroidal component $\mathbf{B}_T$ is in latitudinal and azimuthal direction: $\mathbf{B}_T = (0, B_\theta, B_\phi)$. Based on this decomposition, the density of the electrical current $\mathbf{J}$ can be rewritten as

$$\mathbf{J} = \sigma \left(\mathbf{E} + \mathbf{U}_T \times \mathbf{B}_P + \mathbf{U}_P \times \mathbf{B}_T + \mathbf{U}_P \times \mathbf{B}_P + (\mathbf{U}_T \times \mathbf{B}_T)_r \right), \qquad (4.7)$$

where $(\mathbf{U}_T \times \mathbf{B}_T)$ has only the component along the r direction. Both Uranus and Neptune are fast-rotating planets. The large Coriolis force acting on the fluid particle inhibits the motion along the radial and latitudinal direction. Based on the mixing length estimation, the magnitude of the poloidal velocity field is about 1 cm s^{-1} (Guillot et al., 2004), which is four orders of magnitude less than the observed zonal flow ~ 100 m s^{-1} on the surfaces of planets. It implies $|\mathbf{U}_P \times \mathbf{B}_P| \ll |\mathbf{U}_T \times \mathbf{B}_P|$.

Since the toroidal component of the magnetic field is confined in the region of finite electric current, only the poloidal component of the magnetic field can be observed external to the planets. For the observed magnetic field of Uranus and Neptune, the quadrupole component is as strong as the dipole component (~ 0.2 G). Inside the planet, the poloidal magnetic field interacts with the toroidal components of the flow and produces a toroidal magnetic field with the magnitude $|\mathbf{B}_T| \sim R_m |\mathbf{B}_P|$. From later calculations, we will find that the magnetic Reynolds number is small ($R_m \ll 1$) in the region of relevance to our calculation. So, it is reasonable to assume $|\mathbf{U}_P \times \mathbf{B}_T| \ll |\mathbf{U}_T \times \mathbf{B}_P|$. The current density can be rewritten as

$$\mathbf{J} = \sigma \left(\mathbf{E} + \mathbf{U}_T \times \mathbf{B}_P + (\mathbf{U}_T \times \mathbf{B}_T)_r \right). \qquad (4.8)$$

In the steady state, the electrical field can be written as the gradient of the electrical potential: $\mathbf{E} = -\nabla \varphi$. Substituting this equation and the definition of

magnetic diffusivity into equation (4.8), we arrive at

$$\mathbf{J} = \frac{1}{\mu_0 \lambda} \left(-\nabla\varphi + \mathbf{U}_T \times \mathbf{B}_P + (\mathbf{U}_T \times \mathbf{B}_T)_r \right). \tag{4.9}$$

The current density $\mathbf{J}$ is divergence free,

$$\nabla \cdot \mathbf{J} = 0. \tag{4.10}$$

Putting the expression of the current density (equation (4.9)) into equation (4.10), and conducting expansion in spherical coordinates (r, θ, ϕ), we then have

$$\frac{1}{r} \frac{\partial}{\partial r} \left(\frac{r^2}{\mu_0 \lambda} \left(-\frac{\partial\varphi}{\partial r} + (\mathbf{U}_T \times \mathbf{B}_P + \mathbf{U}_T \times \mathbf{B}_T)_r \right) \right)$$
$$+ \frac{1}{r \sin(\theta)} \frac{\partial}{\partial \theta} \left(\frac{\sin(\theta)}{\mu_0 \lambda} \left(-\frac{\partial\varphi}{\partial \theta} + (\mathbf{U}_T \times \mathbf{B}_P)_\theta \right) \right)$$
$$+ \frac{1}{r \sin(\theta)} \frac{\partial}{\partial \phi} \left(\frac{1}{\mu_0 \lambda} \left(-\frac{\partial\varphi}{\partial \phi} \right) \right) = 0. \tag{4.11}$$

The magnetic diffusivity increases very rapidly outward from the metallic region to the semi-conducting region. From chapter 2, we know that the scale height for the magnetic diffusivity is about several hundred kilometers in the outer region of the planets, which is much smaller than the typical length scale of the variation of the zonal flow in the meridional direction ($L \sim 10000$ km). Therefore, the dominant term in equation (4.11) is the one involving the derivative of the magnetic diffusivity respect to the radius: $\frac{\partial\lambda(r)}{\partial r}$. There are no other terms in equation (4.11) that can balance the magnitude of this term. Therefore, the divergence-free current density requires that the term involving the derivative of the magnetic diffusivity respect to the radius to be approximately zero:

$$\frac{1}{\mu_0 \lambda^2} \frac{d\lambda}{dr} \left(-\frac{\partial\varphi}{\partial r} + (\mathbf{U}_T \times \mathbf{B}_P + \mathbf{U}_T \times \mathbf{B}_T)_r \right) \approx 0. \tag{4.12}$$

The current density $\mathbf{J}$ along the radial direction can be written as

$$\mathbf{J}_r = \frac{1}{\mu_0 \lambda} \left(-\frac{\partial \varphi}{\partial r} + (\mathbf{U}_T \times \mathbf{B}_P + \mathbf{U}_T \times \mathbf{B}_T)_r \right). \tag{4.13}$$

Comparing equation (4.12) with equation (4.13), we find that the rapid variation of the magnetic diffusivity along the radial direction and the divergence free current density demand that the current along the radial direction to be almost zero and much less than the current along the meridional direction and azimuthal direction. Physically, this makes sense: The current that flows radially from deep regions is forced to flow meridionally and azimuthally in a thin layer, thereby having large amplitude. This is exactly analogous to the standard meteorological scaling that allows one to ignore vertical motions relative to horizontal motions in a thin atmosphere. In other words, the rapid variation of the magnetic diffusivity along the radial direction causes the current density along the r direction to be much smaller than that along the θ and ϕ direction.

We can also obtain an expression for the electrical potential φ from equation (4.12):

$$\frac{\partial \varphi}{\partial r} = (\mathbf{U}_T \times \mathbf{B}_P + \mathbf{U}_T \times \mathbf{B}_T)_r. \tag{4.14}$$

Integrating along the r-direction, we obtain

$$\varphi = -\int_r^R (\mathbf{U}_T \times \mathbf{B}_P + \mathbf{U}_T \times \mathbf{B}_P)_r \, dr' + Q(\theta, \phi), \tag{4.15}$$

where R is the planetary radius and $Q(\theta, \phi)$ is an arbitrary function of θ and ϕ. The electrical field in the θ direction can be written as

$$\mathbf{E}_\theta = -\frac{\partial \varphi}{\partial \theta} = \frac{1}{r} \left[\frac{\partial}{\partial \theta} \int_r^R (\mathbf{U}_T \times \mathbf{B}_P + \mathbf{U}_T \times \mathbf{B}_T)_r \, dr' - \frac{\partial Q(\theta)}{\partial \theta} \right]. \tag{4.16}$$

In the above equation (4.16), the first term in the parentheses is a function of both r, θ and ϕ. However, the second term in the parentheses $\frac{\partial Q(\theta, \phi)}{\partial \theta}$ is only a function of

θ and ϕ. These two terms cannot cancel each other at all radii.

From equation (4.9), we acquire the current density along the θ direction as

$$\mathbf{J}_\theta = \frac{1}{\mu_0 \lambda} = \left(-\frac{\partial \varphi}{\partial \theta} + (\mathbf{U}_T \times \mathbf{B}_P)_\theta \right). \qquad (4.17)$$

Substituting the expression for the electrical potential into this equation, we obtain

$$\mathbf{J}_\theta = \frac{1}{\mu_0 \lambda r} \left[\frac{\partial}{\partial \theta} \int_r^R (\mathbf{U}_T \times \mathbf{B}_P + \mathbf{U}_T \times \mathbf{B}_T)_r \, dr' + r \, (\mathbf{U}_T \times \mathbf{B}_P)_\theta - \frac{\partial Q}{\partial \theta} \right]. \qquad (4.18)$$

Similarly, the electric current density along the ϕ direction can be written as

$$\mathbf{J}_\phi = \frac{1}{\mu_0 \lambda r} \left[\frac{\partial}{\partial \phi} \int_r^R (\mathbf{U}_T \times \mathbf{B}_P + \mathbf{U}_T \times \mathbf{B}_T)_r \, dr' - \frac{\partial Q}{\partial \phi} \right]. \qquad (4.19)$$

The Ohmic dissipation per unit volume is equal to the square of the current density divided by the electric conductivity. Since the current along θ direction and ϕ direction is dominant, the Ohmic dissipation per unit volume is

$$
\begin{aligned}
P &= \frac{J^2}{\sigma} \\
&\approx \frac{1}{\mu_0 \lambda r} \left[\frac{\partial}{\partial \theta} \int_r^R (\mathbf{U}_T \times \mathbf{B}_P + \mathbf{U}_T \times \mathbf{B}_T)_r \, dr' + r \, (\mathbf{U}_T \times \mathbf{B}_P)_\theta - \frac{\partial Q}{\partial \theta} \right]^2 \\
&+ \frac{1}{\mu_0 \lambda r} \left[\frac{\partial}{\partial \phi} \int_r^R (\mathbf{U}_T \times \mathbf{B}_P + \mathbf{U}_T \times \mathbf{B}_T)_r \, dr' - \frac{\partial Q}{\partial \phi} \right]^2. \qquad (4.20)
\end{aligned}
$$

The magnitude of $\left| \frac{\partial}{\partial \theta} \int_r^R (\mathbf{U}_T \times \mathbf{B}_P + \mathbf{U}_T \times \mathbf{B}_T)_r \, dr' + r \, (\mathbf{U}_T \times \mathbf{B}_P)_\theta - \frac{\partial Q}{\partial \theta} \right|$ and $\left| \frac{\partial}{\partial \phi} \int_r^R (\mathbf{U}_T \times \mathbf{B}_P + \mathbf{U}_T \times \mathbf{B}_T)_r \, dr' - \frac{\partial Q}{\partial \phi} \right|$ can be bound in the following way: From equation (4.20), we can see that the Ohmic dissipation per unit volume is inversely proportional to the magnetic diffusivity. In the interior of the giant planet, the magnetic diffusivity of the material increases exponentially outward from the metallic conducting region with the scale height $H_\lambda(r)$. The Ohmic dissipation in the spherical

shell around r with thickness $H_\lambda(r)$ is approximately

$$
\begin{aligned}
P_{shell} \quad \sim \quad & \frac{4\pi r^2 H_\lambda J^2}{\sigma} \\
\sim \quad & \frac{4\pi r^2 H_\lambda}{\sigma} \left(\frac{\partial}{\partial \theta} \int_r^R (\mathbf{U}_T \times \mathbf{B}_P + \mathbf{U}_T \times \mathbf{B}_T)_r \, dr' + r \left(\mathbf{U}_T \times \mathbf{B}_P \right)_\theta - \frac{\partial Q}{\partial \theta} \right)^2 \\
+ \quad & \frac{4\pi r^2 H_\lambda}{\sigma} \left(\frac{\partial}{\partial \phi} \int_r^R (\mathbf{U}_T \times \mathbf{B}_P + \mathbf{U}_T \times \mathbf{B}_T)_r \, dr' - \frac{\partial Q}{\partial \phi} \right)^2 . \quad\quad (4.21)
\end{aligned}
$$

Since the total Ohmic dissipation cannot be larger than the planetary net luminosity L_{net}, we have

$$
\begin{aligned}
P_{shell} \quad \sim \quad & \frac{4\pi H_\lambda}{\mu_0 \lambda} \left(\frac{\partial}{\partial \theta} \int_r^R (\mathbf{U}_T \times \mathbf{B}_P + \mathbf{U}_T \times \mathbf{B}_T)_r \, dr' + r \left(\mathbf{U}_T \times \mathbf{B}_P \right)_\theta - \frac{\partial Q}{\partial \theta} \right)^2 \\
+ \quad & \frac{4\pi H_\lambda}{\mu_0 \lambda} \left(\frac{\partial}{\partial \phi} \int_r^R (\mathbf{U}_T \times \mathbf{B}_P + \mathbf{U}_T \times \mathbf{B}_T)_r \, dr' - \frac{\partial Q}{\partial \phi} \right)^2 \leq L_{net}. \quad\quad (4.22)
\end{aligned}
$$

Then we acquire the following upper bound:

$$
\frac{4\pi H_\lambda}{\mu_0 \lambda} \left(\frac{\partial}{\partial \theta} \int_r^R (\mathbf{U}_T \times \mathbf{B}_P + \mathbf{U}_T \times \mathbf{B}_T)_r \, dr' + r \left(\mathbf{U}_T \times \mathbf{B}_P \right)_\theta - \frac{\partial Q}{\partial \theta} \right)^2 \leq L_{net}, \quad (4.23)
$$

and

$$
\frac{4\pi H_\lambda}{\mu_0 \lambda} \left(\frac{\partial}{\partial \phi} \int_r^R (\mathbf{U}_T \times \mathbf{B}_P + \mathbf{U}_T \times \mathbf{B}_T)_r \, dr' - \frac{\partial Q}{\partial \phi} \right)^2 \leq L_{net}. \quad\quad (4.24)
$$

We consider the equation (4.23) first. It can be rewritten as

$$
\left| \frac{\partial}{\partial \theta} \int_r^R (\mathbf{U}_T \times \mathbf{B}_P + \mathbf{U}_T \times \mathbf{B}_T)_r \, dr' + r \left(\mathbf{U}_T \times \mathbf{B}_P \right)_\theta - \frac{\partial Q}{\partial \theta} \right| \leq \left(\frac{L_{net} \mu_0 \lambda}{4\pi H_\lambda} \right)^{\frac{1}{2}}. \quad (4.25)
$$

Define $\left| \frac{\partial}{\partial \theta} \int_r^R (\mathbf{U}_T \times \mathbf{B}_P + \mathbf{U}_T \times \mathbf{B}_T)_r \, dr' + r \left(\mathbf{U}_T \times \mathbf{B}_P \right)_\theta \right|$ as term 1, $\left| \frac{\partial Q(\theta, \phi)}{\partial \theta} \right|$ as term 2 and $\left| \frac{\partial}{\partial \theta} \int_r^R (\mathbf{U}_T \times \mathbf{B}_P + \mathbf{U}_T \times \mathbf{B}_T)_r \, dr' + r \left(\mathbf{U}_T \times \mathbf{B}_P \right)_\theta - \frac{\partial Q(\theta, \phi)}{\partial \theta} \right|$ as term 3. Both term 1 and term 2 can also be bound individually. Suppose term 1 and term 2 completely cancel each other at the radius r_*. They will not cancel each other at the nearby radius $r = r_* + H_\lambda(r_*)$. Across this layer with thickness $H_\lambda(r_*)$, term 2

doesn't change whereas the variation of term 1 is of order

$$\Delta \left| \frac{\partial}{\partial \theta} \int_r^R \left(\mathbf{U}_T \times \mathbf{B}_P + \mathbf{U}_T \times \mathbf{B}_T \right)_r dr' + r \left(\mathbf{U}_T \times \mathbf{B}_P \right)_\theta \right|$$

$$\sim \left| \frac{\partial}{\partial \theta} \int_{r_*}^R \left(\mathbf{U}_T \times \mathbf{B}_P + \mathbf{U}_T \times \mathbf{B}_T \right)_r dr' + r_* \left(\mathbf{U}_T \times \mathbf{B}_P \right)_\theta \right| \frac{H_\lambda(r_*)}{r_*}. \qquad (4.26)$$

Therefore, we have

$$\left| \frac{\partial}{\partial \theta} \int_{r_*}^R \left(\mathbf{U}_T \times \mathbf{B}_P + \mathbf{U}_T \times \mathbf{B}_T \right)_r dr' + r_* \left(\mathbf{U}_T \times \mathbf{B}_P \right)_\theta \right| \leq \frac{r_*}{H_\lambda(r_*)} \left(\frac{L_{net} \mu_0 \lambda(r_*))}{4\pi H_\lambda(r_*)} \right)^{1/2}. \qquad (4.27)$$

Since term 1 and term 2 completely cancel each other at r_*, we have

$$\left| \frac{\partial Q}{\partial \theta} \right| \leq \frac{r_*}{H_\lambda(r_*)} \left(\frac{L_{net} \mu_0 \lambda(r_*))}{4\pi H_\lambda(r_*)} \right)^{1/2}. \qquad (4.28)$$

Combining equations (4.27), (4.28) and (4.25), we find that the bound for term 1 and term 2 is of order $\frac{r}{H_\lambda(r)}$ larger than the bound for term 3.

Similarly, for equation (4.24), we have

$$\left| \frac{\partial}{\partial \phi} \int_{r_*}^R \left(\mathbf{U}_T \times \mathbf{B}_P + \mathbf{U}_T \times \mathbf{B}_T \right)_r dr' \right| \leq \frac{r_*}{H_\lambda(r_*)} \left(\frac{L_{net} \mu_0 \lambda(r_*))}{4\pi H_\lambda(r_*)} \right)^{1/2} \qquad (4.29)$$

and

$$\left| \frac{\partial Q}{\partial \phi} \right| \leq \frac{r_*}{H_\lambda(r_*)} \left(\frac{L_{net} \mu_0 \lambda(r_*))}{4\pi H_\lambda(r_*)} \right)^{1/2}. \qquad (4.30)$$

In Uranus and Neptune, a tight bound for $\left| \frac{\partial Q}{\partial \theta} \right|$ and $\left| \frac{\partial Q}{\partial \phi} \right|$ can be acquired at the layer near the top of the metallic water ice region, where: $\sigma \sim 2 \times 10^3$ S m^{-1}, $\lambda \sim 400$ m^2 s^{-1} and $H_\lambda \sim 1000$ km. For Uranus, we have

$$\left| \frac{\partial Q}{\partial \theta} \right| \leq \left(\frac{(0.6 \times 2.6 \times 10^7)^2 \times 4\pi \times 10^{-7} \times 0.034 \times 10^{16} \times 400}{4\pi \times (10^6)^3} \right)^{1/2} \sim 10^3 \text{ Tesla m}^2 \text{ s}^{-1}, \qquad (4.31)$$

and

$$\left| \frac{\partial Q}{\partial \phi} \right| \leq 10^3 \text{ Tesla m}^2 \text{ s}^{-1}. \tag{4.32}$$

For Neptune, we have $\left| \frac{\partial Q}{\partial \theta} \right| \leq 5 \times 10^3$ Tesla m s^{-1} and $\left| \frac{\partial Q}{\partial \phi} \right| \leq 5 \times 10^3$ Tesla m s^{-1}. From equation (4.23), we can also estimate the upper bound for the zonal velocity near the top of the metallic water ice region. If we assume the magnitude of the poloidal magnetic field $\mathbf{B}_P$ is in the same order as the toroidal magnetic field $\mathbf{B}_T$, the magnitude of $\left| \frac{\partial}{\partial \theta} \int_r^R (\mathbf{U}_T \times \mathbf{B}_P + \mathbf{U}_T \times \mathbf{B}_T)_r \, dr' + r (\mathbf{U}_T \times \mathbf{B}_P)_\theta \right|$ is approximately $|r\mathbf{U}_T\mathbf{B}_P|$. Therefore, we have

$$|\mathbf{U}_T| \leq \frac{1}{|\mathbf{B}_P|H_\lambda} \left(\frac{L_{net}\mu_0\lambda}{4\pi H_\lambda} \right)^{1/2}. \tag{4.33}$$

If we assume that the magnitude of the poloidal magnetic field is in the same order as the downward continuation of the observed dipole field, we obtain $|\mathbf{U}_T| \leq 5$ m s^{-1} for Uranus and $|\mathbf{U}_T| \leq 20$ m s^{-1} for Neptune. If the magnitude of the zonal flow velocity is larger than the upper bound, excessive Ohmic dissipation will be produced.

At the outer region of the giant planets, the magnitude of the velocity is about 200 m s^{-1}. The magnitude of $\left| \frac{\partial}{\partial \theta} \int_r^R (\mathbf{U}_T \times \mathbf{B}_P + \mathbf{U}_T \times \mathbf{B}_T)_r \, dr' + r (\mathbf{U}_T \times \mathbf{B}_P)_\theta \right|$ is approximately $|r\mathbf{U}_T\mathbf{B}_P| \sim 10^5$ Tesla m^2 s^{-1}, which is much larger than the upper bound for $\left| \frac{\partial Q}{\partial \theta} \right|$ and $\left| \frac{\partial Q}{\partial \phi} \right|$. Thus, for calculating the Ohmic dissipation produced by the deep-seated large cylindrical zonal winds (~ 200 m s^{-1}), we can ignore the term related with $\frac{\partial Q}{\partial \theta}$ and $\frac{\partial Q}{\partial \phi}$ in equation (4.18), (4.19) and (4.20).

Therefore, the current density along the θ direction can be rewritten as

$$\mathbf{J}_\theta(r, \theta, \phi) = \frac{1}{\mu_0\lambda} \left[\frac{1}{r} \frac{\partial}{\partial \theta} \int_r^R (\mathbf{U}_T \times \mathbf{B}_P + \mathbf{U}_T \times \mathbf{B}_T)_r \, dr' + (\mathbf{U}_T \times \mathbf{B}_P)_\theta \right], \tag{4.34}$$

and the current density along the ϕ direction can be rewritten as

$$\mathbf{J}_\phi(r, \theta, \phi) = \frac{1}{\mu_0\lambda} \left[\frac{1}{r} \frac{\partial}{\partial \phi} \int_r^R (\mathbf{U}_T \times \mathbf{B}_P + \mathbf{U}_T \times \mathbf{B}_T)_r \, dr' \right], \tag{4.35}$$

In the equation (4.34), the first term comes from the electrical field $\mathbf{E}$. It is a global term since it depends on the integration of the radial component of $\mathbf{U}_T \times \mathbf{B}_P$ from r to R. The second term is a local term, since it is determined by the local value of the meridional component of $\mathbf{U}_T \times \mathbf{B}_P$. If we assume that the poloidal magnetic field is in the same order as the poloidal magnetic field, the global term can be estimated as

$$\frac{1}{\mu_0 \lambda} \left[\frac{1}{r} \frac{\partial}{\partial \theta} \int_r^R (\mathbf{U}_T \times \mathbf{B}_P + \mathbf{U}_T \times \mathbf{B}_T)_r \, dr' \right] \sim \frac{1}{\mu_0 \lambda} \frac{R-r}{r} |(\mathbf{U}_T \times \mathbf{B}_P)_r| . \qquad (4.36)$$

The local term can be expressed approximately:

$$\frac{1}{\mu_0 \lambda} (\mathbf{U}_T \times \mathbf{B}_P)_\theta \sim \frac{1}{\mu_0 \lambda} |(\mathbf{U}_T \times \mathbf{B}_P)_\theta| . \qquad (4.37)$$

For the spherical shell close to the surface, we have: $R - r \ll r$. Thus, the local term is much larger than the global term and the current density along the θ direction is dominated by the local values of $(\mathbf{U}_T \times \mathbf{B}_P)_\theta$.

Based on the expression for the current density (equation (4.34)), we can calculate the Ohmic dissipation per unit volume produced by the current:

$$\begin{aligned} P = \frac{J^2}{\sigma} &= \frac{1}{\mu_0 \lambda} \left[\frac{1}{r} \frac{\partial}{\partial \theta} \int_r^R (\mathbf{U}_T \times \mathbf{B}_P + \mathbf{U}_T \times \mathbf{B}_T)_r \, dr' + (\mathbf{U}_T \times \mathbf{B}_P)_\theta \right]^2 \\ &+ \frac{1}{\mu_0 \lambda} \left[\frac{1}{r} \frac{\partial}{\partial \phi} \int_r^R (\mathbf{U}_T \times \mathbf{B}_P)_r \, dr' \right]^2 . \end{aligned} \qquad (4.38)$$

Taking the volume integral of equation (4.38) in the whole sphere, we obtain the total Ohmic dissipation produced by the deep-seated zonal flow:

$$\begin{aligned} P_{total} &= \frac{2\pi}{\mu_0} \int_0^R \frac{dr'}{\lambda(r')} \int_0^{2\pi} d\phi \int_0^\pi d\theta \sin(\theta) \left[\frac{\partial}{\partial \theta} \int_{r'}^R (\mathbf{U}_T \times \mathbf{B}_P + \mathbf{U}_T \times \mathbf{B}_T)_r \, dr'' + r (\mathbf{U}_T \times \mathbf{B}_P)_\theta \right]^2 \\ &+ \frac{2\pi}{\mu_0} \int_0^R \frac{dr'}{\lambda(r')} \int_0^{2\pi} d\phi \int_0^\pi d\theta \sin(\theta) \left[\frac{\partial}{\partial \theta} \int_{r'}^R (\mathbf{U}_T \times \mathbf{B}_P + \mathbf{U}_T \times \mathbf{B}_T)_r \, dr'' \right]^2 . \end{aligned} \qquad (4.39)$$

The total Ohmic dissipation cannot be larger than the intrinsic energy radiated per second by the planet, which will give us an upper bound for the penetration depth of

the observed zonal flow.

4.4   Ohmic dissipation calculation

On Uranus and Neptune, the deep penetrating zonal flow interacts with the pre-existing poloidal magnetic field, produces toroidal magnetic field and modifies the pre-existing poloidal magnetic field. The dimensionless number characterizing the interaction is the magnetic Reynolds number: $R_m = \frac{Ul}{\lambda}$, where U is the characteristic velocity; l is the length scale and can be taken as the scale height of the magnetic diffusivity; and λ is the magnetic diffusivity. If the magnetic Reynolds number is small, $R_m << 1$, the induced toroidal magnetic field and the modification for the pre-existing poloidal magnetic field would be much smaller than the pre-existing poloidal field. In this section, we first assume that the magnetic Reynolds number is small. Then $|\mathbf{U}_T| \ll |\mathbf{U}_P|$ and we can use downward continuation of the observed magnetic field as the poloidal field. Under this assumption, the current density along the θ and ϕ directions can be written as

$$\mathbf{J}_\theta(r, \theta, \phi) = \frac{1}{\mu_0 \lambda} \left[\frac{1}{r} \frac{\partial}{\partial \theta} \int_r^R (\mathbf{U}_T \times \mathbf{B}_P)_r \, dr' + (\mathbf{U}_T \times \mathbf{B}_P)_\theta \right], \qquad (4.40)$$

and

$$\mathbf{J}_\phi(r, \theta, \phi) = \frac{1}{\mu_0 \lambda} \left[\frac{1}{r} \frac{\partial}{\partial \phi} \int_r^R (\mathbf{U}_T \times \mathbf{B}_P)_r \, dr' \right]. \qquad (4.41)$$

And the total Ohmic dissipation can be rewritten as

$$
\begin{aligned}
P_{total} &= \frac{2\pi}{\mu_0} \int_0^R \frac{dr'}{\lambda(r')} \int_0^{2\pi} d\phi \int_0^\pi d\theta \sin(\theta) \left[\frac{\partial}{\partial \theta} \int_{r'}^R (\mathbf{U}_T \times \mathbf{B}_P)_r \, dr'' + r \, (\mathbf{U}_T \times \mathbf{B}_P)_\theta \right]^2 \\
&+ \frac{2\pi}{\mu_0} \int_0^R \frac{dr'}{\lambda(r')} \int_0^{2\pi} d\phi \int_0^\pi d\theta \sin(\theta) \left[\frac{\partial}{\partial \theta} \int_{r'}^R (\mathbf{U}_T \times \mathbf{B}_P)_r \, dr'' \right]^2 . \qquad (4.42)
\end{aligned}
$$

We assume that the observed zonal flows on the surface of the giant planets pen-

etrating to the deep interior along cylinders and vanishes below the hypothesized spherical cut-off radius. Figure (4.2) shows the relation between the total Ohmic dissipation and the hypothesized spherical cut-off radius for Uranus and Neptune based on different water-ice mixing ratio in the gas envelope. The planetary net luminosity is 0.034×10^{17} W for Uranus and 0.33×10^{17} W for Neptune (Guillot, 2005). For total Ohmic dissipation being less than the planetary net luminosity, the maximum penetration depth for Uranus surface wind is about $0.8R_U$ if the water ice is confined in the intermediate ice layer, and it shifts outwards as the mixing ratio of water ice in the gas layer increases. If the mixing ratio of water ice reaches 10%, the maximum penetration depth is about $0.87R_U$. For Neptune, the maximum penetration depth of the zonal flow goes from $0.84R_N$ to $0.85R_N$ as the mixing ratio of water ice increases in the gas layer. The magnetic diffusivity at the maximum penetration depth is about 10^9 m^2 s. Take $U \sim 100$ m s^{-1} and $L \sim 10^6$ m, the corresponding magnetic Reynolds number is about $R_m \sim 0.1$. Thus, it is justified to use small Reynolds number assumption in this calculation.

From the three-layer model presented by Hubbard et al. (1991), the transition radius from the ice layer to the gas layer is about $0.8R_U$ for Uranus and $0.84R_N$ for Neptune. Therefore, if the maximum penetration depth of the zonal flow is the same as the transition radius, the penetrated zonal flow can be truncated naturally at the large density variation ice-gas transition radius and total Ohmic dissipation is less than the planetary net luminosity. However, if the maximum penetration depth of the zonal flow above the transition radius, the penetrated zonal flow needed to be truncated by some forces to avoid producing excessive Ohmic dissipation. From order of magnitude analysis in the previous sections (4.2), we know that the Lorentz force is not large enough to truncate to the flow at the maximum penetration depth. Therefore, some other forces need to be large enough to truncate the flow; otherwise, the presumed penetrating zonal flow does not exist.
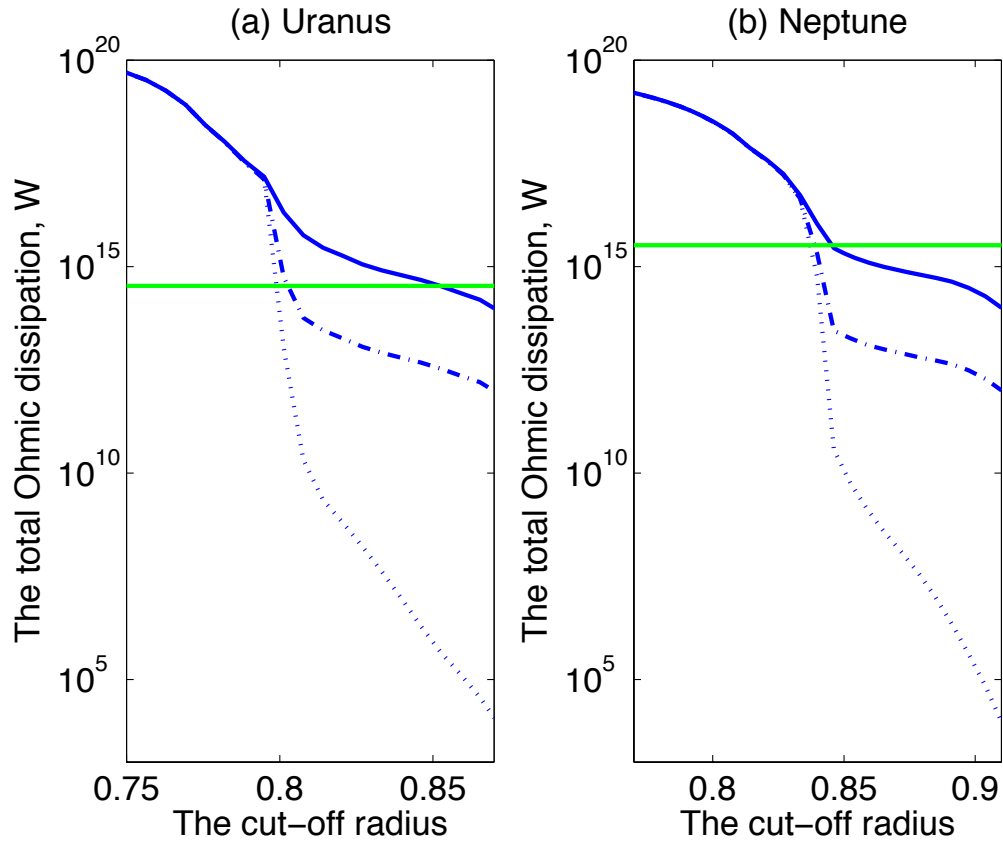
Figure 4.2 Here we assume that the observed zonal flow penetrates to the deep interior along the cylinders. The flow has to be truncated at a certain radius to prevent production of excessive Ohmic dissipation. This figure shows the total Ohmic dissipation versus the scaled truncation radius: (a) Uranus; (b) Neptune. The solid blue curves show calculated total Ohmic dissipation if water-ice is confined in the "ice" layer; the dash-line show total Ohmic dissipation if the mixing ratio of water ice in the "gas" layer is 0.1%; the dot-line show total Ohmic dissipation if the mixing ratio of water ice in the "gas" layer is 10%. The green horizontal line shows the planetary total luminosity, which is 0.034×10^{17} W for Uranus and 0.33×10^{17} W for Neptune (Guillot, 2005). The maximum penetration depth of the zonal flow is reached when the total Ohmic dissipation produced by the flow matches the planet's net luminosity. For Uranus, the maximum penetration depth increases from $0.80R_U$ to $0.87R_U$ as the mixing ratio of water ice increases; For Neptune, the maximum penetration depth increases from $0.84R_N$ to $0.85R_N$ as the mixing ratio of water ice increases.

Chapter 5   Interaction of magnetic field and shear flow

5.1   Abstract

Giant planets in our solar system have both strong external magnetic fields and large near surface zonal flows. In this paper, we consider some simple zonal flows and investigate their modification by the magnetic field in both a Cartesian geometry and a spherical geometry. We find that the magnetic field tends to reduce the magnitude of velocity and velocity shear. The dimensionless number characterizing this interaction is the Chandrasekhar number. In a spherical geometry a deep-seated zonal flow can arise even though the driving force for the flow is confined in the surface layer. The penetrating zonal flow has much smaller amplitude than the observed zonal flow and is reduced by the magnetic field in the deep interior.

5.2   Introduction

Giant planets in our solar system show strong azimuthal flow on the surface. These winds might be powered by the solar energy or internal heat left over from the planetary formation or both. The flows contain both large-scale and small-scale motions. The typical horizontal length scale for large-scale motions is about ~ 5000 km; and it is about ~ 100 km or even smaller for small-scale motions. Small surface features usually last for only a few hours or days, but large features often last for decades or centuries (Ingersoll, 1990). A complete understanding of the formation mechanism of the zonal flow needs to consider the heat transport and fluid motion in a wide range of length scales and timescales in three dimensions, which is a tremendous task. Therefore the form and the magnitude of the driving force for the zonal

flow are still largely unknown despite extensive studies (Vasavada & Showman, 2005).

Giant planets also have strong external magnetic fields: about 4.2 G in the equatorial region of Jupiter; and 0.2 G in the equatorial region of Saturn, Uranus and Neptune. These strong magnetic fields are assumed to be generated in the high electrical conducting interior. For Jupiter and Saturn, shockwave experiments indicate that hydrogen experiences a continuous transition from an insulator to a conductivity of 2×10^5 S m^{-1} (Nellis et al., 1996); For Uranus and Neptune, the high electrical conductivity material is the water ice, whose conductivity increases exponentially with pressure and temperature until reaching 10^3 S m^{-1}(Nellis et al., 1988). The interaction between the fluid and the magnetic field is important in the fluid envelope and changes the outgoing magnetic field as well as the fluid structure.

The outstanding questions are: what is the response of the fluid to different driving forces? How does magnetic field interact with zonal flow? In a spherical geometry, if we drive the flow in the surface layer, will the flow be able to penetrate to the deep interior? If so, will the flow take the form of Taylor-Proudman cylinders? In this chapter, we consider several simple driving mechanisms for the zonal flow and study the flow structure in both a Cartesian geometry and a spherical geometry. After that, we conduct dynamical consistent calculations to investigate the interaction of magnetic field and zonal flow in those systems.

5.3 Interaction of magnetic field with shear flow in a Cartesian geometry

In this section, we investigate the interaction of magnetic field and shear flow in the following Cartesian geometry: a fluid with certain electrical conductivity distribution is confined between two parallel plates; the x-direction is parallel to the plates and the z-direction is perpendicular to the plates. The flow is driven along the x-direction,
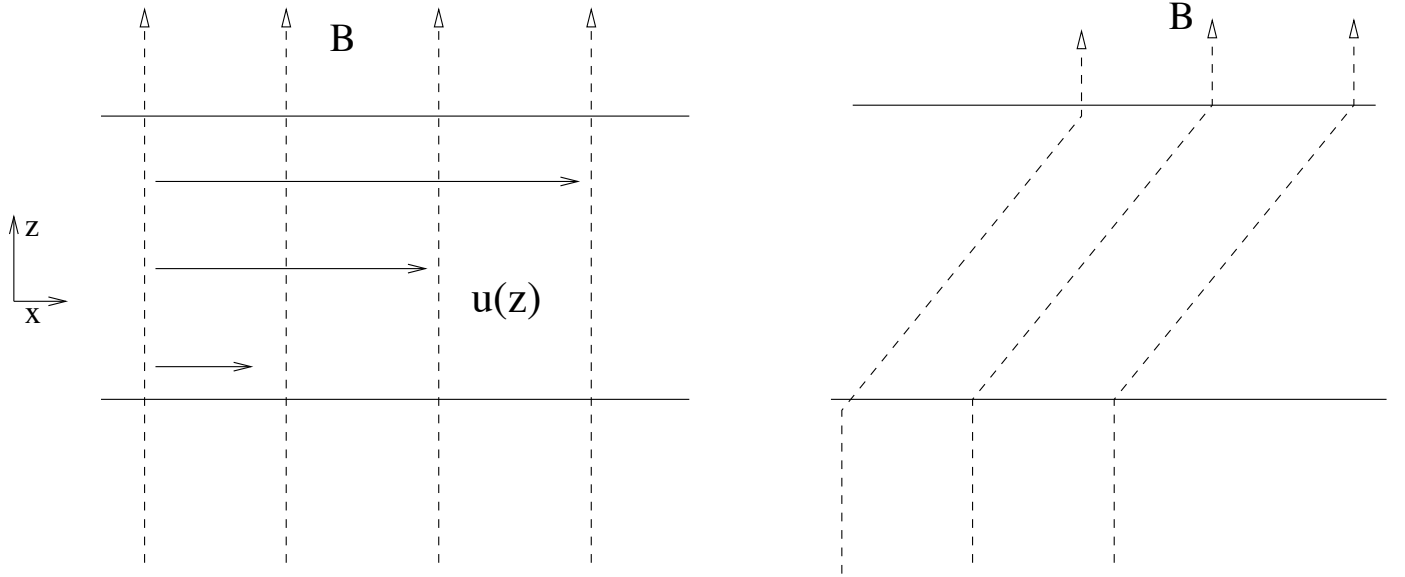
Figure 5.1 (a) The Cartesian geometry; (b) The magnetic field lines after considering interaction between magnetic field and shear flow.

and a uniform magnetic field is imposed uniformly along the z-direction (see figure (5.1a)).

5.3.1 Driving the flow by boundary stress: constant magnetic diffusivity

Consider the simplest case, where the fluid has constant parameters and is driven by a boundary stress σ at the top plate. In this case, the interaction of the horizontal flow and the imposed vertical magnetic field induces a magnetic field in the horizontal direction (Figure (5.1b)). In steady state, the governing equations are the Navier-Stokes equation including the Lorentz force and the magnetic induction equation

$$0 = \frac{\partial}{\partial z}\left[\nu\frac{\partial U}{\partial z} + \frac{B_0 B}{\mu_0 \rho}\right], \tag{5.1}$$

and

$$0 = B_0\frac{\partial U}{\partial z} + \lambda\frac{\partial^2 B}{\partial z^2}. \tag{5.2}$$

Here U is the velocity along the x-direction; B_0 is the imposed uniform magnetic field along the z-direction; B is the induced magnetic field along the x-direction; ν is the kinematic viscosity; λ is the magnetic diffusivity; μ_0 is the magnetic permeability. Scale equations (5.1) and (5.2) in the following way: $[B] \sim B_0$; $[U] \sim U_0$; and $[z] \sim L$ where L is the domain size along the z-direction. The scaled equations are

$$\frac{\partial}{\partial z}\left[\frac{\partial U}{\partial z} + \Lambda_{lorentz}B\right] = 0; \tag{5.3}$$

and

$$R_m\frac{\partial U}{\partial z} + \frac{\partial^2 B}{\partial z^2} = 0. \tag{5.4}$$

The dimensionless numbers are defined as

$$\Lambda_{lorentz} = \frac{B_0^2 L}{\nu U_0 \mu_0 \rho}, \tag{5.5}$$

and,

$$R_m = \frac{U_0 L}{\lambda}, \tag{5.6}$$

where $\Lambda_{lorentz}$ is the ratio of the Maxwell stress to the viscous stress; and R_m represents the ratio of the magnetic field generation to diffusion.

A non-slip boundary condition is used at bottom and a shear stress σ is applied at the top. Without considering the imposed magnetic field B_0, the steady state solution requires that $\sigma L/\nu U_0 \rho = 1$ and the nondimensional velocity is the uniform shear flow

$$U = z. \tag{5.7}$$

If the applied magnetic field along the z-direction is not zero ($B_0 \neq 0$), the steady state solution for the Navier-Stokes equation with the above velocity boundary conditions satisfies

$$\frac{\partial U}{\partial z} + \frac{Q}{R_m}B - 1 = 0, \tag{5.8}$$

Combining with the steady state magnetic induction equation, we obtain

$$\frac{\partial^2 B}{\partial z^2} - QB + R_m = 0,$$

(5.9)

where

$$Q = R_m \Lambda_{lorentz} = \frac{B_0^2 L^2}{\nu \lambda \mu_0 \rho}$$

(5.10)

is the Chandrasekhar number. Since the horizontal induced magnetic field is only confined in the finite electrical conducting region, and the area outside of the parallel plates is assumed to be insulating, B goes to zero at both top and bottom boundaries. The solutions of equation (5.8) and (5.9) are

$$B(z) = \frac{R_m}{Q} \left(1 - \frac{\cosh \sqrt{Q}(z - 1/2)}{\cosh \sqrt{Q}/2} \right),$$

(5.11)

and

$$U(z) = \frac{\left[\sinh \sqrt{Q}(z - 1/2) + \sinh \sqrt{Q}/2 \right]}{\sqrt{Q} \cosh \sqrt{Q}/2}.$$

(5.12)

The flow is thus entirely determined by Q, and does not depend separately on R_m and $\Lambda_{lorentz}$. The field structure is also determined entirely by Q, and the peak value of R_m/Q is obtained (for $Q \gg 1$).

Figure (5.2) shows the solution for various Q. The magnitude of the velocity is reduced as Q increases. Define velocity amplitude reduction $\Re_r$ as the ratio of the velocity at the top boundary ($z = 1$) with imposed magnetic field to that without magnetic field. For $Q \gg 1$, $\Re_r \propto Q^{-1/2}$. In the middle of the domain, the velocity shear reduction is proportional to $\exp(-\sqrt{Q})$. Since the magnitude of the induced horizontal magnetic field goes to zero at both the top and bottom boundary, the velocity shear at both boundaries is the same with or without imposed vertical magnetic field (See equation (5.8)). Thus, the thickness of the boundary layer is $\sim 1/\sqrt{Q}$. The magnitude of the induced horizontal magnetic field reaches maximum in the middle of two plates. If $Q \gg 1$, the maximum value of R_m/Q corresponds to balancing the
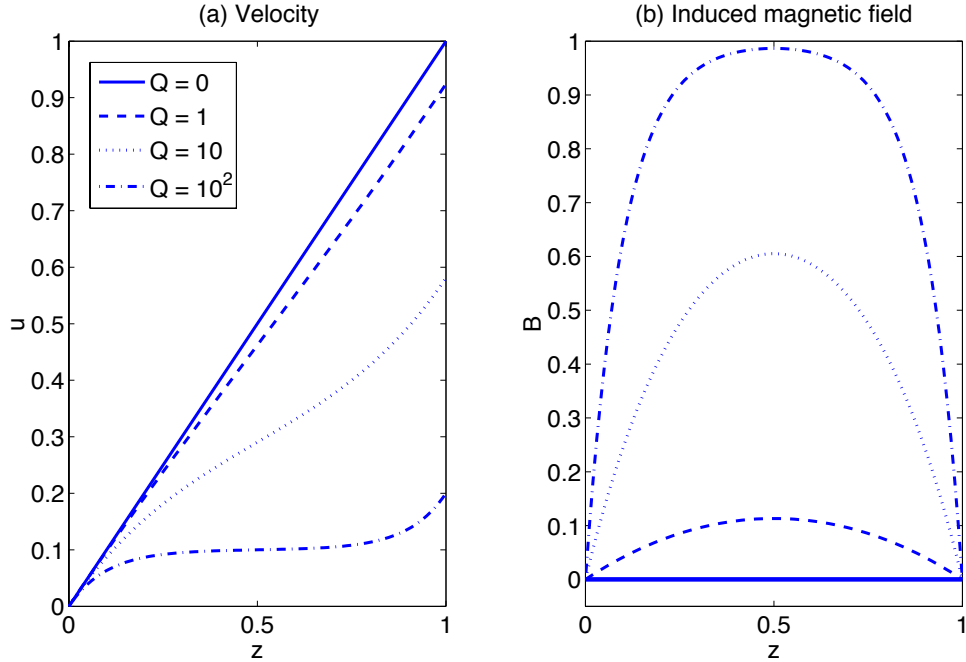
Figure 5.2 The interaction of the magnetic field and the shear flow for constant magnetic diffusivity. (a) Velocity versus height; (b) Induced horizontal magnetic field versus height. The induced magnetic field B is scaled to R_m/Q. For $Q \gg 1$, the velocity amplitude reduction is proportional to $Q^{-1/2}$ and the maximum value of R_m/Q corresponds to balancing the viscous and Maxwell stress, i.e., $B_0 B/\mu_0 \sim \sigma$ in dimensional units. The velocity shear is everywhere exponentially small except in the thin boundary layer of thickness $\sim 1/\sqrt{Q}$.

viscous and Maxwell stress, i.e., $B_0 B/\mu_0 \sim \sigma$ in dimensional units.

5.3.2 Driving the flow by boundary stress: variable magnetic diffusivity

In the interiors of the giant planets, the magnetic diffusivity of material increases exponentially from the high electrical conducting region towards the surface:

$$\lambda = \lambda_0 \exp(z\beta), \tag{5.13}$$

where λ_0 is the magnetic diffusivity at the metallic hydrogen region and $1/\beta$ is the scale height of the magnetic diffusivity. In this case, the magnetic induction equation can be rewritten as

$$\frac{\partial^2 B}{\partial z^2} + \beta \frac{\partial B}{\partial z} + R_m \frac{\partial U}{\partial z} = 0, \tag{5.14}$$

where the dimensionless number R_m is defined as: $R_m = U_0 L / \lambda_0 \exp(\beta z)$. Combining with the Navier-Stokes equation (5.8), we have:

$$\frac{\partial^2 B}{\partial z^2} + \beta \frac{\partial B}{\partial z} - QB + R_m = 0, \tag{5.15}$$

where Q is the local Chandrasekhar number defined as:

$$Q_{local} = \frac{B_0^2 L^2}{\mu_0 \rho \nu \lambda_0 \exp(\beta z)}. \tag{5.16}$$

The solutions for different scale heights are shown in figure (5.3). The reduction of velocity is proportional to $Q_{local}^{-1/2}$.

5.3.3 Driving the flow with variable body forces: constant magnetic diffusivity

We consider driving the flow by the following body force:

$$\mathbf{F} = 12 U_0 \nu \left(z - \frac{L}{2} \right) \frac{1}{L^3} \mathbf{e}_x, \tag{5.17}$$

which has zero mean along the z-direction. Reynolds stress, thermal wind, etc., have the same property. The non-dimensionalized governing equations are

$$\frac{\partial^2 U}{\partial z^2} + \frac{Q}{R_m} \frac{\partial B}{\partial z} + 12 \left(z - \frac{1}{2} \right) = 0, \tag{5.18}$$

and,

$$\frac{\partial^2 B}{\partial z^2} + R_m \frac{\partial U}{\partial z} = 0, \tag{5.19}$$
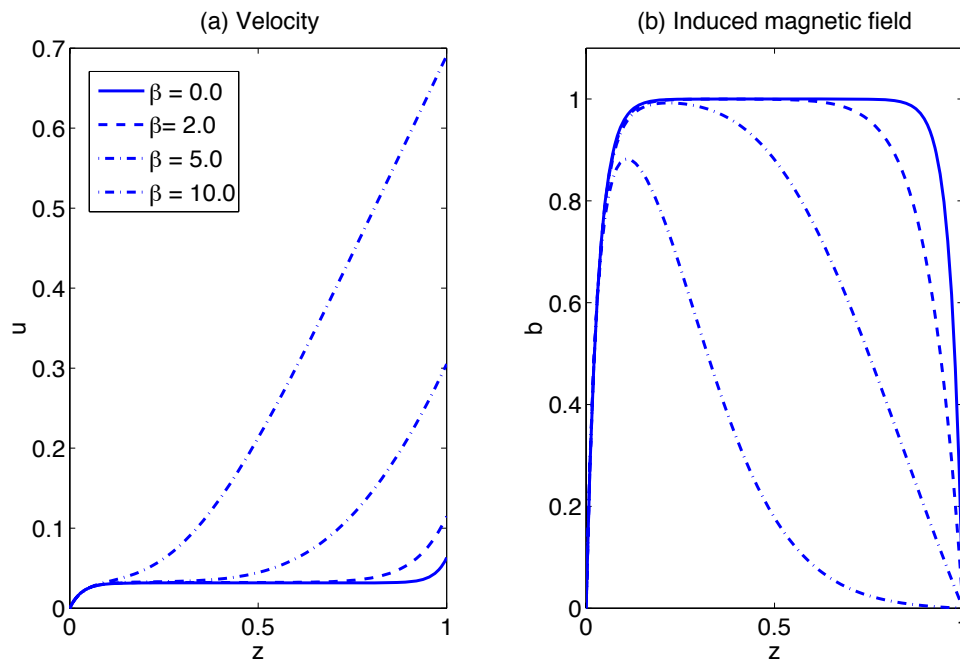
Figure 5.3 Interaction of the magnetic field and the shear flow for various magnetic diffusivities with different scale heights: $\lambda = \exp(\beta z)$, where β is taken to be: $0.0, 2.0, 5.0, 10.0$. Here, $Q = 10^3$ and the induced magnetic field is scaled to Q/R_m. (a) Velocity versus height; (b) Induced toroidal magnetic field versus height. Reduction of the velocity is concentrated in the region with large Q.

where the dimensional number R_m and Q is defined in equation (5.6) and (5.10) respectively. Without imposing the magnetic field, the solution for the Navier-Stokes equation in steady state is:

$$U(z) = -2z^3 + 3z^2. \tag{5.20}$$

It has the following properties: $U = 0$ at $z = 0$; $U = U_0$ at $z = 1$ and stress free $(dU/dz = 0)$ at both boundaries. In this case, a viscous boundary layer does not exist. It is quite different from driving the flow by boundary stress, because there is no obligation to have thin layers with high velocity shear.

If a uniform magnetic field is imposed along the z-direction, the magnetic field reduce the magnitude of the velocity. As in the previous calculation, we assume the induced magnetic field along the x-direction goes to zero at both top and bottom boundaries. The solutions for equation (5.18) and (5.19) are:

$$U(z) = \frac{C \cosh(\sqrt{Q}(1-z))}{\sqrt{Q}\cosh Q} - \frac{12 \sinh \sqrt{Q}z}{\sqrt{Q^3}\cosh Q} + \frac{12}{Q}z - \frac{C}{Q}, \tag{5.21}$$

and,

$$B(z) = \frac{Q}{R_m}\left[\frac{12\cosh\sqrt{Q}z - 12}{Q\cosh\sqrt{Q}} + \frac{\sinh(\sqrt{Q}(1-z)) - \sinh\sqrt{Q}}{\cosh\sqrt{Q}}C - 6z^2 + (2C+6)z\right], \tag{5.22}$$

where the constant C is defined as:

$$C = \frac{12\left(\cosh\sqrt{Q} - 1\right)}{Q\left(2\cosh\sqrt{Q} - \sinh\sqrt{Q}\right)}. \tag{5.23}$$

Similar as driving the fluid by boundary stress, both the velocity and the structure of the magnetic field are entirely determined by Q. For $Q \gg 1$, we have: $C \approx 12/Q$ and $U(z = 1) \approx 12/Q$. The velocity amplitude reduction is:

$$\Re_r \propto \frac{1}{Q}. \tag{5.24}$$
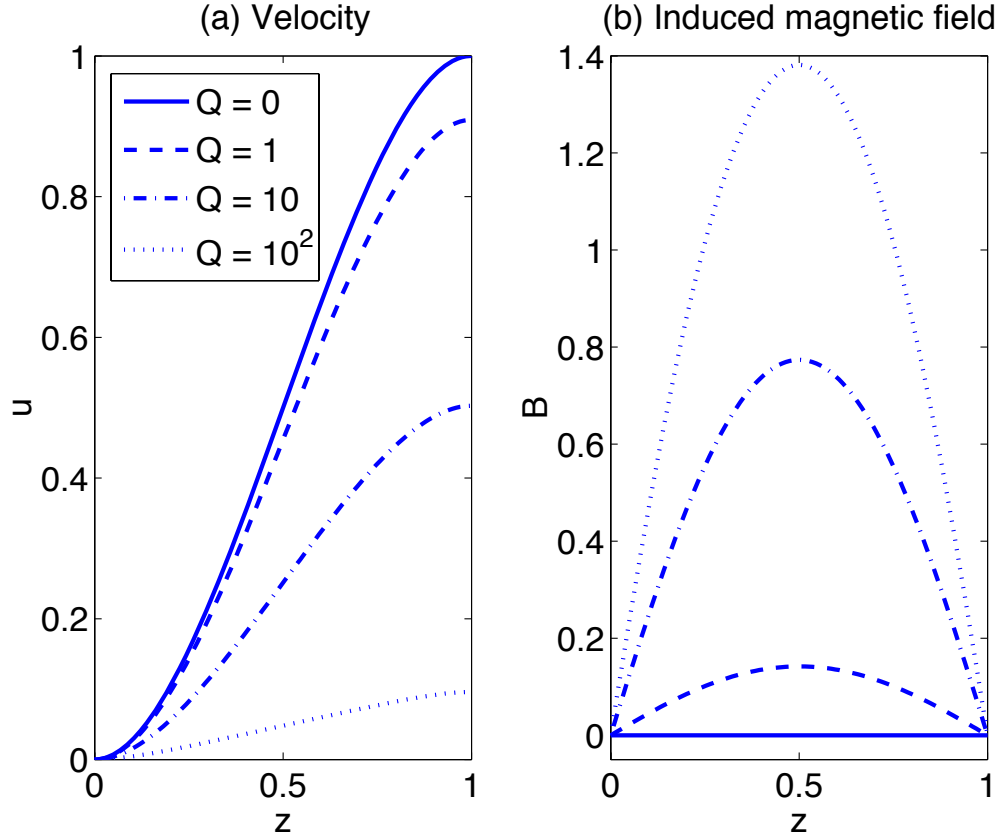
Figure 5.4 Interaction of magnetic field and shear flow if we drive the flow with vertically varying body force(See equation (5.17)) for different Q. (a) Velocity; (b) Induced magnetic field. B is scaled to R_m/Q. The velocity shear is everywhere reduced by $1/Q$ relative to the zero field case.

The velocity shear in the middle of the domain is,

$$\frac{dU}{dz} \propto \frac{1}{Q}. \tag{5.25}$$

The peak value of the induced magnetic field is obtained in the middle of the domain with the value: Q/R_m.

The interactions of the magnetic field and the shear flow for different magnetic diffusivities are shown in figure (5.4). Driving the flow by a body force is fundamentally different from driving the flow by a boundary stress. In the case of boundary stress forcing, the velocity shear is everywhere exponentially small except in thin boundary
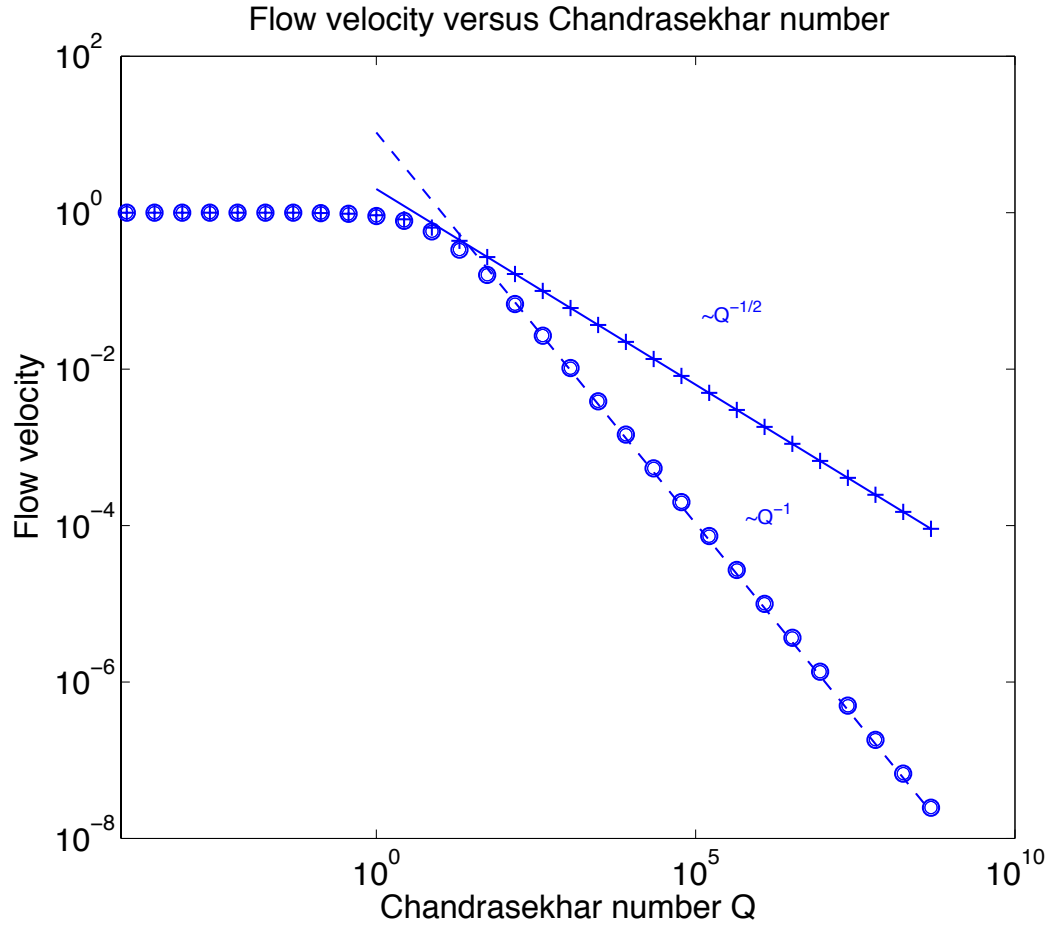
Figure 5.5 Flow velocity versus Chandrasekhar number for different driving forces. Interaction of flow and magnetic field is characterized by Q. If the flow is driven by boundary stress, the reduction of the velocity is proportional to $Q^{-1/2}$. If the flow is driven by body force, the reduction of the velocity is proportional to Q^{-1}. The fundamental difference between these two cases is the role of boundary layers.

layers of thickness $\sim \frac{1}{\sqrt{Q}}$, where it must reach the zero field values. In the case of a body force, the velocity shear is actually larger except near the boundaries and is everywhere reduced by $1/Q$ relative to the zero field case. The velocity difference between the two boundaries is much smaller in the body force case (assuming $Q \gg 1$) because the region where the induced field is small is not a region where the velocity shear is forced to be large.

Figure (5.5) indicates that the reduction of the velocity becomes significant when

$Q > 10$. For the interior of Jupiter and Saturn, the magnetic diffusivity increases exponentially outward the metallic hydrogen region, where other parameters only change slowly in the radial direction. The magnitude of viscosity in the interior is quite uncertain. For Jupiter and Saturn, the eddy viscosity estimation based on the mixing length theory gives: $\nu \sim 10^3$ m s^{-2}. However, if the observed zonal flow penetrates to the deep interior along cylinders, the eddy viscosity has to be smaller than ~ 0.25 m^2 s^{-1} for avoiding producing excessive dissipation due to the relative motions of the cylinders (Ingersoll & Pollard, 1982).

For Jupiter and Saturn, we use radial profiles of density and magnetic diffusivity, and take L to be the scale height of the magnetic diffusivity: $L \sim 10^3$ km; B_0 to be the magnitude of the observed dipole magnetic field, which is 4.2 G for Jupiter and 0.2 G for Saturn. The Chandrasekhar number Q as a function of r for different choices of eddy viscosity is shown in figure (5.6). The reduction of the flow is significant below $0.97 R_J$ for Jupiter and $0.89 R_S$ for Saturn if $\nu \sim 0.25$ m s^{-2}. If $\nu \sim 10^3$ m s^{-2}, the reduction of the velocity becomes significant below $0.96 R_J$ and $0.85 R_S$.

5.4 Interaction of the magnetic field with the zonal flow in a spherical geometry

In this section, we investigate the interaction of the magnetic field with the zonal flow in a spherical geometry. We consider driving of the flow by some simple forces in the surface layer. An example would be winds driven by latitudinal temperature gradients. Can a flow that is driven by the force concentrated in the surface layer penetrate to the deep interior? If the flow can penetrate to the deep interior, will this flow interact with the deep-seated planetary magnetic field? How does this interaction change the structure of the flow and the outgoing magnetic field? In order to answer these questions, we assume that the planetary magnetic field is generated in the high electrical conducting region, and there is a low conducting spherical shell
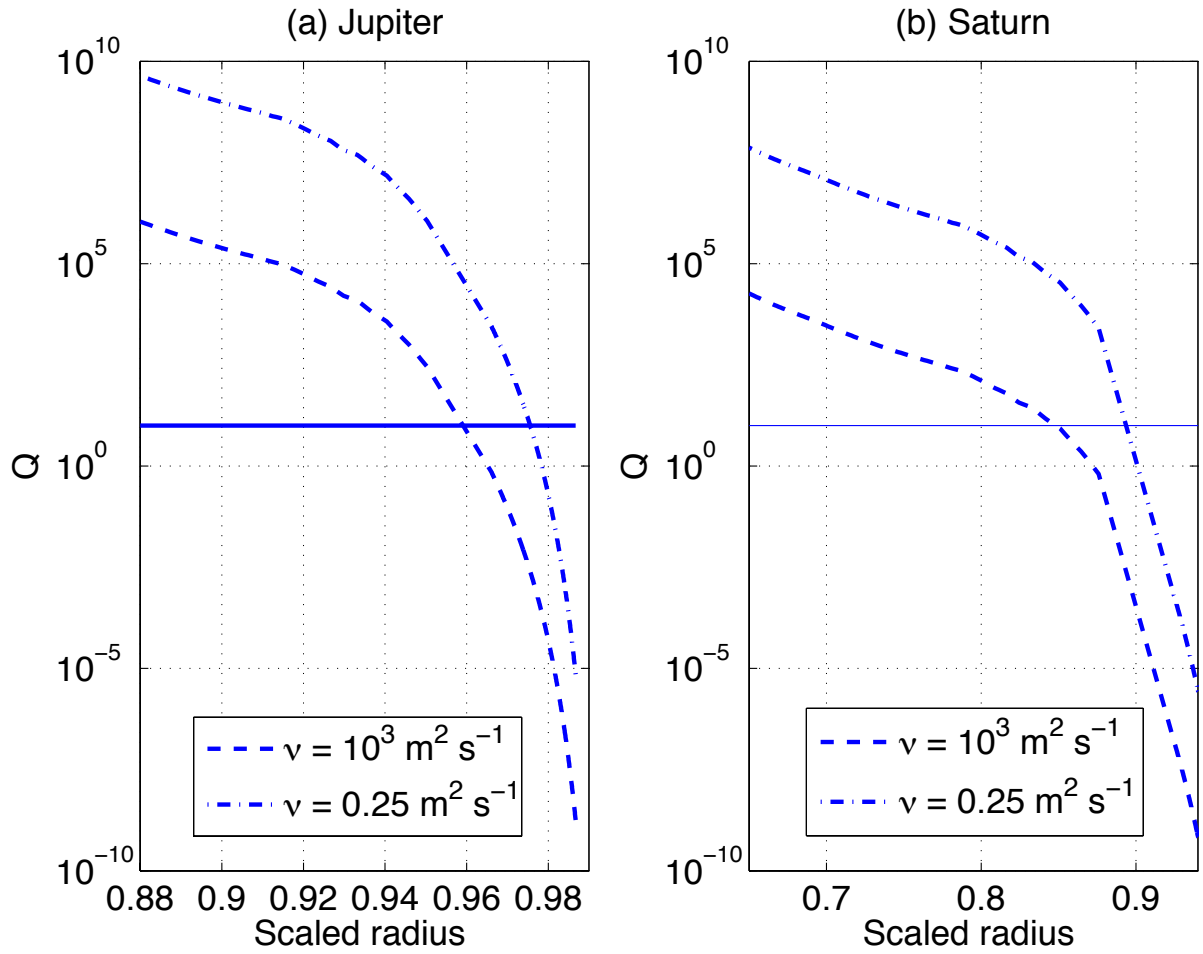
Figure 5.6 The Chandrasekhar number as a function of radius for Jupiter and Saturn. (a) Jupiter; (b) Saturn. If the viscosity is taken to be 0.25 m^2 s^{-1}, Q is larger than 10 below $0.92R_J$ for Jupiter and below $0.72R_S$ for Saturn. However, if $\nu \sim 10^3$ m s^{-2}, the reduction of the velocity becomes significant below $0.96R_J$ and $0.85R_S$.

outside of the dynamo generation region. For Jupiter, the high electrical conductivity region lies below $0.84R_J$ where the hydrogen transitions from the semi-conducting to metallic state. In Saturn, the corresponding radius is $0.63R_S$. We then consider the modification of the flow structure in the low conducting spherical shell by outgoing magnetic field and modification of outgoing magnetic field by the flow.

Consider a spherical shell with thickness $0.7R \sim 1.0R$ where R is the radius of the planets. Define two coordinate systems: spherical coordinate $(\mathbf{e}_r, \mathbf{e}_\theta, \mathbf{e}_\phi)$ and cylindrical coordinate $(\mathbf{e}_s, \mathbf{e}_z, \mathbf{e}_\phi)$, where $\mathbf{e}_r$ is the unit vector along radial direction; $\mathbf{e}_\theta$ is along meridional direction; $\mathbf{e}_s$ is along cylindrical radial direction; $\mathbf{e}_z$ is along the rotation axis of the planets and $\mathbf{e}_\phi$ is along azimuthal direction. Under the Boussinesq approximation, the Navier-Stokes equation can be written as

$$\frac{\partial \mathbf{U}}{\partial t} + (\mathbf{U} \cdot \nabla) \mathbf{U} + 2\Omega(\mathbf{e}_z \times \mathbf{U})$$
$$= -\frac{\nabla P}{\rho} + \frac{1}{\mu_0 \rho} (\nabla \times \mathbf{B}) \times \mathbf{B} + \nu \nabla^2 \mathbf{U} + \frac{\mathbf{F}}{\rho}, \tag{5.26}$$

where Ω is the rotation frequency of the planet; $\mathbf{U}$ is the velocity field; $\mathbf{B}$ is the magnetic field; P is the pressure; ρ is the density; μ_0 is the magnetic permeability; ν is the kinematic viscosity; and $\mathbf{F}$ is the driving force. For simplicity, we apply the driving force in the surface layer along the radial direction:

$$\mathbf{F} = F_0 \sin(\theta)\mathbf{e}_r, \quad \text{if} \quad r > R_0, \tag{5.27}$$

and

$$\mathbf{F} = 0. \quad \text{if} \quad r \leq R_0, \tag{5.28}$$

where R_0 is an adjustable parameter that defines the "surface layer". For rapidly rotating planets, the zonal flow (flow along the azimuthal direction) can be generated even the force is only applied along the radial direction because of the influence of the Coriolis force. The driving force is stronger in the equatorial region and weaker near the polar region, which is consistent with the latitudinal distribution of solar heating.

For variable electrical conductivity distribution, the magnetic induction equation can be written as

$$\frac{\partial \mathbf{B}}{\partial t} = \nabla \times (\mathbf{U} \times \mathbf{B}) - \nabla \times (\lambda \nabla \times \mathbf{B}). \tag{5.29}$$

Scale the equations (5.26) and (5.29) as: $[t] \sim \frac{1}{\Omega}$; $[\nabla] \sim \frac{1}{L}$; $[U] \sim \Omega R$; $[B] \sim B_0$; $[\lambda] \sim \lambda_0$; $[P] \sim \rho(\Omega L)^2$. Here, L is the thickness of the spherical shell; B_0 is the observed poloidal magnetic field; λ_0 is the magnetic diffusivity at the high electrical conducting region. The scaled Navier-Stokes equation and magnetic induction equation are

$$\frac{\partial \mathbf{U}}{\partial t} + (\mathbf{U} \cdot \nabla)\mathbf{U} + 2(\mathbf{e}_z \times \mathbf{U}) = -\nabla P + \Lambda (\nabla \times \mathbf{B}) \times \mathbf{B} + E_\nu \nabla^2 \mathbf{U} + \Gamma \mathbf{F}, \tag{5.30}$$

and

$$\frac{\partial \mathbf{B}}{\partial t} = \nabla \times (\mathbf{U} \times \mathbf{B}) - E_\lambda \nabla \times (\lambda \nabla \times \mathbf{B}). \tag{5.31}$$

Here the dimensionless number Λ evaluates the ratio of Lorentz force to Coriolis force:

$$\Lambda = \frac{B_0^2}{\mu_0 \rho (\Omega L)^2}; \tag{5.32}$$

Γ is the ratio of driving force to Coriolis force:

$$\Gamma = \frac{F_0}{\Omega U_0 \rho}. \tag{5.33}$$

E_ν evaluates the magnitude of viscous diffusion to Coriolis force and E_λ is the ratio of magnetic diffusion to Coriolis force:

$$E_\nu = \frac{\nu}{\Omega L^2}; \tag{5.34}$$

and

$$E_\lambda = \frac{\lambda_0}{\Omega L^2}. \tag{5.35}$$

For Jupiter, we take: $B_0 \sim 10^{-3}$ Tesla; $\rho \sim 1$ kg m^{-3}; $\Omega \sim 2 \times 10^{-4}$ s^{-1}; $L \sim 2 \times 10^7$ m; $\lambda_0 \sim 4$ m^2 s^{-1}, which corresponds to a conductivity of 2×10^5 S m^{-1}. Thus, $\Lambda \approx 10^{-5}$,

$E_\lambda \approx 10^{-5}$, and $E_\nu \approx (10^{-10} \sim 10^{-7})$, which depends on the choice of the viscosity. In the interior of Jupiter and Saturn, it ranges from 0.25 m^2 s^{-1} (Ingersoll & Pollard, 1982) to 10^3 m^2 s^{-1} (from mixing length estimation). However, in the actual numerical simulations, both E_λ and E_ν have to be many orders of magnitude larger than that in the interior of the planets to stabilize the numerical scheme (Glatzmaier & Roberts, 1995). Thus, other dimensionless parameters need to be correspondingly larger to approach the correct regime for the planets.

For an incompressible fluid, we have $\nabla \cdot \mathbf{U} = 0$; Thus, the velocity field can be decomposed into its toroidal and poloidal components:

$$\mathbf{U} = \nabla \times (e\mathbf{r}) + \nabla \times \nabla \times (f\mathbf{r}), \tag{5.36}$$

where e and f can be expanded in spherical harmonics:

$$e = \sum_l \sum_{m=0}^{l} e(r) P_l^m (\cos(\theta)) \exp(im\phi); \tag{5.37}$$

and

$$f = \sum_l \sum_{m=0}^{l} f(r) P_l^m (\cos(\theta)) \exp(im\phi). \tag{5.38}$$

Take the curl of the scaled Navier-Stokes equation (5.30). The $\mathbf{e}_r$ component of the equation can be written as

$$\begin{aligned}
+ &\sum_l \sum_{m=0}^{m=1} \left[\frac{\partial}{\partial t} \left(\frac{l(l+1)}{r^2} e(r) P_l^m (\cos(\theta)) \exp(im\phi) \right) \right] \\
+ &\sum_l \sum_{m=0}^{m=1} \left[\nu \left(-\frac{l(l+1)}{r^2} L_l e(r) P_l^m (\cos(\theta)) \exp(im\phi) \right) \right] \\
= &\ \mathbf{e}_r \cdot \left[\nabla \times \left(-(\mathbf{U} \cdot \nabla)\mathbf{U} - 2(\mathbf{e}_z \times \mathbf{U}) + \Lambda(\nabla \times \mathbf{B}) \times \mathbf{B} + \Gamma\mathbf{F} \right) \right],
\end{aligned} \tag{5.39}$$

and

$$+ \sum_l \sum_{m=0}^{m=l} \left[-\frac{\partial}{\partial t} \left(\frac{l(l+1)}{r^2} L_l f(r) P_l^m (\cos(\theta)) \exp(im\phi) \right) \right]$$

$$+ \sum_l \sum_{m=0}^{m=l} \left[-\nu \frac{l(l+1)}{r^2} L_l L_l f(r) P_l^m \left(\cos(\theta) \right) \exp(im\phi) \right]$$
$$= \mathbf{e}_r \cdot \left[\nabla \times \nabla \times \left(-(\mathbf{U} \cdot \nabla)\mathbf{U} - 2(\mathbf{e}_z \times \mathbf{U}) + \Lambda(\nabla \times \mathbf{B}) \times \mathbf{B} + \Gamma\mathbf{F} \right) \right], \quad (5.40)$$

where L_l is defined as

$$L_l = \frac{d^2}{dr^2} - \frac{l(l+1)}{r^2}. \qquad (5.41)$$

Stress-free boundary conditions for the velocity field are used on both the top and bottom boundaries. They require:

$$U_r = 0, \quad \frac{\partial}{\partial r}\left(\frac{U_\theta}{r}\right) = 0, \quad \frac{\partial}{\partial r}\left(\frac{U_\phi}{r}\right) = 0 \quad \text{at} \quad r = r_i, r_o, \qquad (5.42)$$

where r_i is the radius for the inner boundary and r_o is the radius for the outer boundary. In the high electrical conducting dynamo generation region, the magnetic field lines are fixed in the flow and the relative velocity between the flow and magnetic field are small. This would suggest that there is no shear at the base; however the simulation does not explicitly deal with the difficult question of how to match to the core dynamos. Accordingly, this is an assumption, not a rigorously justified choice.

Similarly, for the magnetic field, $\nabla \cdot \mathbf{B} = 0$. Therefore, the magnetic field $\mathbf{B}$ can be decomposed into its toroidal and poloidal components:

$$\mathbf{B} = \nabla \times (g\mathbf{r}) + \nabla \times \nabla \times (h\mathbf{r}), \qquad (5.43)$$

where g and h can be expanded in spherical harmonics:

$$g = \sum_l \sum_{m=0}^{m=l} g(r) P_l^m \left(\cos(\theta) \right) \exp(im\phi), \qquad (5.44)$$

and

$$h = \sum_l \sum_{m=0}^{m=l} h(r) P_l^m \left(\cos(\theta) \right) \exp(im\phi). \qquad (5.45)$$

Since the magnetic diffusivity is only a function of radius $\lambda = \lambda(r)$ in the interior of

the giant planets, we take curls of the magnetic induction equation and obtain

$$\sum_l \sum_{m=0}^{m=l} \left[\frac{l(l+1)}{r^2} P_l^m \left(\cos(\theta) \right) \exp(im\phi) \left[\frac{\partial h(r)}{\partial t} - \lambda(r) L_l h(r) \right] \right]$$
$$= \mathbf{e}_r \cdot \left[\nabla \times (\mathbf{U} \times \mathbf{B}) \right], \qquad (5.46)$$

and

$$\sum_l \sum_{m=0}^{m=1} \left[\frac{l(l+1)}{r^2} P_l^m \left(\cos(\theta) \right) \exp(im\phi) \left[\frac{\partial g(r)}{\partial t} - \lambda(r) L_l g(r) - \lambda'(r) g'(r) \right] \right]$$
$$= \mathbf{e}_r \cdot \left[\nabla \times \nabla \times (\mathbf{U} \times \mathbf{B}) \right]. \quad (5.47)$$

Since electrical conducting material is confined inside the planet, we choose the outer boundary condition to be insulating. The magnetic field generated in the high electrical conductivity region contains both a poloidal component and a toroidal component. Since the toroidal magnetic field cannot be observed on the planetary surface, we choose the magnetic field at the inner boundary of the spherical shell to be poloidal field only.

Equations (5.39), (5.40), (5.46) and (5.47) can be solved simultaneously by the spectral element method, where spherical harmonics expansion is used in θ and ϕ direction and Chebyshev polynomials are used in r-direction. The basic numerical program has been developed by Hollerbach (2000) for constant density and magnetic diffusivity. Here we improved the numerical program to allow for variable magnetic diffusivity.

First, we consider the structure of the flow without the magnetic field and assume that the flow is axisymmetric. The driving force is along the radial direction and confined in the surface layer(See equation (5.27) and (5.28)). Due to the influence of the Coriolis force, the large flow along the zonal direction in the surface layer is produced. Even though the force is zero outside of the surface layer, a small amount of the momentum can still be transported downward from the surface layer.

The time evolution of the azimuthal flow at two random separated internal points for different Ekman numbers E_ν is shown in figure (5.7). The spherical coordinates (r, θ) for those two points are $(0.85R, 71°)$ and $(0.90R, 127°)$. The system undergoes rapid oscillations initially before settling down to the steady state. The Ekman number $E_\nu = \frac{\nu}{\Omega L^2}$ is the ratio of the rotational timescale to viscous timescale. For $E_\nu = 10^{-3}$, the viscous timescale is 10^3 times of the rotation timescale. From figure (5.7a), we see that the system reaches the steady state at 500 rotation timescale $(\propto \frac{1}{2E_\nu})$. Similarly, for $E_\nu = 10^{-4}$, the viscous timescale is 10^4 times of the rotation timescale and the system reaches the steady state at 5000 rotation timescale. The timescale for reaching the steady state is proportional to inverse Ekman number $(T \propto \frac{1}{E_\nu})$.

The axisymmetric velocity field ($\mathbf{U}$) can be decomposed into its zonal component and meridional component

$$\mathbf{U} = v\mathbf{e}_\phi + \nabla \times (\Psi\mathbf{e}_\phi), \tag{5.48}$$

where v and Ψ are two scalar functions. Also,

$$\nabla \times (\Psi\mathbf{e}_\phi) = \left(\frac{1}{r \sin\theta} \frac{\partial}{\partial\theta} (\sin\theta\Psi) , -\frac{1}{r} \frac{\partial}{\partial r} (r\Psi) , 0 \right), \tag{5.49}$$

and

$$\nabla (\Psi r \sin\theta) = \left(\sin\theta \frac{\partial}{\partial r} (r\Psi) , \frac{\partial}{\partial\theta} (\sin\theta\Psi) , 0 \right). \tag{5.50}$$

Combining equation (5.49) and (5.50) yields

$$\nabla \times (\Psi\mathbf{e}_\phi) \cdot \nabla (\Psi r \sin\theta) = 0, \tag{5.51}$$

which implies that $(\Psi r \sin\theta)$ is perpendicular to the meridional flow $\nabla \times (\Psi\mathbf{e}_\phi)$ and $\Psi r \sin\theta$ is the stream function for the meridional circulation.
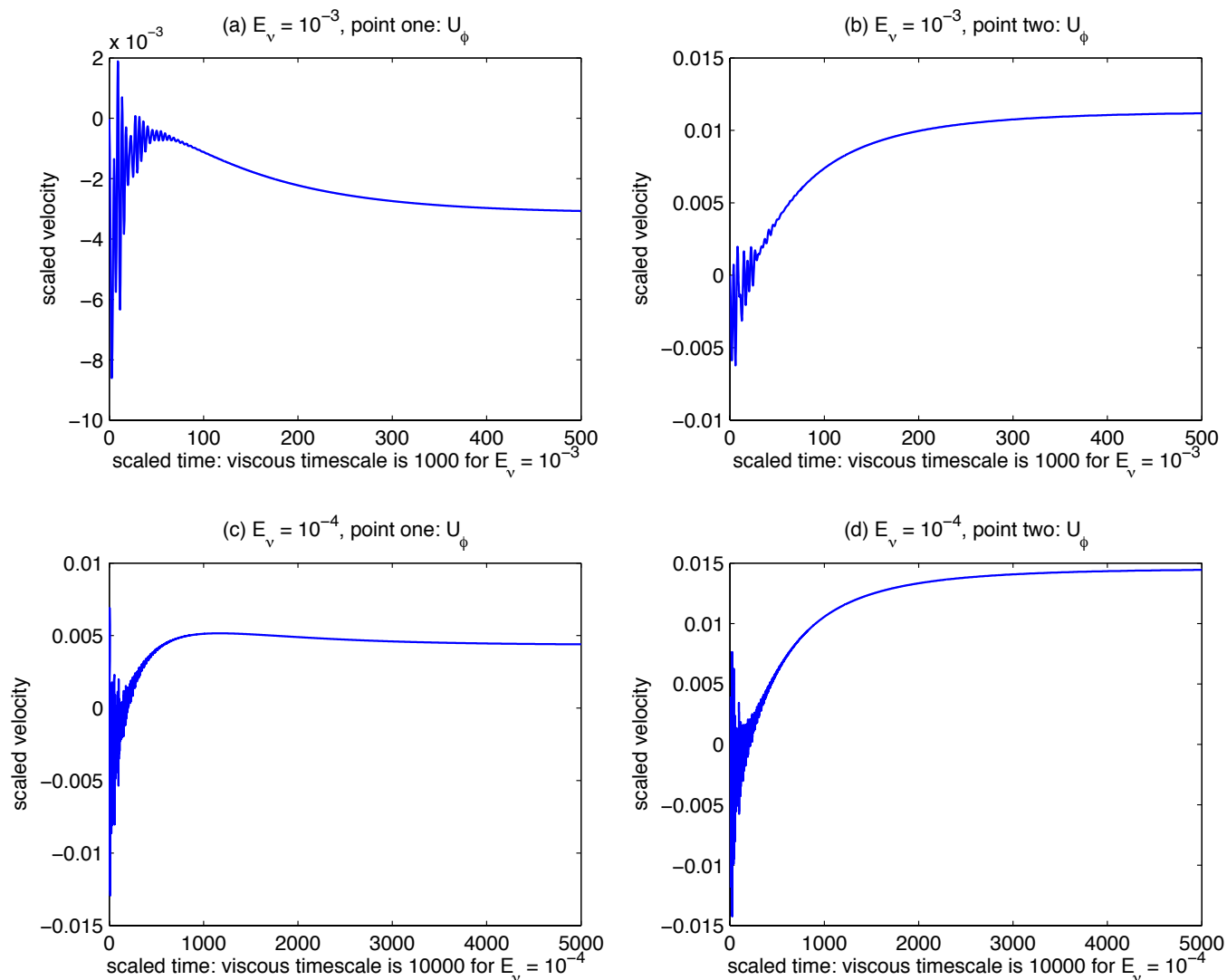
Figure 5.7 The time evolution of the azimuthal velocity for different Ekman numbers E_ν at two different separated points in the interior of the fluid domain far away from boundary. The spherical coordinate (r, θ) for point one is $(0.85R, 71°)$; and the spherical coordinate for point two is $(0.90R, 127°)$. (a) At point one $E_\nu = 10^{-3}$; (b) At point two $E_\nu = 10^{-3}$; (c) At point one $E_\nu = 10^{-4}$; (d) At point two $E_\nu = 10^{-4}$. The Ekman number $E_\nu = \frac{\nu}{\Omega L^2}$ is the ratio of the rotational timescale to viscous timescale. For $E_\nu = 10^{-3}$, the viscous timescale is 10^3 times of the rotation timescale. From figure (5.7a), we see that the system reaches the steady state at 500 rotation timescale. Similarly, for $E_\nu = 10^{-4}$, the viscous timescale is 10^4 times of the rotation timescale and the system reaches the steady state at 5000 rotation timescale. The timescale for reaching the steady state is proportional to inverse Ekman number ($T \propto \frac{1}{E_\nu}$).

For Ekman number $E_\nu = 10^{-3}$, the velocity field and the meridional stream function in steady state are shown in figure (5.8). Large meridional and azimuthal flows are concentrated in the surface layer $(r > R_o)$, where the force is applied. Here R_o is taken to be $0.95R$. However, in the region outside of the surface layer $(r < R_o)$ the magnitude of the flow is not zero despite the zero driving force. Small amount of the azimuthal flow can still penetrate from the surface layer to the deep interior along cylinders, consistent with the Taylor-Proudman theorem. In general, the velocity along the zonal direction is about one to two orders of magnitude larger than that along the meridional direction. For smaller E_ν, the ratio of the zonal velocity to the meridional velocity is larger.

Figure (5.9) shows the magnitude of the zonal flow velocity along the rotation axis for different cylindrical radii s. The magnitude of the penetrating flow is about 10% of the observed zonal flow.

For the same driving force, the amount of the penetrating zonal flow depends on the Ekman number E_ν. For smaller E_ν, the magnitude of the zonal flow in the surface layer is larger and the magnitude of the penetrating flow is also larger. The ratio of the surface flow to the penetrating flow for different Ekman number E_ν is shown in figure (5.10). This figure shows that the ratio of the internal to external flows is roughly independent of E_ν provided E_ν is sufficiently small.

Consider the influence of the magnetic field. In the interior of the gas giant planets, the magnetic diffusivity increases exponentially from the metallic hydrogen region: $\lambda = \lambda_0 \exp(\beta z)$, where λ_0 is the magnetic diffusivity in the metallic hydrogen region and $\frac{1}{\beta}$ is the scale height. From chapter 2, we know $\lambda_0 = 4$ m s^{-1} and the scale height of the magnetic diffusivity near the metallic region is about 1000 km. Comparing with the length scale $L \sim 2.0 \times 10^4$ km, we have: $\frac{1}{\beta} \sim 20$. First, assume that the deep-seated magnetic field is a dipolar field. Take $\Gamma \sim 1.0$, $E_\nu \sim 10^{-3}$ and
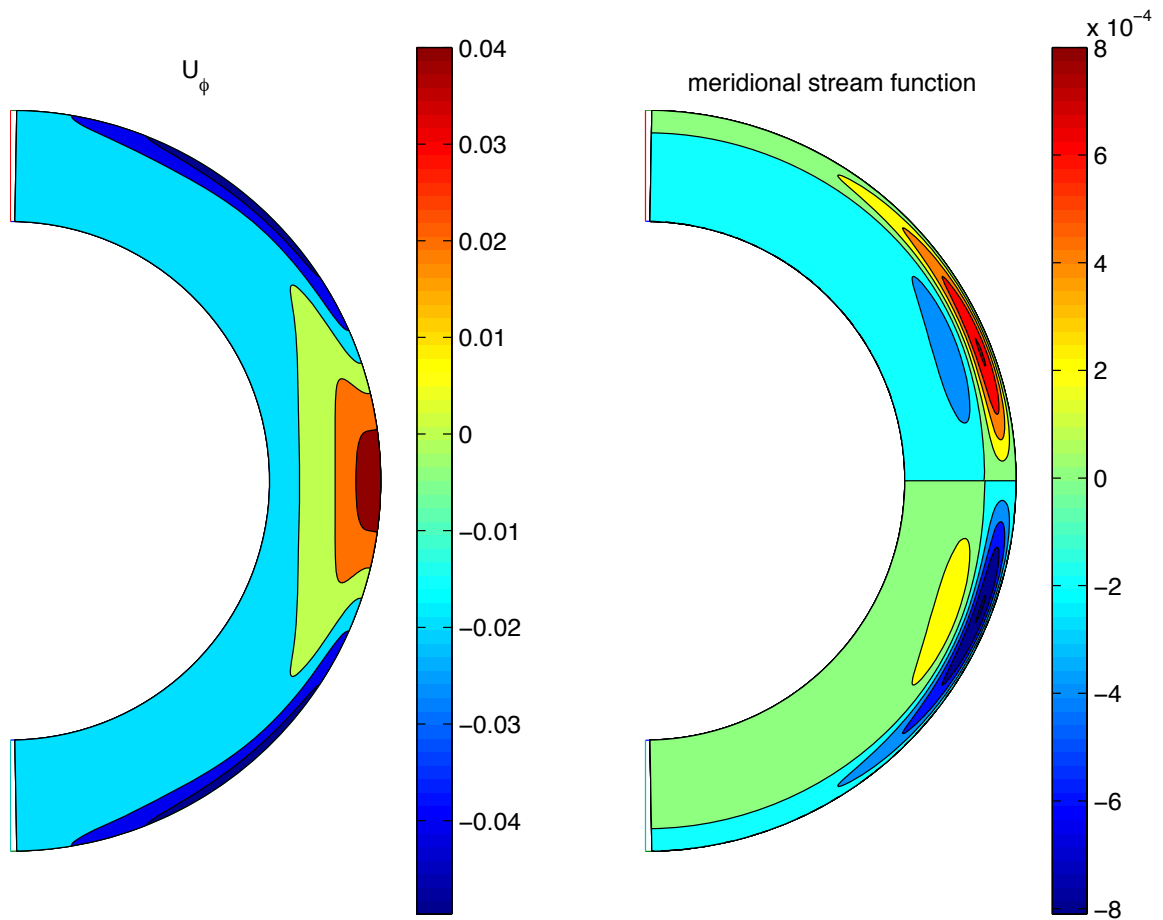
Figure 5.8 The general solution of the velocity in steady state for $E_\nu = 10^{-3}$. (a) The scaled zonal flow velocity U_ϕ; (b) the meridional stream function. Here the driving force is confined in the layer $r > R_o$, where R_o is taken to be $0.95R$. And, $\Gamma = 1.0$. The magnitude of the flow is not zero outside of the surface layer despite the zero driving force in this region.
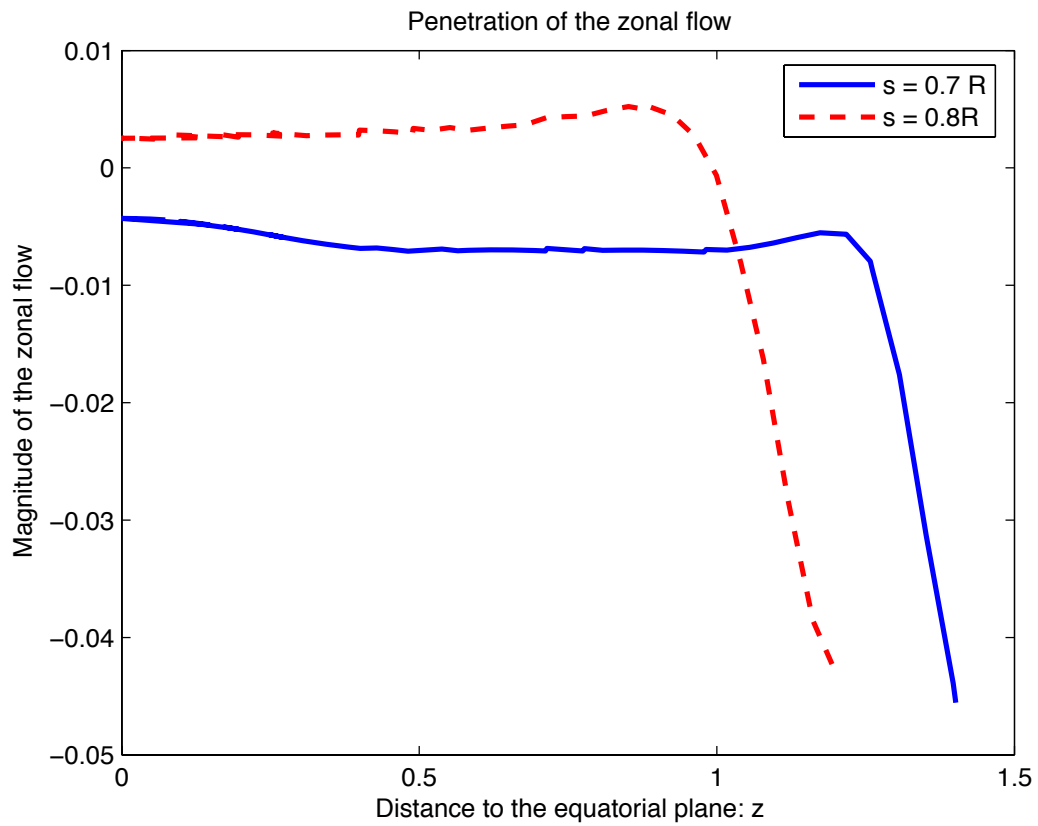
Figure 5.9 The magnitude of the azimuthal flow along the rotation axis for different cylindrical radius: $s = 0.7R$ and $s = 0.8R$. Here $E_\nu = 10^{-3}$ and $\Gamma = 1.0$.
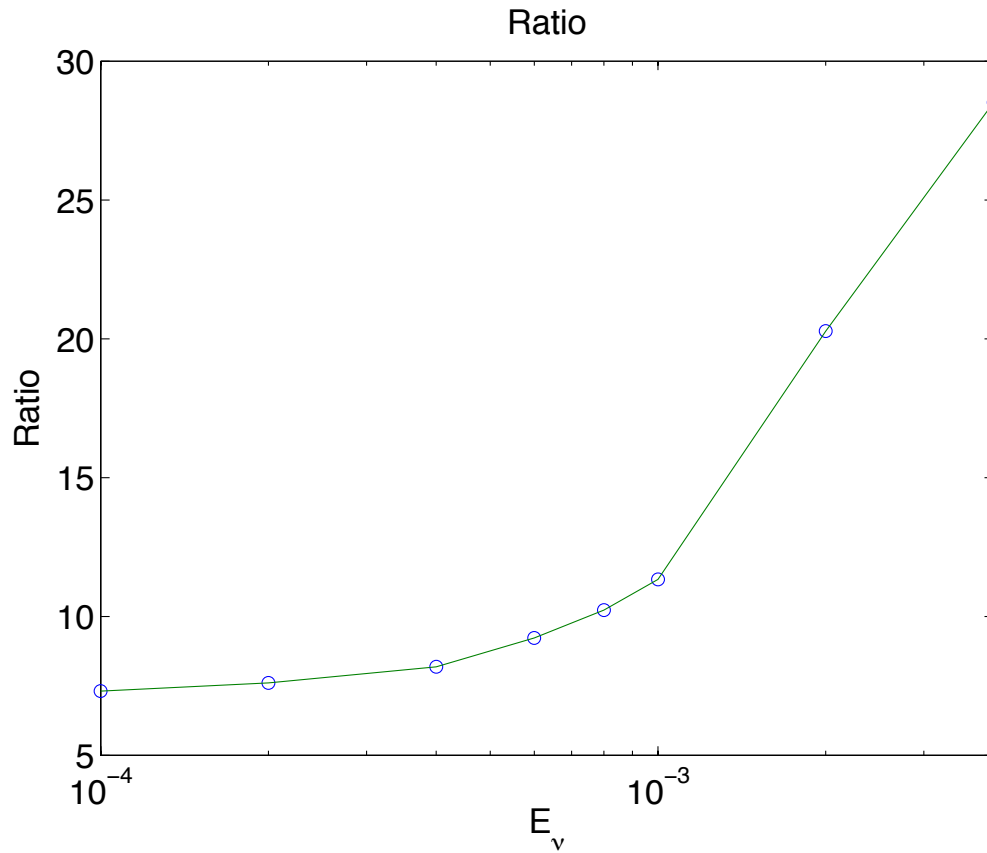
Figure 5.10 The ratio of the zonal flow on the surface to the penetrating flow for different E_ν. It is roughly independent of E_ν provided E_ν is sufficiently small. Here Γ is taken to be 1.0.

$E_\lambda \sim 10^{-3}$. Here $E_\lambda \sim 10^{-3}$ is corresponding to $\lambda_0 \sim 10^7$ S m, which is about seven orders of magnitude larger than the actual magnetic diffusivity near the metallic core region. We choose the unrealistically large E_λ for stabilizing the numerical scheme and increasing the time step for reaching the steady state solution faster. However, in order to simulate the interaction of the magnetic field and the flow, we have also chosen $\Lambda \sim 0.1$, which is several orders of magnitude higher than the actual value in the planetary interior (See equation (5.32)). The dynamically consistent solution for the velocity field and the magnetic field in steady state are shown in figure (5.11). The interaction between the magnetic field and zonal flow reduces the magnitude of the velocity shear and induces toroidal magnetic field at the high electrical conducting region. The reduction is larger near the equator and smaller in the polar region.

From figure (5.11), we see that the magnitude of the induced toroidal magnetic field is about one order of magnitude smaller than that of the pre-existing poloidal magnetic field. Since the magnitude of velocity shear is reduced due to the interaction with the magnetic field, the magnitude of the induced toroidal magnetic field is limited. The reduction of the zonal velocity shear by the magnetic field is illustrated more clearly in figure (5.12). With the magnetic field, the magnitude of the velocity shear is reduced to near zero at the high electrical conducting region.

The magnitude of the velocity in the giant planets is determined relative to the deep-seated planetary magnetic field. Since the velocity shear is reduced to near zero near the metallic hydrogen region, we can choose the velocity near the metallic hydrogen region to be zero velocity and determine the velocity in other regions relatively. Figure (5.13) shows the relative velocity distribution in the equatorial plane with and without the magnetic field. Both the magnitude of the velocity and the velocity shear are reduced significantly by the magnetic field in the high electrical conducting region.

Figure (5.14) shows the relative velocity distribution in the equatorial plane for different Λ, which is defined as $\Lambda = \frac{B_0^2}{\mu_0 \rho (\Omega L)^2}$ and is an evaluation for the Lorentz
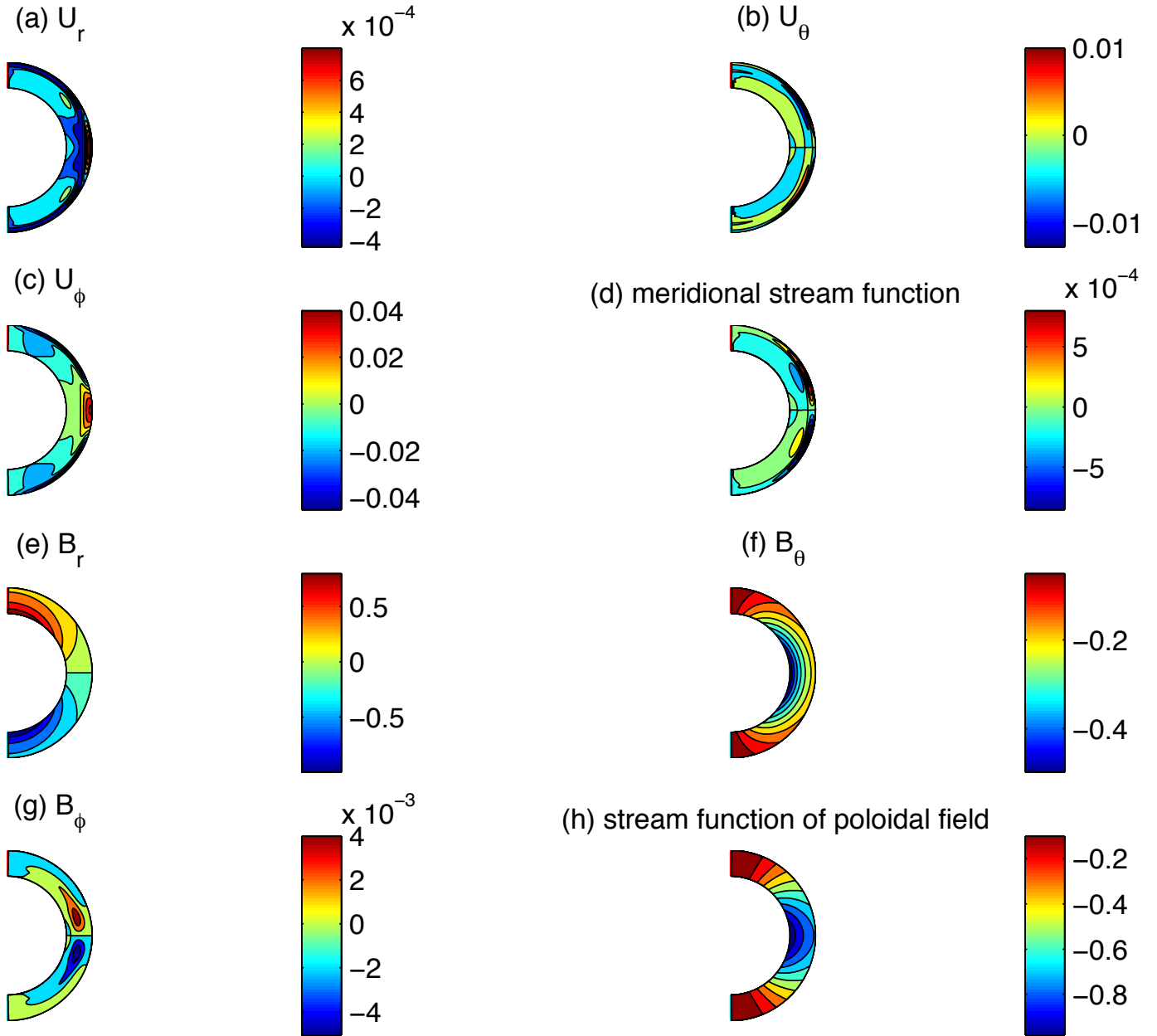
Figure 5.11 The solution with the deep-seated dipolar magnetic field and the variable magnetic diffusivity distribution: $\lambda = \exp(\beta z)$. Here the dimensionless numbers are taken to be: $\Gamma \sim 1.0$, $\Lambda \sim 1.0$, $E_\nu \sim 10^{-3}$ and $E_\lambda \sim 10^{-3}$. (a) U_r; (b) U_θ; (c) U_ϕ; (d) meridional stream function of velocity; (e) B_r; (f) B_θ; (g) B_ϕ; (h) meridional stream function of magnetic field. The interaction between the magnetic field and zonal flow reduces the magnitude of the velocity shear and induces toroidal magnetic field at the high electrical conducting region.
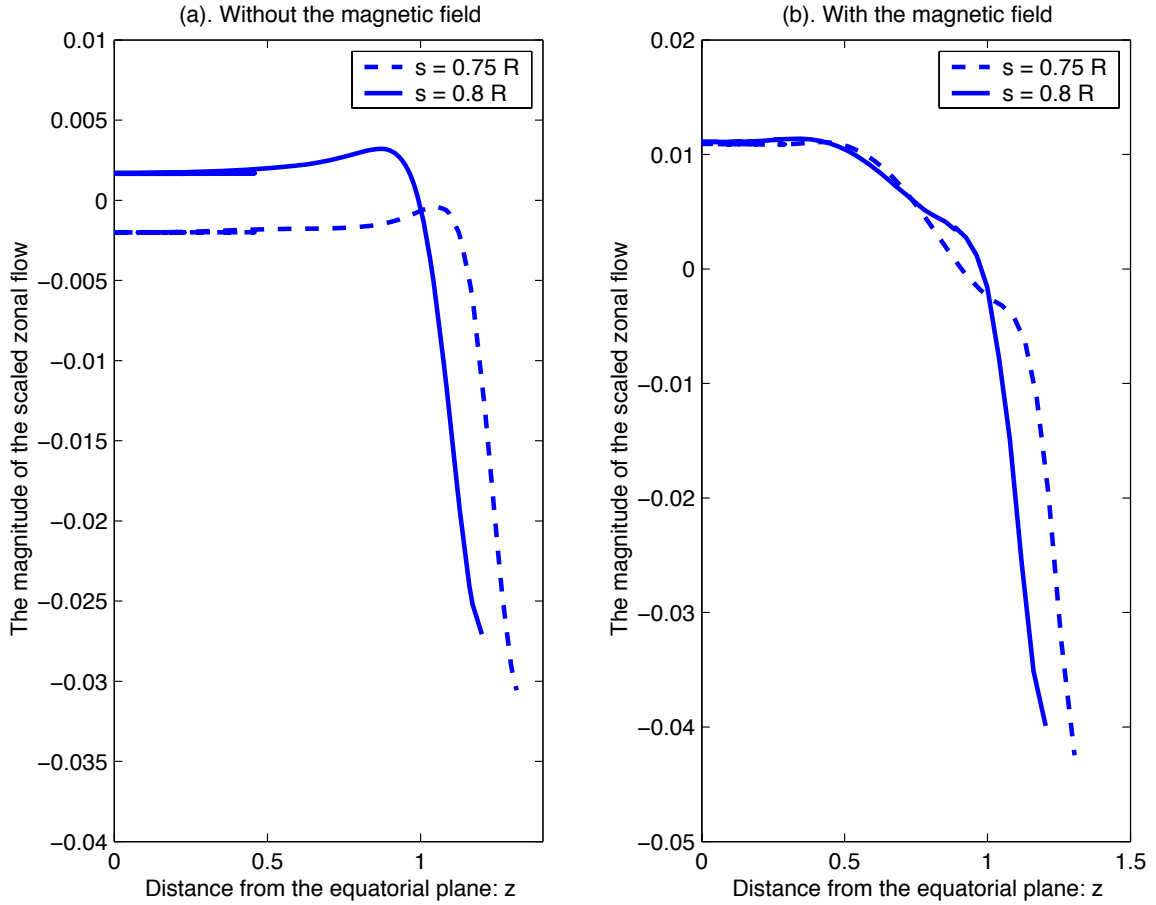
Figure 5.12 The magnitude of the zonal flow along the cylinders for different cylindrical radius. (a) Without the magnetic field. (b) with the magnetic field, $\lambda = \lambda_0 \exp 20(r - r_i)$, $\Lambda = 0.2$ and $E_\lambda = 10^{-3}$. In both cases, we take $E_\nu = 10^{-3}$ and $\Gamma = 1.0$. For the case with magnetic field, the curves for different cylindrical radius s nearly coincide at small z. This demonstrates the reduction of velocity shear by the magnetic field in the region with high electrical conductivity. The zonal flow at depth in this case should be identified with the rotation of the core.
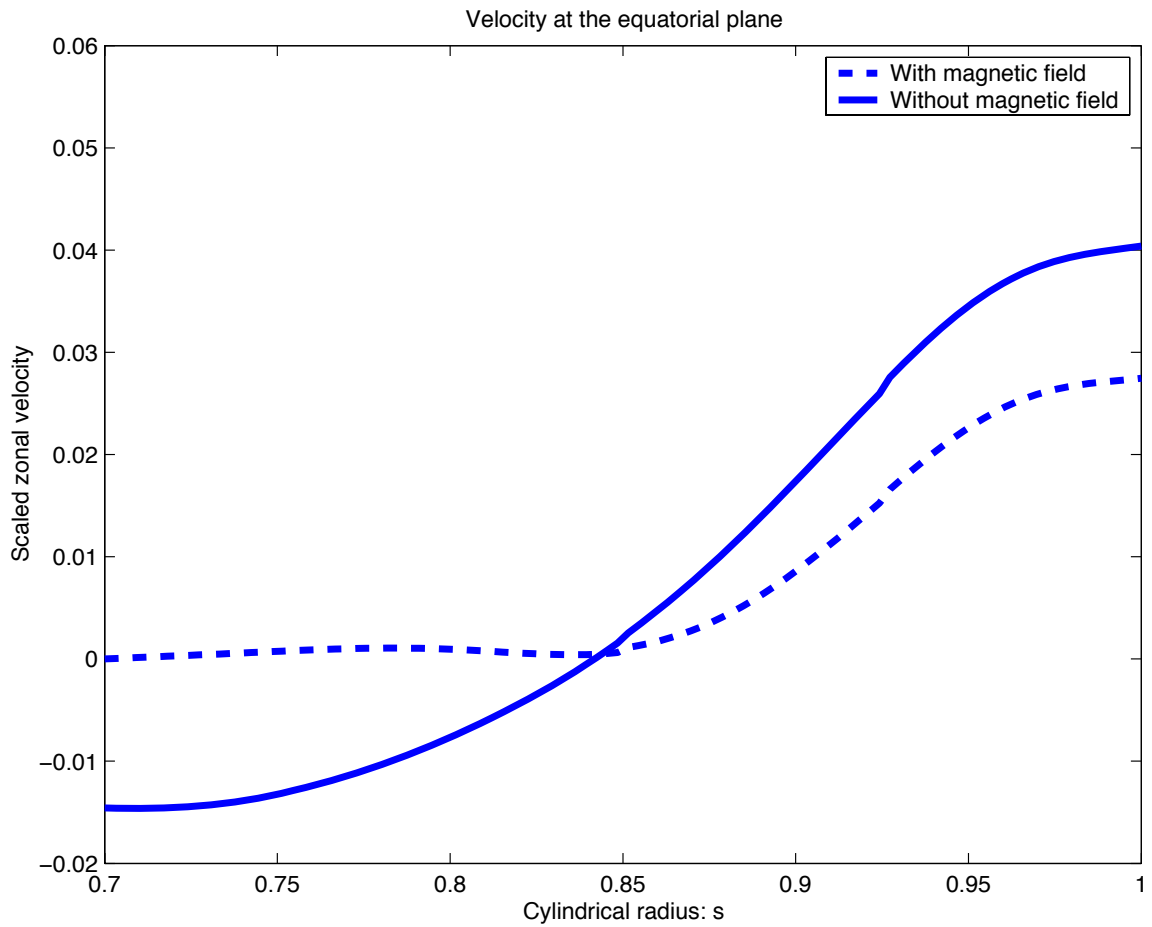
Figure 5.13 Relative velocity distribution in the equatorial plane. For the case with the magnetic field, $\lambda = \lambda_0 \exp 20(r - r_i)$, $\Lambda = 0.2$, $\Gamma = 1.0$, $E_\nu = 10^{-3}$ and $E_\lambda = 10^{-3}$. For the case without magnetic field $\Gamma = 1.0$, $E_\nu = 10^{-3}$.
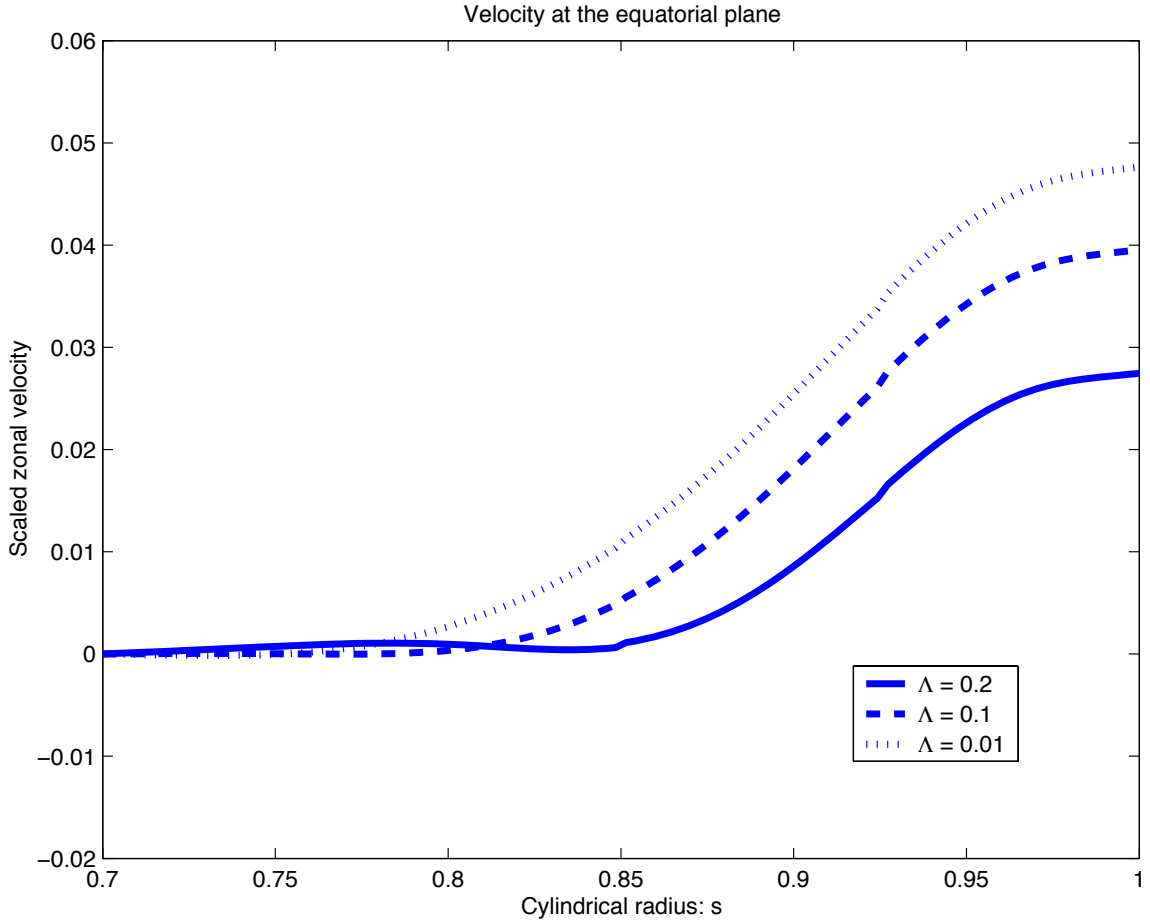
Figure 5.14 The relative velocity distribution in the equatorial plane for different Λ. Here, $\lambda = \lambda_0 \exp 20(r - r_i)$, $\Gamma = 1.0$, $E_\nu = 10^{-3}$ and $E_\lambda = 10^{-3}$. For large Λ, the Lorentz force is strong and the velocity shear reduction is more.

force. For large Λ, the Lorentz force is strong and the velocity shear reduction is more significant.

The analysis in Cartesian geometry indicates that the velocity reduction is proportional to the inverse of Chandrasekhar number Q. The local Q can be defined as

$$Q = \frac{B_0^2 L^2}{\mu_0 \lambda \rho \nu} = \Lambda \frac{1}{E_k} \frac{1}{E_\nu \exp(\beta(r - r_i))}. \tag{5.52}$$

Figure (5.15) shows the relative velocity distribution in the equatorial plane as a function of Q^{-1} for different Λ. The velocity distribution is roughly proportional to the inverse of the Chandrasekhar number providing Q is large enough.
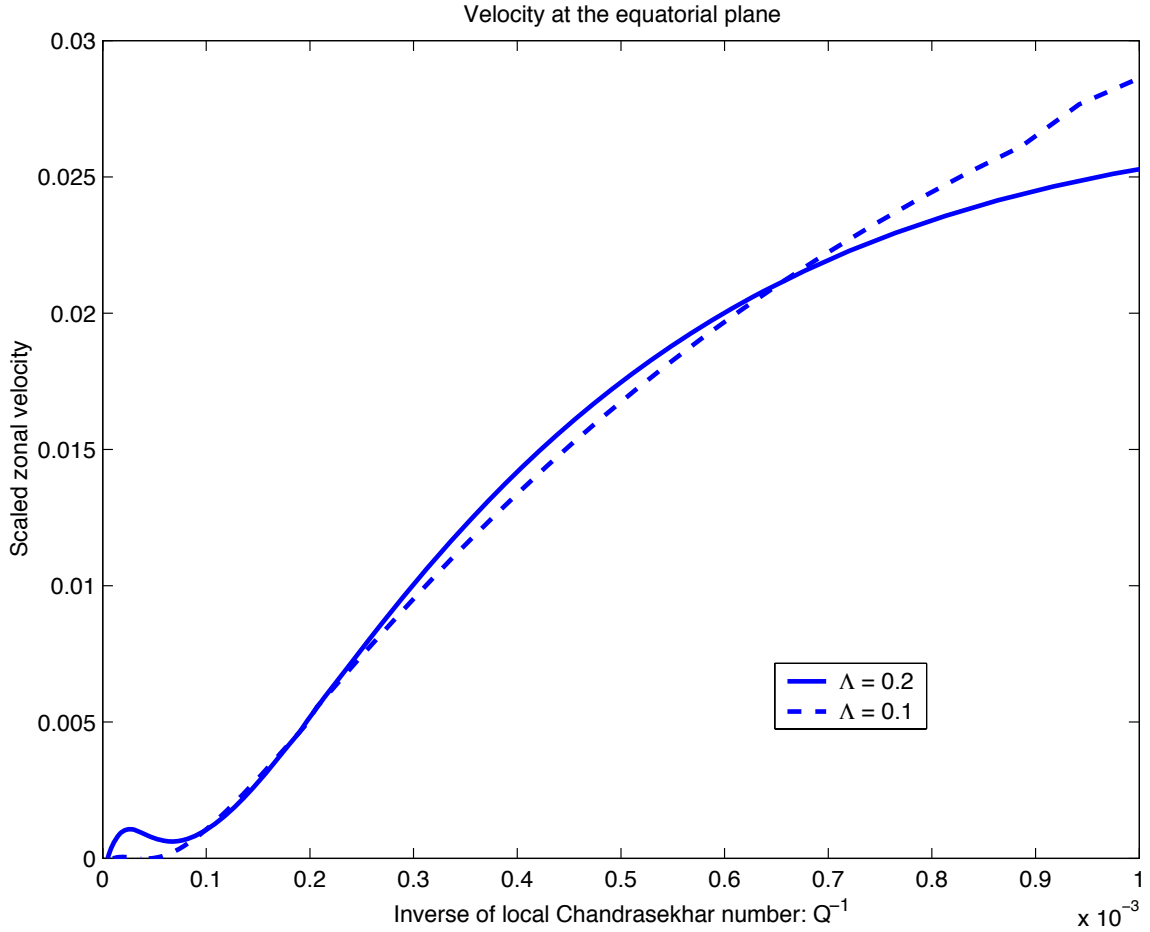
Figure 5.15 The relative velocity distribution in the equatorial plane as a function of Chandrasekhar number for different Λ. Here: $\lambda = \lambda_0 \exp 20(r - r_i)$, $\Gamma = 1.0$, $E_\nu = 10^{-3}$ and $E_\lambda = 10^{-3}$. For large enough Q, the velocity distribution is roughly proportional to the inverse of Chandrasekhar number.

5.5   Conclusion

In this chapter, we investigated the interaction of the magnetic field and shear flow in both a Cartesian geometry and a spherical geometry. The interaction of the magnetic field and shear flow will reduce both the magnitude of the velocity and the velocity shear. The dimensionless number that characterizes this interaction is the Chandrasekhar number. In a spherical geometry, we drive the flow in the surface layer.

However, a small amount of zonal flow still penetrates to the interior along cylinders and is reduced below by interaction with the magnetic field.

Chapter 6 Attenuation of non-asymmetric magnetic field in the outer shell of giant planets

6.1 Abstract

Planetary dynamos can generate magnetic fields with a variety of temporal and spatial variations. A fluid shell with sufficient electrical conductivity and azimuthal velocity shear outside of the dynamo generation region can attenuate the non-axisymmetric component of the magnetic field. However, the interaction of the axisymmetric component of the magnetic field and the zonal flow is able to reduce the magnitude of zonal flow. In this chapter, we investigate the attenuation of the non-axisymmetric magnetic field by magnetically limited zonal flow and find that the substantially different magnitudes of the axisymmetric magnetic fields on Jupiter and Saturn may produce different zonal flow shear. The smaller Saturnian field may allow a larger velocity shear and a greater attenuation of the non-axisymmetric field, thereby providing a possible explanation for the nearly axisymmetric field.

6.2 Introduction

Dynamo simulations suggest that the internal field has a wide range of temporal and spatial variations. A fluid layer with sufficient electrical conductivity and velocity shear outside of the dynamo generation region is able to attenuate the non-axisymmetric component of magnetic field (Stevenson, 1982). The amount of attenuation depends primarily on the magnetic Reynolds number within the layer.

As discussed in the last chapter, the interaction of the shear flow with the axisymmetric magnetic field reduces the magnitude of velocity shear. The reduction is characterized by Chandrasekhar number, which is defined as: $Q = B_0^2 L^2/\mu_0 \lambda \rho \nu$. Here B_0 is the magnitude of the observed axisymmetric magnetic field; L is the thickness of the fluid shell; μ_0 is the magnetic permeability; λ is the magnetic diffusivity and ν is the viscosity. The velocity shear reduction is larger for smaller Chandrasekhar number. This suggests a competition between two effects, both arising from the magnetic field. It is not clear that the magnetic limited zonal flow can still attenuate the non-axisymmetric magnetic field.

Jupiter and Saturn have similar internal structures (Guillot, 2005) and similar electrical conductivity distribution (see chapter 2). It is remarkable that Jupiter's observed dipole tilt is 100 times larger than that of Saturn. The spacecrafts' observations indicate that the magnitude of the axisymmetric dipolar field on the surface of Jupiter is about 4.2 G in the equatorial region and it is about 0.2 G in the equatorial region of Saturn. The internal difference in the magnitudes of the axisymmetric magnetic fields is large but imperfectly known. A factor of ~ 10 difference in the axisymmetric field results in a factor of ~ 100 difference in Chandrasekhar number and this can produce remarkably different zonal velocity shear reduction.

In this chapter, we study the attenuation of the non-axisymmetric magnetic field by magnetically limited zonal flow in both a Cartesian geometry and a spherical geometry. We treat the difference in the magnitude of the axisymmetric magnetic field on Jupiter and Saturn as given and investigate whether the different zonal velocity reduction produced by these magnetic field is able to produce large difference in attenuating the non-axisymmetric component of the magnetic field.

6.3 Attenuation of the non-axisymmetric magnetic field by the flow in a Cartesian geometry

We first investigate the attenuation of the non-axisymmetric magnetic field by flow in the Cartesian geometry (shown in figure (5.1) in chapter 5). The fluid with magnetic diffusivity λ is confined in two parallel plates. Let x be the direction parallel to the plate and z be the direction perpendicular to the plate. The fluid is driven along the x-direction. Instead of imposing a uniform magnetic field vertically, we apply a periodically x-dependent magnetic field along the z-direction: $(\mathbf{b} \propto b_0 \exp(ikx)\mathbf{e}_z)$, where k is the horizontal wavenumber. The flow in horizontal direction can attenuate the x-dependent magnetic field, which is similar to attenuating the outgoing non-axisymmetric magnetic field by zonal flow in the interior of giant planets. In this section, we first calculate the attenuation effect produced by the specified shear flow for both constant magnetic diffusivity and variable magnetic diffusivity, and illustrate the attenuation mechanism. We then apply a uniform magnetic field along the z-direction, which is able to reduce the velocity shear and conduct perturbation analysis to calculate the attenuation effect produced by the magnetically limited flow.

6.3.1 Attenuation produced by the specified shear flow: constant magnetic diffusivity

In steady state, the magnetic induction equation for constant magnetic diffusivity is

$$\nabla \times (\mathbf{u} \times \mathbf{b}) + \lambda \nabla^2 \mathbf{b} = 0. \tag{6.1}$$

Apply a periodically x-dependent magnetic field along the z direction: $(\mathbf{b} \propto b_0 \exp(ikx)\mathbf{e}_z)$ and specify uniform shear flow along the x direction: $u_x = z$. Scale the equation (6.1) in the following way: $[u] \sim u_0$, $[b] \sim b_0$ and $[\nabla] \sim \frac{1}{L}$, where L is the size of the domain. The scaled equation is

$$R_m \nabla \times (\mathbf{u} \times \mathbf{b}) + \nabla^2 \mathbf{b} = 0. \tag{6.2}$$

Here R_m is the magnetic Reynolds number: $R_m = u_0 L/\lambda$. In component form, the magnetic induction equation can be written as

$$\left[-k^2 b_z + \frac{d^2 b_z}{dz^2} \right] - ik R_m z b_z = 0; \tag{6.3}$$

Using $\nabla \cdot \mathbf{b} = 0$, we obtain: $b_x = \left(\frac{i}{k} \right) \frac{\partial b_z}{\partial z}$. The boundary condition at the bottom is

$$b_z(z = 0) = 1, \tag{6.4}$$

which corresponds to imposing a periodic magnetic field with unit magnitude along the z-direction. Since it is insulating above the top boundary, we have

$$\mathbf{b} = \nabla \varphi, \tag{6.5}$$

where φ satisfies

$$\nabla^2 \varphi = 0. \tag{6.6}$$

The solution for the Laplace equation is

$$\varphi = A_1 \exp(-kz) \exp(ikx) + A_2 \exp(kz) \exp(ikx). \tag{6.7}$$

Here A_1 and A_2 are two constants. Since the magnetic field goes to zero at infinity, we have $A_2 = 0$ and

$$\varphi = A_1 \exp(-kz) \exp(ikx). \tag{6.8}$$

At the top boundary $(z = 1)$, the magnetic field satisfies

$$b_x = \frac{\partial \varphi}{\partial x} = ik A_1 \exp(-kz) \exp(ikx), \tag{6.9}$$

and

$$b_z = \frac{\partial \varphi}{\partial z} = -k A_1 \exp(-kz) \exp(ikx). \tag{6.10}$$

Combining equations (6.9) and (6.10) and $\nabla \cdot \mathbf{b} = 0$, we obtain the top boundary condition for b_z:

$$b_z + \frac{1}{k}\frac{\partial b_z}{\partial z} = 0, \quad \text{at} \quad z = 1. \tag{6.11}$$

The equation (6.3) with the above boundary conditions can be solved analytically by Airy functions:

$$b_z = v_1 A_i(y) + v_2 B_i(y), \tag{6.12}$$

where y is defined as: $y = -(ikR_m)^{1/3}(z - \frac{ik}{R_m})$; v_1 and v_2 are two constants determined by the boundary conditions. Figure (6.1) shows the attenuation of the x-dependent magnetic field by the specified uniform shear flow $u = z$ for different magnetic Reynolds numbers. The magnitude of the x-dependent magnetic field is attenuated more for larger R_m (i.e., smaller magnetic diffusivity).

Without considering the attenuation produced by the shear flow, the magnetic field in vacuum decays as $\sim \exp(-kz)$, which is the geometric attenuation. Define the physical attenuation factor F_a as the attenuation produced by the shear flow only:

$$F_a = \frac{b_z(z = 1)\exp(k)}{b_z(z = 0)}. \tag{6.13}$$

It is clear from equation (6.3) that the asymptotic ($kR_m \gg 1$, $k \leq 1$) solution has a real part of the form $b_z \propto \exp\left(-\frac{2}{3\sqrt{2}}\sqrt{kR_m}z^{3/2}\right)$, except for a slowly varying amplitude term. Evaluated at $z = 1$, this gives

$$F_a \approx \exp\left(-0.47\sqrt{kR_m}\right). \tag{6.14}$$

Define Ψ as the stream function for the magnetic field:

$$b_x = -\frac{\partial}{\partial z}\Psi, \tag{6.15}$$

and

$$b_z = \frac{\partial}{\partial x}\Psi. \tag{6.16}$$
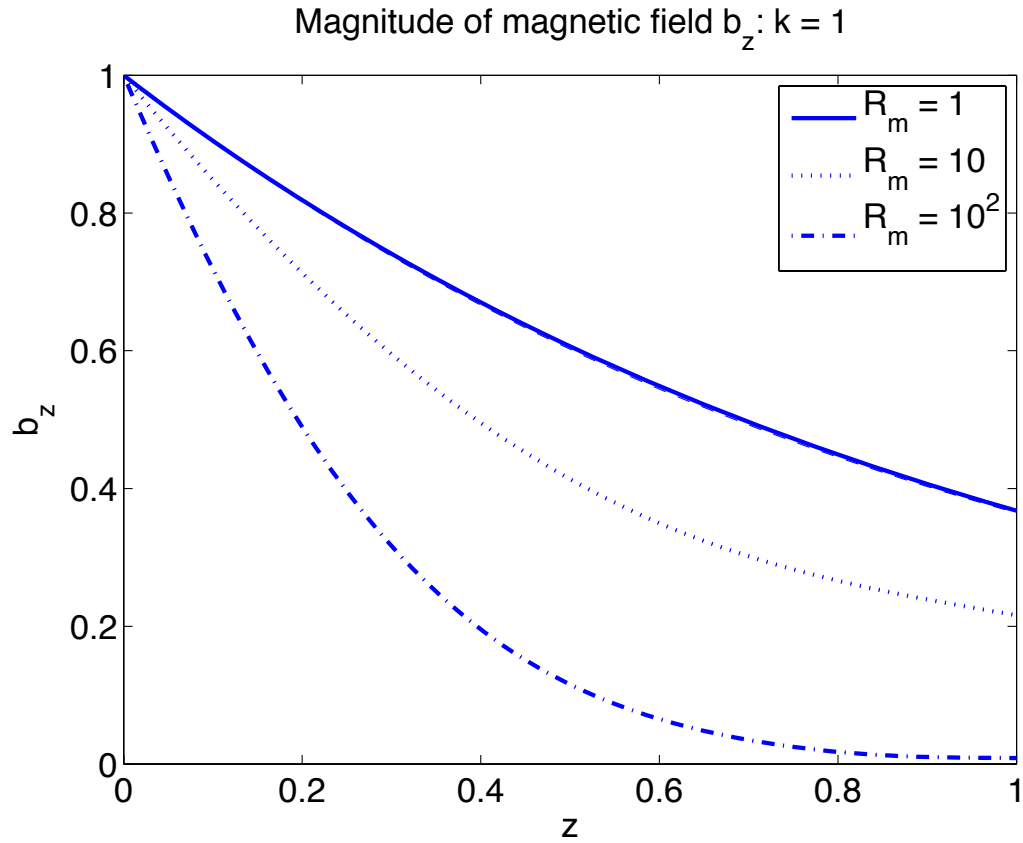
Figure 6.1 The magnitude of the x-dependent magnetic field b_z as a function of height z for different R_m. Here, the x-dependent vertical magnetic field ($b_z = \exp(ikx)$) is imposed at the bottom boundary and the horizontal wavenumber k is taken to be: $k = 1$. The attenuation effect is strong for large R_m.

Thus, $b_z = ik\Psi$ and $\Psi = b_z/ik$. We can draw the contours of Ψ as the representation of the magnetic field lines. Figure (6.2) shows the contour plot of the magnetic field lines without and with flow. Without flow, the periodically x-dependent magnetic field imposed at the bottom boundary diffuses through the electrical conducting medium. With flow, the magnetic field lines are dragged by the flow and move together with the fluid. The magnetic field lines travel a large distance in the horizontal direction before reaching the top boundary. Thus, the x-dependent magnetic field diffuses more and is attenuated.

The typical solution for the attenuation effect is characterized by the Airy function (equation (6.12)). The Airy function is related with the Bessel function of order $1/3$. To see why the fraction $1/3$ shows up in the problem, considering the following: Since the velocity shear is constant, the distance that the fluid advects the magnetic field lines during time t at coordinate z is $\delta \sim tz\frac{du}{dz}$. But in time t, the field diffuses a distance $dz \sim (t\lambda)^{1/2}$ (see figure (6.3)). Set $dz \sim z$, and eliminate t from the above two relations to obtain

$$k\delta \sim k\frac{du}{dz}\frac{z^3}{\lambda}. \tag{6.17}$$

If $k\delta > 1$, b_x reverses signs between $z = 0$ and z, which implies that the magnetic field lines coming out from the bottom boundary go back to the bottom boundary without reaching the top. Therefore the number of magnetic field lines observed on the top surface is less than that coming from the bottom and the x-dependent magnetic field is reduced.

Also, dz can be written as

$$dz^3 = \frac{\pi}{k}\frac{\lambda}{du/dz}. \tag{6.18}$$

If dz is smaller than the domain size, the field line will reverse its direction before reaching the top boundary and the x-dependent field is attenuated.
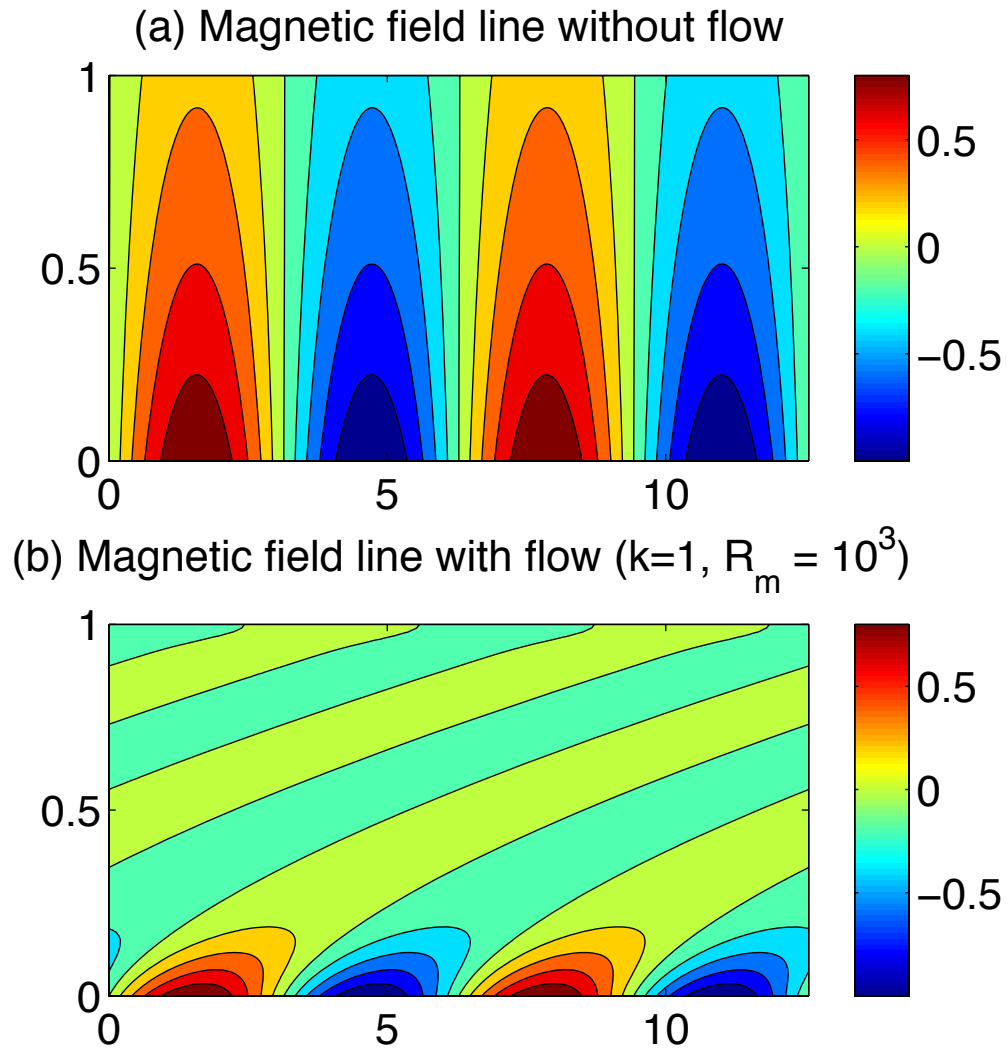
Figure 6.2 Magnetic field lines. (a) Without the flow; (b) with the flow for $k = 1$ and $R_m = 10^3$. With the flow, the magnetic field lines are dragged by the flow and move together with the fluid in the high electric conducting region.

dz

X =0

X =π/k
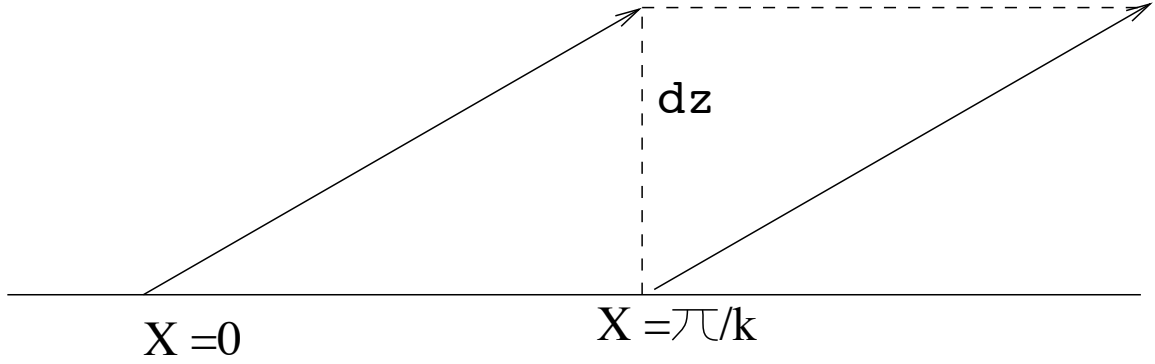
Figure 6.3 Demonstrate the mechanism of attenuating the x-dependent magnetic field by the shear flow.

6.3.2 Attenuation produced by the specified shear flow: variable magnetic diffusivity

In the steady state, the magnetic induction equation for variable magnetic diffusivity can be written as

$$\nabla \times (\mathbf{u} \times \mathbf{b}) - \nabla \times (\lambda(\nabla \times \mathbf{b})) = 0. \tag{6.19}$$

In the interior of the planet, the magnitude of the magnetic diffusivity increases exponentially outward from the high electrical conducting region. Consider the following magnetic diffusivity distribution: $\lambda = \lambda_0 \exp(\beta z)$, where $1/\beta$ is the scale height. For periodic magnetic field: $\mathbf{b} = b_0(\exp(ikx))\mathbf{e}_z$ imposed at the bottom boundary and specified the uniform shear flow along the x direction: $u = z$, the scaled magnetic induction equation can be written as

$$\exp(\beta z) \left[-k^2 b_z + \frac{d^2 b_z}{dz^2} \right] - iR_m kz b_z = 0, \tag{6.20}$$

where R_m is defined as $R_m = uL/\lambda_0$. The boundary conditions for the magnetic field are the same as in the previous section. For $R_m = 10^3$, we can calculate b_z as a function of z for different β. The results are shown in figure (6.4). The attenuation effect is concentrated at the place with small magnetic diffusivity.

Figure (6.5) shows the contours of the magnetic field lines. The magnetic field
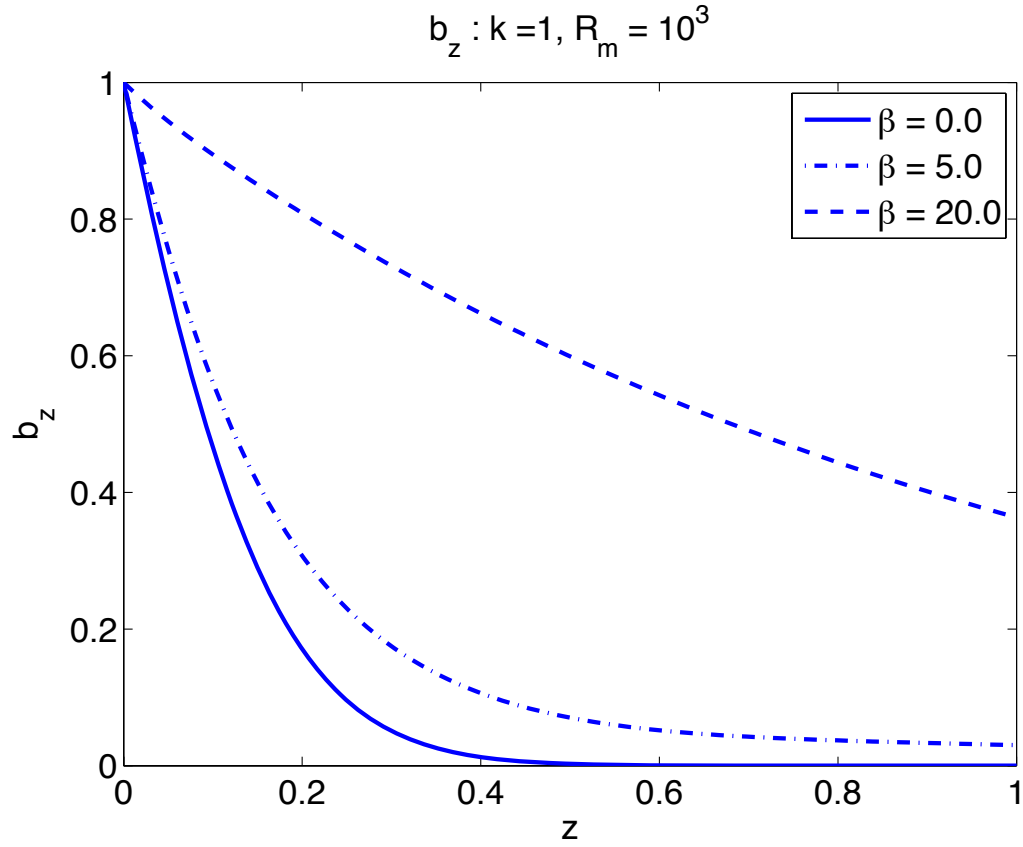
Figure 6.4 The attenuation of the x-dependent field by the specified shear flow with variable magnetic diffusivity: $\lambda = \lambda_0 \exp(\beta z)$. Here $k = 1$, $R_m = 10^3$ and β is: $\beta = 0.0$; $\beta = 5.0$; $\beta = 20.0$. The attenuation effect is concentrated in the region with low magnetic diffusivity.
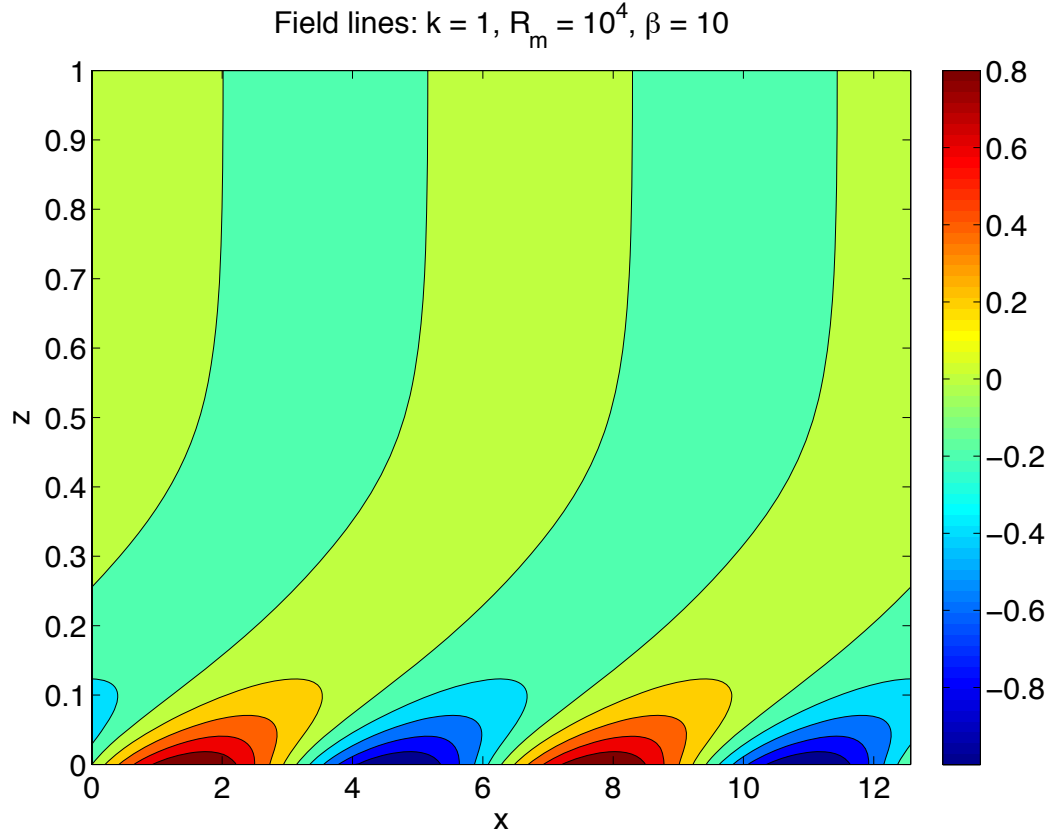
Figure 6.5 Magnetic field line advected by the fluid for variable magnetic diffusivity: $\lambda = \exp(\beta z)$. Here $R_m = 10^4$, $k = 1$ and $\beta = 10$. The magnetic field lines will only be advected by the flow in the region with low magnetic diffusivity.

lines are advected by the flow in the low magnetic diffusivity region. In the high magnetic diffusivity region, the magnetic field lines are not influenced by the flow.

6.3.3 Perturbation analysis: constant magnetic diffusivity

The observed dipole tilt is small for both Jupiter and Saturn. It is about 10° for Jupiter and less than 0.1° for Saturn (Connerney, 1993). It is reasonable to treat the non-axisymmetric magnetic field as a perturbation to the axisymmetric magnetic field. If the flow is driven along the x-direction, and the uniform magnetic field is imposed along the z-direction, the magnetic field is able to reduce the magnitude of velocity. In equilibrium, both the magnetic field and the flow are uniform in the x-direction. We then perturb the system with a periodic x-dependent magnetic fields

along the z-direction: $\mathbf{b} \propto \exp(ikx)\mathbf{e}_z$ and investigate whether the x-dependent magnetic field can be attenuated by the magnetically limited flow.

The perturbed magnetic induction equation is

$$\lambda \nabla^2 \mathbf{b} + \nabla \times (\mathbf{U} \times \mathbf{b}) = 0, \tag{6.21}$$

where $\mathbf{U}$ is the axisymmetric velocity field in equilibrium. It is determined by equation (5.8) and (5.9) if the flow is driven by boundary stress; and is determined by equation (5.18) and (5.19) if the flow is driven by body force. The equation (6.21) can be written in component form:

$$\lambda \left(\frac{\partial^2}{\partial x^2} + \frac{\partial^2}{\partial z^2} \right) b_x + \frac{\partial}{\partial z} (b_z U_x) = 0 \tag{6.22}$$

and

$$\lambda \left(\frac{\partial^2}{\partial x^2} + \frac{\partial^2}{\partial z^2} \right) b_z - \frac{\partial}{\partial x} (b_z U_x) = 0. \tag{6.23}$$

The perturbed magnetic field is divergence free: $\nabla \cdot \mathbf{b} = 0$, which implies that $b_x = \frac{i}{k} \frac{\partial b_z}{\partial z}$. Substituting this expression into equation (6.22) and (6.23) yields

$$\left(-k^2 + \frac{\partial^2}{\partial z^2} \right) b_z - ikR_m (b_z U_x) = 0, \tag{6.24}$$

where R_m is defined as $R_m = \frac{UL}{\lambda}$ and U_x is axisymmetric velocity field along the x-direction. According to the analysis in chapter 5, the magnitude of velocity is reduced by the magnetic field. The dimensionless number characterize this reduction is Q if the magnetic diffusivity is small enough. If the flow is driven by boundary stress, the magnitude of the flow reduction is proportional to the inverse square root of the Chandrasekhar number: $\Re_r \propto Q^{-1/2}$. In this case, the effect is confined to thin boundary layers and the velocity is nearly constant in the bulk of the flow. If the flow

is driven by the following body force:

$$\mathbf{F} = 12 u_0 \nu \left(z - \frac{L}{2} \right) \frac{1}{L^3} \mathbf{e}_x, \tag{6.25}$$

the magnitude of the flow reduction is proportional to the inverse of the Chandrasekhar number: $\Re_r \propto Q^{-1}$. In this case, the effect is distributed throughout the layer as a reduction in velocity shear. It is accordingly closer in form to the flow we assumed earlier in this chapter. The effective magnetic Reynolds number is

$$R_m^* = \frac{UL}{\lambda} = \frac{U_0 \Re_r L}{\lambda}, \tag{6.26}$$

where U_0 is the magnitude of the velocity at the top boundary without the magnetic field. The Chandrasekhar number is defined as $Q = \frac{B_0^2 L^2}{\mu_0 \lambda \rho \nu}$. If the flow is driven by boundary stress, the effective magnetic Reynolds number is

$$R_m^* = \left(\frac{\mu_0 \rho \nu}{\lambda} \right)^{\frac{1}{2}} \frac{U_0}{B_0}. \tag{6.27}$$

If the flow is driven by body force (6.25), the effective magnetic Reynolds number is

$$R_m^* = \frac{\mu_0 \rho \nu U_0}{B_0^2 L}. \tag{6.28}$$

It is interesting to see that the magnetic Reynolds number does not depend on the magnitude of the magnetic diffusivity λ in this case. For the above two driving situations, equation (6.24) can be solved. The results are shown in figure (6.6) for different Q.

In the outer shell of giant planets, hydrogen (the dominant constituent) is supercritical, which implies that there is no gas-liquid or gas-solid phase transition in this region. Besides the outer boundary at the planetary surface, there is no other boundary. Driving the fluid by body force in the form (6.25) does not produce viscous boundary layers and is therefore more applicable to the planetary interior. We
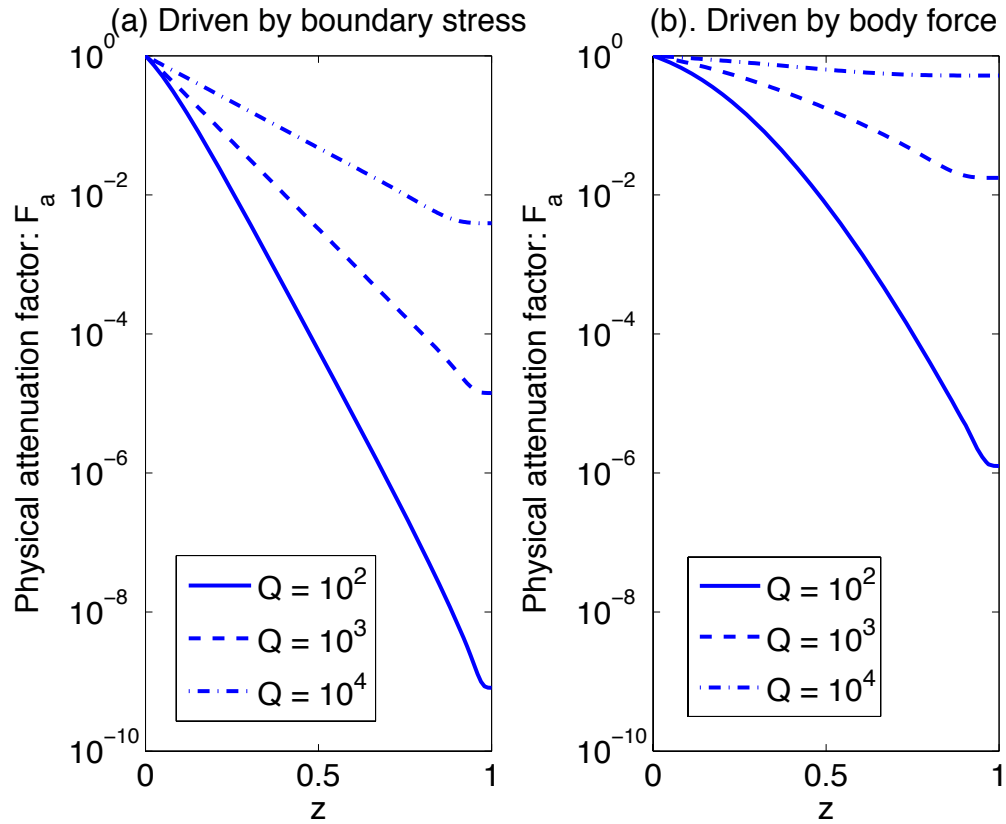
Figure 6.6 The relation between the physical attenuation factor and height for differ-ent magnetic diffusivities: (a) drive the flow by boundary stress; (b) drive the flow by variable body forces (see equation (6.25)). We take $k = 1$ and $R_m = 10^4$.

focus on this case in the following investigations. Based on equation (6.28), we can estimate the magnitude of the effective magnetic Reynolds number R_m^2 for Juptier and Saturn. For Jupiter, we take: $\rho \sim 10^3$ kg m^{-3}; $\mu \sim 10^3$ m^2 s^{-1}; $U_0 \sim 0.01$ m s^{-1}; $B_0 \sim 4.2 \times 10^{-4}$ Tesla; and $L \sim 10^6$ m. Thus, $R_m^* \sim 10^{-1}$. For Saturn, we take $\rho \sim 10^3$ kg m^{-3}; $\mu \sim 10^3$ m^2 s^{-1}; $U_0 \sim 0.2$ m s^{-1}; $B_0 \sim 0.2 \times 10^{-4}$ Tesla; and $L \sim 10^6$ m. Thus, $R_m^* \sim 30$. For Jupiter and Saturn, the difference in the effective magnetic Reynolds number is about two orders of magnitude. It seems that Saturn's non-axisymmetric magnetic field can be attenuated more.

6.3.4 Perturbation analysis: variable magnetic diffusivity

For variable magnetic diffusivity, the magnetic induction equation can be written as

$$-\nabla \times (\lambda(\nabla \times \mathbf{b})) + \nabla \times (\mathbf{U} \times \mathbf{b}) = 0. \tag{6.29}$$

Take $\lambda = \lambda_0 \exp(\beta z)$, the above equation can be rewritten in component form:

$$\exp(\beta z)\left(-k^2 + \frac{\partial^2}{\partial z^2}\right) b_z - ikR_m\left(b_z U_x\right) = 0. \tag{6.30}$$

For different driving forces, the velocity shear reduction by the magnetic field is different. In this case, the attenuation effect depends on the local magnetic Reynolds number: $R_m = UL/\lambda \exp(\beta z)$. However, for driving the flow by body force (see equation (6.25)), the magnetic Reynolds number does not depend on λ provided λ is small enough.

6.4 The thin shell approximation and the boundary conditions

In this section, we specify the zonal flow velocity in a spherical shell, and calculate the attenuation effect to the non-asymmetric magnetic field produced by this spherical

shell. The governing equation is the magnetic induction equation:

$$\frac{\partial \mathbf{B}}{\partial t} = -\nabla \times (\lambda \nabla \times \mathbf{B}) + \nabla \times (\mathbf{U} \times \mathbf{B}), \tag{6.31}$$

where the magnetic diffusivity is a function of the radius r only. If we choose the length scale to be the planetary radius: $[L] \sim R$; velocity scale to be the magnitude of the small scale velocity in the deep interior: $[U] \sim U_0 \sim 0.01$ m s^{-1}; the magnetic diffusivity scale to be the magnetic diffusivity at the metallic hydrogen region $[\lambda] \sim \lambda_0 \sim 4m^2$ s^{-1}; the magnetic field scale to be the poloidal magnetic field observed on the surface of the planet: $[B] \sim \mathbf{B}_0 \sim 10$ G; the time scale to be the diffusion time scale: $[T] \sim \frac{R^2}{\lambda}$; we can non-dimensionalize the magnetic induction equation:

$$\frac{\partial \mathbf{B}}{\partial t} = -\nabla \times (\lambda \nabla \times \mathbf{B}) + R_m \nabla \times (\mathbf{U} \times \mathbf{B}), \tag{6.32}$$

where R_m is the magnetic Reynolds number, and is defined as

$$R_m = \frac{U_0 R}{\lambda_0}. \tag{6.33}$$

In spherical coordinates (r, θ, ϕ), assume that the non-axisymmetric magnetic field is in the following form:

$$\mathbf{B} = (\mathbf{B}_r(r, \theta), \mathbf{B}_\theta(r, \theta), \mathbf{B}_\phi(r, \theta)) \exp(im\phi). \tag{6.34}$$

Here ϕ is the azimuthal wave number. Thus, the magnetic induction equation (6.32) can be written in the following component form: The $\mathbf{e}_r$ component of the magnetic induction equation is

$$+ \frac{1}{r\sin(\theta)} \left[\frac{\lambda}{r} \frac{\partial}{\partial \theta} \left(\sin(\theta) \left(\frac{\partial}{\partial r}(rB_\theta) - \frac{\partial}{\partial \theta} B_r \right) \right) - \frac{im\lambda}{r\sin(\theta)} \left(imB_r - \sin(\theta) \frac{\partial}{\partial r}(rB_\phi) \right) \right]$$
$$+ \frac{imR_m}{r\sin(\theta)}(B_r U_\phi) = 0. \tag{6.35}$$

Since the magnetic diffusivity changes rapidly with radius, the significant attenuation happens in a thin shell. Use the thin shell approximation

$$r = a + \xi, \tag{6.36}$$

where a is the inner boundary of the spherical shell. Under the thin shell approximation, $r \to a$ and $dr \to d\xi$, and the $\mathbf{e}_r$ component of the magnetic induction equation can be rewritten as

$$\frac{\lambda}{a}\frac{\partial}{\partial\theta}\left(\sin(\theta)\left(\frac{\partial}{\partial\xi}(aB_\theta) - \frac{\partial}{\partial\theta}B_r\right)\right) - \frac{im\lambda}{a\sin(\theta)}\left(imB_r - \sin(\theta)\frac{\partial}{\partial\xi}(aB_\phi)\right)$$
$$= -imR_m(B_rU_\phi). \tag{6.37}$$

The divergence-free magnetic field implies that

$$\nabla \cdot \mathbf{B} = \frac{\partial}{\partial\xi}(B_r) + \frac{1}{a\sin(\theta)}\frac{\partial}{\partial\theta}(\sin(\theta)B_\theta) + \frac{im}{a\sin(\theta)}B_\phi = 0. \tag{6.38}$$

Combining the equation (6.37) and (6.38), we then obtain

$$\frac{\partial^2}{\partial\xi^2}B_r = -\frac{1}{a^2\sin(\theta)}\frac{\partial}{\partial\theta}\left(\sin(\theta)\frac{\partial}{\partial\theta}B_r\right) + \frac{m^2}{a^2\sin^2(\theta)}B_r + \frac{im}{a\lambda\sin(\theta)}R_mB_rU_\phi. \tag{6.39}$$

In this equation, the terms $-\frac{1}{a^2\sin(\theta)}\frac{\partial}{\partial\theta}\left(\sin(\theta)\frac{\partial}{\partial\theta}B_r\right)$ and $\frac{m^2}{a^2\sin^2(\theta)}B_r$ express the second derivative of the magnetic field respect to θ and ϕ. Since the magnetic diffusivity changes rapidly along the r-direction, the variation of the magnetic field along the r-direction will be much more than the variation along the θ and the ϕ direction. So, we can ignore those two second derivative terms and simplify the above equation (6.39) as

$$\frac{\partial^2}{\partial\xi^2}B_r = \frac{im}{a\lambda\sin(\theta)}R_mB_rU_\phi. \tag{6.40}$$

If we choose L to be the dimension of the thin shell ($L << a$), we have

$$z = \frac{\xi}{L}. \tag{6.41}$$

The equation (6.40) can be rewritten as

$$\frac{\partial^2}{\partial z^2} B_r = \frac{imL^2}{a\lambda \sin(\theta)} R_m B_r U_\phi. \tag{6.42}$$

Now we consider the boundary conditions for the above equation. At the outer boundary $z = 1$, the electrical current in the radial direction is zero

$$\mathbf{J} = \mu_0 \left(\nabla \times \mathbf{B} \right)_r = 0. \tag{6.43}$$

Under the thin shell approximation, we have

$$(\nabla \times \mathbf{B})_r = \frac{1}{a\sin(\theta)} \left[\frac{\partial}{\partial\theta}(\sin(\theta)B_\phi)imB_\theta \right]. \tag{6.44}$$

Since the magnetic field is divergence free, we then have

$$\frac{\partial}{\partial\xi}B_r + \frac{1}{a\sin(\theta)}\frac{\partial}{\partial\theta}(\sin(\theta)B_\theta) + \frac{im}{a\sin(\theta)}B_\phi = 0; \tag{6.45}$$

Therefore, the magnetic field along the ϕ direction can be expressed as

$$B_\phi = \frac{a\sin(\theta)}{im}\frac{\partial B_r}{\partial\xi} + \frac{1}{im}\frac{\partial}{\partial\theta}(\sin(\theta)B_\theta). \tag{6.46}$$

Substitute this expression into the equation (6.44), we then arrive

$$m^2 B_\theta + \frac{\partial}{\partial\theta}\left(\sin(\theta)\frac{\partial}{\partial\theta}(\sin(\theta)B_\theta)\right) + \frac{\partial}{\partial\theta}\left(\sin^2(\theta)\frac{\partial}{\partial z}B_r\right) = 0 \tag{6.47}$$

Since the magnetic diffusivity varies rapidly in the r-direction, the largest term in the above equation (6.47) is the term involving $\frac{\partial}{\partial z}B_r$ and there is no other term that can

balance this term. Thus we have:

$$\frac{\partial B_r}{\partial z} = 0. \tag{6.48}$$

Consider the inner boundary condition (at $z = 0$). The observed magnetic field is the curl free potential field, which r component can be written as:

$$B_r = \sum_{n=1}^{\infty} \sum_{m=0}^{n} \left[(n+1) \left(\frac{a}{r}\right)^{n+2} \left(g_n^m \cos(m\phi) + h_n^m \sin(m\phi)\right) P_n^m(\cos(\theta)) \right], \tag{6.49}$$

where $P_n^m(\cos(\theta))$ are Schmidt quasi-normalized associated Legender functions of degree n and order m, and g_n^m, h_n^m are the internal Schmidt coefficients. For Jupiter, the tilted dipole corresponds to $n = 1$ and $m = 1$. From the O_6 model (Cornnerney, 1993), the internal Schmidt coefficients are determined as: $g_1^1 = -0.65929$ and $h_1^1 = 0.24116$. Thus the magnitude of observed B_r for $n = 1$ and $m = 1$ ranges from -1.4 G to 1.4 G depending on ϕ and θ. For Saturn, the dipole tilt is $0.1°$ or less. Based on the Z_3 model, both g_1^1 and h_1^1 are zero. Here we impose a tilted dipole field ($n = 1$ and $m = 1$) in the bottom boundary of the shell:

$$B_r = B_{11} a^{-3}(-2) P_1^1(\cos(\theta)) \exp(i\phi), \tag{6.50}$$

where B_{11} is a constant. For Jupiter, it is chosen to produce the observed dipole tilt. For Saturn, we assume that its dipole tilt is the same as that of Jupiter without the attenuation by the flow. Thus, B_{11} is chosen to produce dipole tilt about $10°$ on the surface. Figure (6.7) shows scaled non-axisymmetric magnetic field on both Jupiter and Saturn, where the non-axisymmetric magnetic field is scaled by the maximum value along the θ direction.

According to the analysis in the previous section, the magnitude of the zonal flow is reduced by the axisymmetric magnetic field and the reduction depends on

the inverse of Chandrasekhar number ($Q^{-1} \sim \frac{\mu_0 \lambda(r) \rho \nu}{B_0^2 H_\lambda^2}$) for driving flow with a body force. Here B_0 is the radial component of the axisymmetric magnetic field; ρ is the density; ν is the viscosity; and H_λ is the scale height of the magnetic diffusivity. Thus, $U \propto Q^{-1} U_{\phi 0}$, where $U_{\phi 0}$ is the velocity without being reduced by the magnetic field. For simplicity, we assume $U_{\phi 0} = U_0 \sin(\theta)$ for both Jupiter and Saturn. Therefore, the equation (6.42) can be rewritten as:

$$\frac{\partial^2}{\partial z^2} B_r = \frac{imL^2}{a\lambda \sin(\theta)} R_m Q^{-1} B_r U_{\phi 0}. \tag{6.51}$$

Similarly as in previous section, we can define an effective magnetic Reynolds number:

$$R_m^* = R_m Q^{-1} = \frac{U_0 R}{\lambda_0} \frac{\mu_0 \rho \nu \lambda_0}{B_0^2 H_{\lambda_0}^2} = \frac{U_0 R \mu_0 \rho \nu}{B_0^2 H_\lambda^2}. \tag{6.52}$$

Consider the attenuation produced in a spherical shell just outside of the metallic hydrogen region by the small scale velocity. Here is a possible application of this result. From the mixing length theory, the magnitude of viscosity is $\nu \sim U_0 L_{mix}$, where L_{mix} is the mixing length with the magnitude about ~ 100 km. Taking $\rho \sim 10^3$ kg m^{-3}, $B_0 = 4.2 \times 10^{-4}$ Tesla for Jupiter and $B_0 = 0.2 \times 10^{-4}$ for Saturn, we calculated the external magnetic field corresponding to a tilted dipole for different velocities U_0 (see figure (6.7)). For a flow with $U_0 = 10^{-3}$ m s^{-1}, the attenuation effect for Jupiter's titled dipole is negligible. However, the attenuation effect produced by the same flow makes Saturn's titled dipole 10^2 times smaller than that without the attenuation. The attenuation effect is stronger for larger U_0. Our Ohmic dissipation calculation in chapter 3 indicates that the amount of velocity has to be less than 0.2 m s^{-1} for Jupiter and 0.5 m s^{-1} for Saturn, which are much larger that the velocities we used here.

The axisymmetric magnetic field along the r direction B_0 is also a function of θ. Based on the observation external to the planet, B_0 can be treated as mainly dipole with small amount of quadrupole and octupole component. Figure (6.8) shows
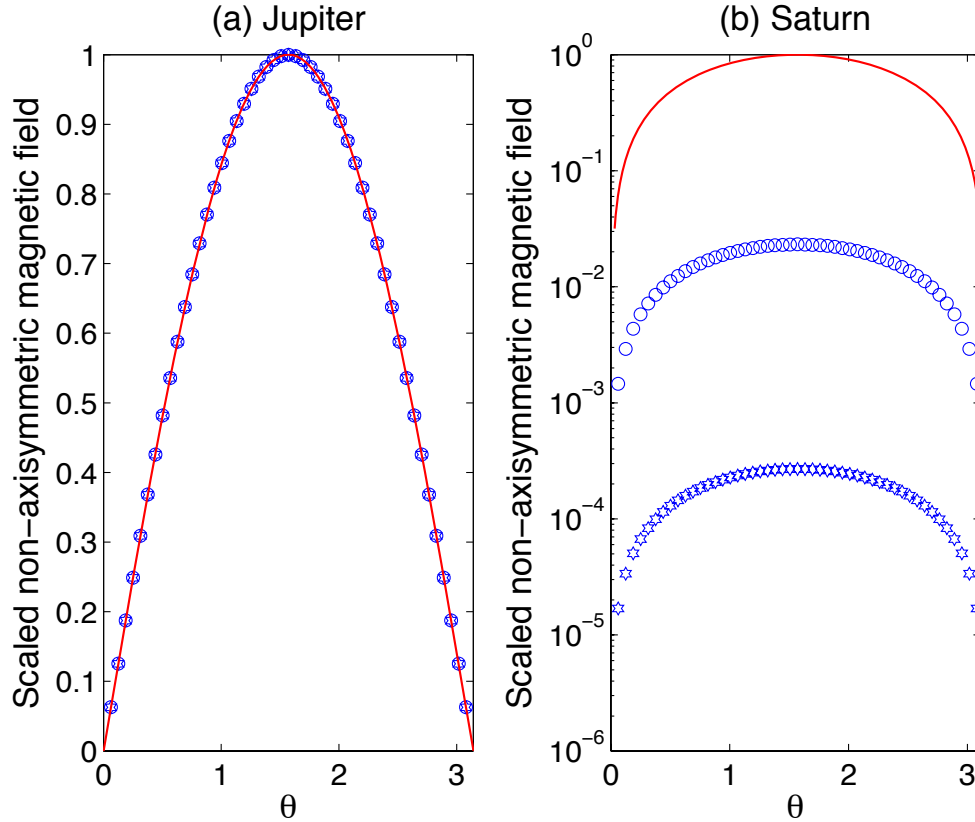
Figure 6.7 The attenuation for the tilted dipole produced by fluid motion in the deep interior. (a) Jupiter; (b) Saturn. Here we assume that Jupiter and Saturn have similar dipole tilt without being attenuated by the flow. The solid line shows the scaled non-axisymmetric magnetic field without being attenuated by the flow, where the magnetic field is scaled by the maximum value of tilted dipole along the meridional direction. The circle corresponds to the external field after being attenuated by the flow with $U_0 = 10^{-3}$ m s^{-1} and the hexagon represents $U_0 = 2 \times 10^{-3}$ m s^{-1}, where U_0 is the magnitude of the flow without being reduced by the magnetic field. The flow has negligible effect in reducing Jupiter's outgoing tilted dipole. However, $U_0 = 10^{-3}$ m s^{-1} makes Saturn's titled dipole 10^2 times smaller than that without the attenuation; and $U_0 = 2 \times 10^{-3}$ m s^{-1} makes it 10^4 times smaller.
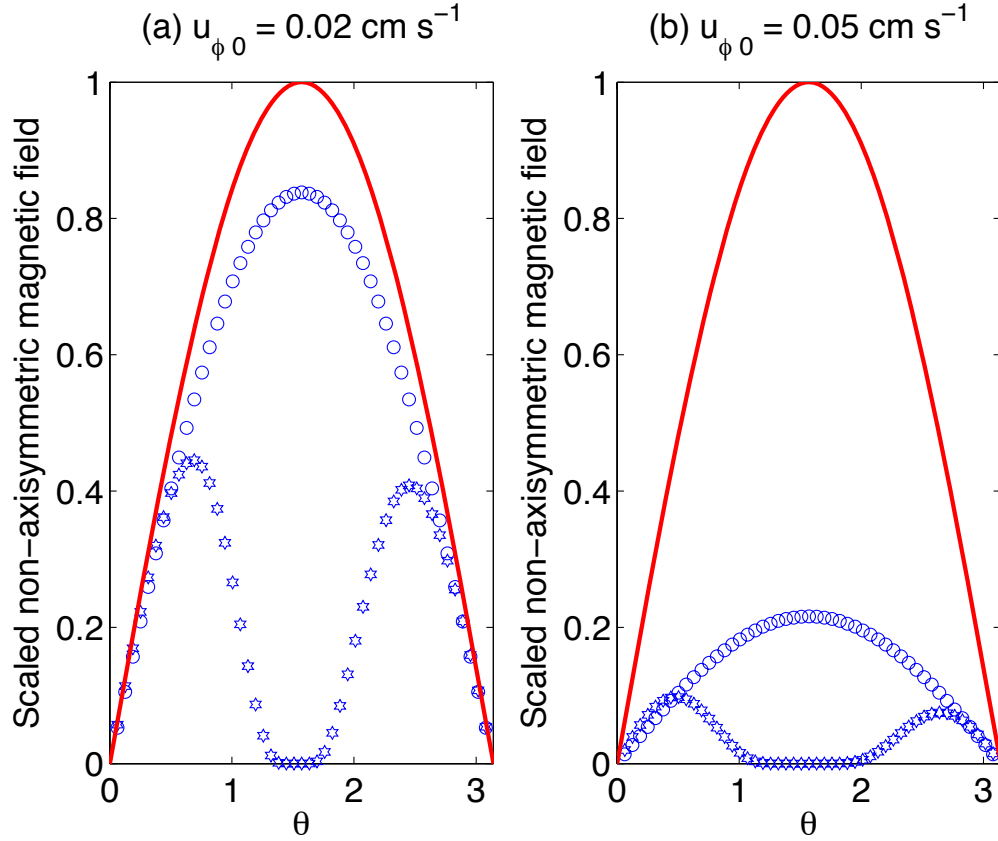
Figure 6.8 Comparison between using constant B_0 and $B_0(\theta)$ as a function of θ. (a) $U_0 = 0.02$ cm s^{-1}, (b) $U_0 = 0.05$ cm s^{-1}. The solid line corresponds to the scaled non-axisymmetric magnetic field without attenuated by the flow. The circle corresponds to external magnetic field with constant B_0 and the hexagon represents to external magnetic field with B_0 as a function of θ. $B_0(\theta)$ is taken to be the observed value.

comparison between using constant B_0 and $B_0(\theta)$ as a function of θ. It is shown that non-axisymmetric magnetic field is attenuated more near the equatorial region if $B_0(\theta)$ is used in the definition of Q. It is due to the small magnitude of the dipole field near the equatorial region.

The axisymmetric magnetic field provide no ready explanation for observation of periodic magnetospheric phenomena near the polar region, such as the rotation modulation of Saturn kilometric radio emission (Desch & Kaiser, 1981; Kaiser & Desch, 1982), optical spoke activity in Saturn's B ring (Porco & Danielson, 1982), and aurora ultraviolet intensity (Sandel et al., 1982). Since the spacecraft measurements

are confined to the low latitude $40°N$ to $40°S$ (Connerney, 1993), the magnetic field in the equatorial region might be more axisymmetric than that in the polar region, which is consistent with our theory of attenuating non-axisymmetric magnetic field by magnetically limited flow.

6.5 Conclusion and discussion.

In this chapter, we investigate the attenuation of the non-axisymmetric magnetic field by magnetically limited zonal flow. The smaller Saturnian field may allow a larger velocity shear and a greater attenuation of the non-axisymmetric field, thereby providing a possible explanation for the nearly axisymmetric field. However, the analysis is based on the velocity reduction calculated from a Cartesian geometry without considering the effect of rotation. More detailed analysis including the Coriolis force is needed.

Chapter 7 Attenuation of temporal variations of magnetic field in the outer region of Jupiter.

7.1 Abstract

The magnetic core, defined as the region of substantial electrical currents and field generation, is clearly confined in the actual core for the terrestrial planets. However, for gas giant planets the definition of the magnetic core is not at all obvious. Shock-wave experiments have measured the electrical conductivity of hydrogen at shock pressures in the range of 0.93 Mbar to 1.8 Mbar and an estimated temperature at about 3000 K, representative of the conditions inside Jupiter (Nellis et al., 1996). These measurements have shown that hydrogen undergoes a continuous transition from a semi-conducting molecular to metallic fluid, which means that giant planets do not have a clearly defined core-mantle boundary. In addition, possible strong, deeply penetrating zonal winds may interact with the magnetic field even at low electrical conductivity, at a place quite far out in the molecular envelope. We study the attenuation of the time-dependent magnetic field by the semi-conducting envelope through the well-known electromagnetic screening effect, and conduct a preliminary estimation of the influence of the flow to the magnetic field in the semi-conducting molecular hydrogen envelope. Combining the study for the attenuation effect produced by the semi-conducting layer and the observation of the magnetic field by Galileo and Voyager, we find the possible outer boundary of the dynamo generation zone is at 0.86 Jupiter radius. If the zonal flows observed on the surface penetrate to the deep interior along cylinders, dynamo generation of a magnetic field can occur at radii where the electrical conductivity is many orders of magnitude below that of

metallic hydrogen if the modest conversion of toroidal to poloidal field (for example that predicted by an α-effect with amplitude suggested by convective motions) exists. The fields generated in this region (and the magnetic Reynolds number that characterizes their generation) are dictated by a length scale comparable to the scale height of the electrical conductivity, which is much smaller than the radius of the planet.

7.2   Introduction.

Jupiter's magnetic field shows some remarkable similarities to Earth's magnetic field. Both planets have a dominant dipole field with the dipole tiles about $10°$. When the magnetic field is downward continued to the radius at which metallic conduction is likely, the field strength at degree $l = 2$ has a similar ratio to the dipole field for the two planets (~ 0.2), and there is likewise a similar ratio at $l = 3 (\sim 0.1)$. Furthermore, the data from the Galileo spacecraft (in combination with the Voyager's data) shows that Jupiter's dipole varies at a rate that is comparable or smaller than variation of Earth's magnetic field (Russell et al., 2001).

However, considering the different internal structure between Jupiter and Earth, the similarity between the magnetic fields in these two planets is surprising. The terrestrial planet Earth is composed of an iron core and a silicate mantle. The iron core is made of high electric conductivity and low viscosity fluid, and the silicate mantle is made of low electric conductivity and high viscosity fluid. Although there maybe a thin immobile layer of intermediate conductivity (Lay et al., 1998), we can view Earth as having a step function conductivity profile. The interaction between the magnetic field and the fluid motion is only important in the iron core. The outgoing magnetic field generated in the core is attenuated by the silicate mantle through the magnetic diffusion effect.

By contrast, the gas giant planet Jupiter is composed primarily of hydrogen (92% atomic) and helium (8% atomic), and the internal structure may not exhibit a step

function in material properties. Shockwave experiments have measured the electrical conductivity of hydrogen at shockwave pressure in the range of 0.93 Mbar to 1.8 Mbar and an estimated temperature at 3000 Kelvin, representative of condition inside Jupiter (Nellis et al., 1996). These experiments suggest that hydrogen undergoes a continuous transition from a semi-conducting molecular to metallic state, which implies that the conductivity profile in the interior of Jupiter is a smooth (though rapidly declining) function of radius. Second, the low conductivity region is a fluid whereas it is a solid in terrestrial planets. The low conductivity fluid can modify the magnetic field lines of the outgoing magnetic field, and the interaction between the fluid and field can change the fluid velocity as well.

As a consequence of these two striking differences, the definition of the "magnetic core" of a giant planet such as Jupiter (here defined to be the region of substantial electrical current and field generation region) is not at all obvious. In this chapter, we will examine what is meant by the magnetic core of the giant planet. We approach this problem by considering the attenuation produced by the finite conducting outer regions on the time varying internally generated fields, and by a preliminary assessment of the consequence of fluid motions on the field in these outer regions.

Irrespective of the zonal flow, the poloidal magnetic field generated in the dynamo region will diffuse through the semi-conducting molecular hydrogen layer and be attenuated by the well-known electromagnetic screening effect. In a region of uniform conductivity and thickness L, the diffusion timescale is $\tau_{diff} = \frac{L^2}{\pi^2 \lambda}$ (Moffatt, 1978). Here λ is the magnetic diffusivity: $\lambda = \frac{1}{\mu_0 \sigma}$, μ_0 is the magnetic permeability and σ is the electrical conductivity. In the region of rapidly varying conductivity, this estimation of timescale is still roughly applicable but with L interpreted as the conductivity scale height. If the conductivity at the outermost region of the dynamo generation region is high, the diffusion timescale will be longer, and vice versa. In general, dynamos generate magnetic fields that exhibit a wide range of frequencies (Roberts & Soward, 1992; Busse, 2000). However, components of the magnetic field varying on

a timescale shorter than the diffusion timescale will be attenuated. Therefore, from the observed secular variation of the magnetic field, we could get the conductivity that corresponds to the outermost boundary of the dynamo generation region. Comparing the magnetic field measurements from Galileo and Voyager, the magnitude of the dipole moment on Jupiter increased about 1.5% over the period from 1975 to 2000 (Russell et al., 2001), which suggests that there is significant power for field variations at the time scale of ~ 1000 years. If we take $L = 1000$ km, the estimated conductivity is about 10^5 S m^{-1}, which corresponds to the outermost boundary of the dynamo generation to be $0.85R_J$.

On the other hand, if the observed zonal flow in the Jovian atmosphere is the surface expression of the zonal flow on the cylindrical surface, or part of the zonal flow observed on the surface of the planet penetrates to the interior with other vertical structure, the dynamo might be able to be generated at a place far out in the envelope compared with the metallic hydrogen region.

In this chapter, we will try to give a more quantitative explanation for the magnetic core of the giant planets. In section 7.3, the internal conductivity distribution of Jupiter is estimated based on the shock wave experimental data. In section 7.4, we calculated the expected frequency dependent attenuation by semi-conducting molecular hydrogen in Jupiter. In section 7.5, given different assumptions about the size of the dynamo generation region, the expected temporal variation of the magnetic field is calculated. We combine our model with the observed secular variation to constrain the size of the dynamo generation region and the lowest dynamo generation conductivity. In section 7.6, we estimate the influence of the fluid motion to the field by the α-effect and ω-effect. In section 7.7, we examine whether the shell dynamo could be generated in the outer layer and get the corresponding critical dynamo number. We also study the influence of the large conductivity gradient to the dynamo generation. From this, we assess the possibility that dynamo action extends much farther out than previously supposed.

7.3 Comparing the electrical conductivity profiles of Jupiter and Earth

We can compare the conductivity profile of Jupiter with that of Earth. For Jupiter, the electrical conductivity profile has been obtained in Chapter 2. The electrical conductivity of Earth's core is about 10^6 S m^{-1} (Keeler & Mitchell, 1969), whereas the electrical conductivity at the lower part of Earth's mantle is very uncertain, with estimations from 1 S m^{-1} to 300 S m^{-1} (Coe et al., 1995; Shankland et al, 1993; Wood & Nell, 1991). Although there may be a thin immobile layer of intermediate conductivity (Lay et al., 1998; Manga & Jeanloz, 1996), we can view Earth as having a step function conductivity profile. The conductivity comparison between Jovian semi-conducting envelope and the lower part of Earth's mantle is shown in Figure 1. In this comparison, we take the conductivity of the lower mantle on the Earth to be 100 S m^{-1} for convenience. For Jupiter the radius ratio used here is the radius of the semi-conducting envelope over the radius of molecular-metallic transition region $(r = 0.84R_J)$. For the Earth, the radius ratio is the radius of the lower part of the mantle over the radius of the core. Figure 7.1 shows that the electrical conductivity for most of Earth's mantle is about 1000 times lower than that for the semi-conducting molecular hydrogen envelope on Jupiter. Therefore, if the secular variation of Jovian magnetic field is in the same order as the secular variation of the Earth, the Jovian dynamo generation zone must extend to larger radius than the transition zone from the semi-conducting molecular hydrogen to metallic hydrogen. This is quantified more precisely in section 7.4.

7.4 Electromagnetic screening by the semi-conducting molecular hydrogen envelope

When a magnetic field is generated in the dynamo, it typically contains temporal variations at all frequencies (Roberts & Soward, 1992; Busse, 2000). After the gen-
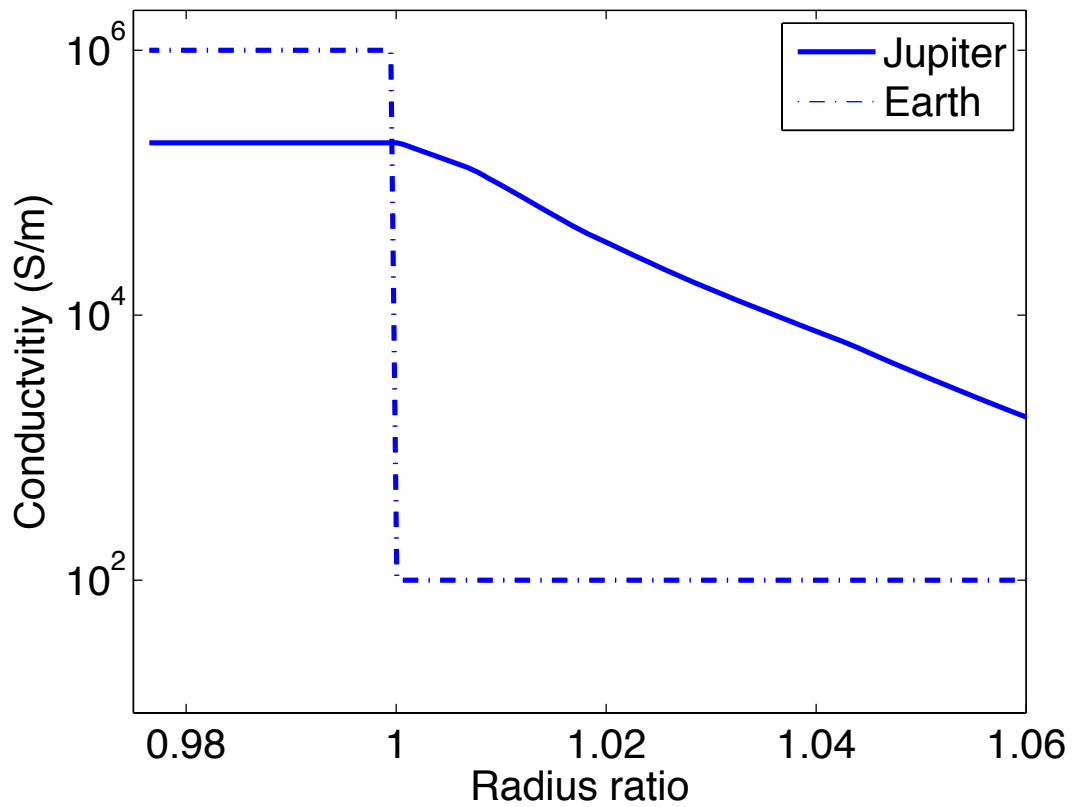
Figure 7.1 Comparison between the conductivity profile of Jupiter to that of the earth. The dash line expresses the conductivity profile of Earth, and the solid line is the conductivity profile of Jupiter.

erated magnetic field diffuses through the semi-conducting hydrogen layer outside of the dynamo generation region, high frequency temporal variations are attenuated by the electromagnetic screening effect. A layer of magnetic diffusivity λ and thickness d will produce significant field attenuation for $\omega \gg \frac{1}{\tau}$, where ω is the frequency of the magnetic field and τ is the screening timescale: $\tau = \frac{d^2}{\pi^2 \lambda}$. For variable magnetic diffusivity $\lambda = \lambda(r)$, the effective thickness is the scale height of the magnetic diffusivity $d = H_\lambda(r)$. For large d and σ, ω is smaller. It means that attenuation is strong for higher frequency. Here, we assume that the dynamo is generated in high conductivity region, and there is also a semi-conducting region outside of the high conductivity region.

In this section, we will study the attenuation effect produced by Jupiter's semi-conducting hydrogen layer in a spherical geometry. As usual, we take the limit in which the variation frequencies are much less than $\frac{c}{R_J}$ (c is the velocity of the light, and R_J is the radius of Jupiter), so that the electric displacement current can be ignored. From pre-Maxwell's equation, the electrical field $\mathbf{E}$ and the magnetic field $\mathbf{B}$ must satisfy the following equations

$$\nabla \times \left[\frac{1}{\sigma \mu_0} \nabla \times \mathbf{E} \right] + \frac{\partial \mathbf{E}}{\partial t} = 0, \tag{7.1}$$

and

$$\nabla \times \left[\frac{1}{\sigma \mu_0} \nabla \times \mathbf{B} \right] + \frac{\partial \mathbf{B}}{\partial t} = 0, \tag{7.2}$$

where μ_0 is the magnetic permeability and σ is the electric conductivity. We define a vector potential $\mathbf{A}$, so that $\mathbf{B} = \mu_0 \nabla \times \mathbf{A}$, and $\mathbf{E} = -\mu_0 \frac{\partial \mathbf{A}}{\partial t}$. The vector potential satisfies the following equation:

$$\nabla \times [\nabla \times \mathbf{A}] + \mu_0 \sigma \frac{\partial \mathbf{A}}{\partial t} = 0. \tag{7.3}$$

Due to the differences of the electrical conductivity, Jupiter could be divided into three regions: $r < R_d$, the dynamo generation region; $R_d < r < R_J$, the attenuation

region; $r > R_J$, the region external to the planet. The electrical conductivity is high in the dynamo generation region, and there is no electrical current external to the planet.

We apply equation (7.3) in the semi-conducting hydrogen layer $R_d < r < R_J$. In this region, the magnetic permeability μ_0 is that of free space and the electrical conductivity is a function of radius: $\sigma = \sigma(r)$. Under these conditions, the standard solution leading to the poloidal magnetic field (assuming $\nabla \cdot \mathbf{A} = 0$) has the following form:

$$\mathbf{A} = \nabla \times (\mathbf{e}_r \Psi), \tag{7.4}$$

and

$$\nabla^2 \Psi = \mu_0 \sigma(r) \frac{\partial \Psi}{\partial t}. \tag{7.5}$$

The toroidal field is confined in the region of finite electric current and therefore cannot be observed external to the planet. It is of little interest in studying the secular variation of the magnetic field, though it does produce a potential detectable poloidal electrical field.

For a periodic magnetic field proportional to $\exp(-i\omega t)$, where ω is the frequency of the magnetic field variation, Ψ satisfies the following equation:

$$\nabla^2 \Psi(r, \theta, \phi) = -i\mu_0 \sigma(r) \omega \Psi(r, \theta, \phi). \tag{7.6}$$

The standard solution for this equation is

$$\Psi_n(r, \theta, \phi) = R_n(r) S_n(\theta, \phi), \tag{7.7}$$

where $S_n(\theta, \phi)$ is the nth order spherical harmonics, and R_n satisfies the following equation:

$$\frac{1}{R_n(r)} \frac{d}{dr} \left(r^2 \frac{dR_n(r)}{dr} \right) - i\mu_0 \sigma(r) \omega r^2 = n(n+1). \tag{7.8}$$

The magnetic field can be expressed by the vector potential in the following way:

$$\mathbf{B} = \mu_0 \nabla \times \mathbf{A} = \mu_0 \nabla \times (\mathbf{e}_r \Psi). \tag{7.9}$$

In the semi-conducting region, we have

$$B_r = -\mu_0 n(n+1) r^{-1} R_n(r) S_n(\theta, \phi), \tag{7.10}$$

$$B_\theta = -\mu_0 r^{-1} \left[\frac{d(r R_n(r))}{dr} \right] \frac{\partial S_n(\theta, \phi)}{\partial \theta}, \tag{7.11}$$

and

$$B_\phi = -\mu_0 r^{-1} \left[\frac{d(r R_n(r))}{dr} \right] \frac{\partial S_n(\theta, \phi)}{\sin(\phi) \partial \phi}. \tag{7.12}$$

Outside of Jupiter ($r > R_J$), there is no electrical current ($\nabla \times \mathbf{B} = 0$). Thus, the magnetic field can be written as

$$B_r = -\mu_0 n(n+1) r^{-2-n} B_n S_n(\theta, \phi), \tag{7.13}$$

$$B_\theta = -\mu_0 r^{-2-n} B_n \frac{\partial S_n(\theta, \phi)}{\partial \theta}, \tag{7.14}$$

and

$$B_\phi = -\mu_0 r^{-2-n} B_n \frac{\partial S_n(\theta, \phi)}{\sin(\phi) \partial \phi}, \tag{7.15}$$

where B_n is a constant.

At the outer boundary of the dynamo generation zone ($r = R_d$), we assume that the magnetic field generated by the dynamo is in the following form:

$$B_r = S_n(\theta, \phi). \tag{7.16}$$

Since the theory is linear and separable with respect to n, we can assume unit amplitude for B_r at $r = R_d$ without loss of generality for each n. By matching the boundary condition in the three different regions: $r \leq R_g$, $R_d < r < R_J$ and $r \geq R_J$,

we solve equation (7.8) numerically with the 4th order Runge-Kutta method, we get the ratio of the magnetic field along the radial direction at the planetary surface to that at the boundary of the dynamo generation region: Λ. If Jupiter had a perfect insulator external to the dynamo, this ratio would be:

$$\Lambda = \frac{B_r|_{r=R_J}}{B_r|_{r=R_d}} = \left(\frac{R_J}{R_d}\right)^{-n-2} \tag{7.17}$$

This is called geometric attenuation, and is due to the different radii of the planetary surface and the field generation region. The geometric attenuation is a natural property of the electromagnetic field in a vacuum or perfect insulator. The magnitude of the magnetic field is smaller as the distance from the field generation region is larger. We can remove the geometric attenuation from Λ and get the physical attenuation factor F for the semi-conducting molecular hydrogen layer:

$$F(\omega) = \frac{B_r|_{r=R_J}}{B_r|_{r=R_d}} \left(\frac{R_J}{R_d}\right)^{n+2}. \tag{7.18}$$

If we take the outer boundary of the dynamo generation region to be the transition place to the metallic hydrogen region, $r = 0.84 R_J$, for periodic magnetic field with period $p \sim 5 \times 10^4$ years, there is only 5% attenuation in the amplitude, but 50% retardation in phase (see figure 7.2). The electromagnetic screening effect produced by the semi-conducting hydrogen envelope has stronger influence in phase than in amplitude. Figure 7.2 also shows that the absolute value of the attenuation factor is approximately 1 for the low frequency magnetic field and becomes much less than 1 as the frequency of the magnetic field increases, which means that the semi-conducting molecular layer has almost no effect for the low frequency magnetic field variation and strongly attenuates the high frequency magnetic field variation.

Since the electrical conductivity of hydrogen decreases exponentially from the metallic conducting region with scale height ~ 1000 km, the outer boundary of the semi-conducting hydrogen layer only has negligible effect on the attenuation produced
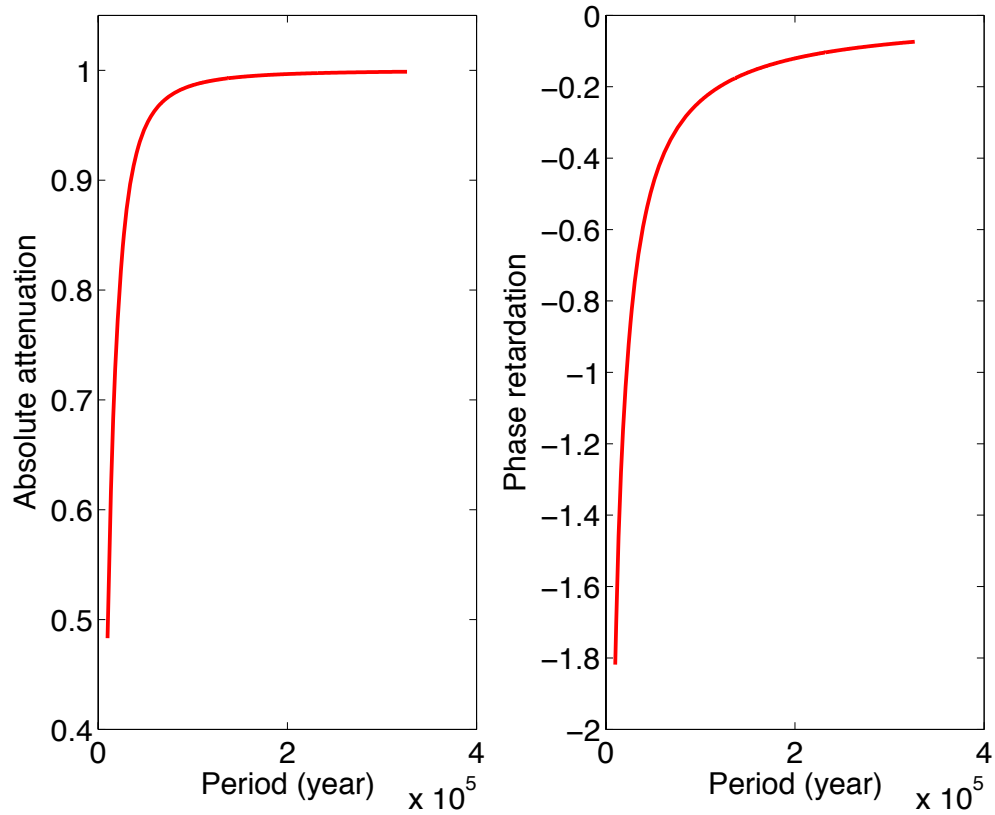
Figure 7.2 The attenuation effect produced by the semi-conducting layer. The outer boundary of the dynamo generation region is taken to be $0.84R_J$, which corresponds to the electrical conductivity 2×10^5 S m^{-1}. (a) The absolute value of the attenuation factor; (b) the phase shift of the attenuation factor.

by the layer, as long as the thickness of the semi-conducting layer is larger than several scale heights of the electrical conductivity.

Furthermore, the attenuation effect produced by the semi-conducting layer is different for different assumptions for the radius of the dynamo generation zonal R_d. The shallower the dynamo generation zone, the smaller the attenuation effect.

7.5 Secular variation and the deduction of the dynamo generation size on Jupiter

Comparing the magnetic field measurement from the Galileo spacecraft with that from Voyager, the magnitude of the dipole moment of Jupiter has increased about 1.5% over the period from 1975 to 2000 (Russell et al., 2001), which is similar to the temporal changes of Earth's magnetic field. If we let the percentage of the magnetic field variation in 25 years be V, then we have

$$V = 25 \times 3 \times 10^7 \times \sqrt{\frac{\left\langle \left(\frac{\partial \mathbf{B}_{ext}}{\partial t}\right)^2 \right\rangle}{\langle \mathbf{B}_{ext}^2 \rangle}}, \tag{7.19}$$

where $\mathbf{B}_{ext}$ is the magnetic field external to the surface. In terms of the frequency ω for the magnetic field, we have:

$$\frac{\left\langle \left(\frac{\partial \mathbf{B}_{ext}}{\partial t}\right)^2 \right\rangle}{\langle \mathbf{B}_{ext}^2 \rangle} = \frac{\frac{1}{2\pi} \int_{-\infty}^{+\infty} \omega^2 F^*(\omega) F(\omega) \widetilde{B}_d^*(\omega) \widetilde{B}_d(\omega) d\omega}{\frac{1}{2\pi} \int_{-\infty}^{+\infty} F^*(\omega) F(\omega) \widetilde{B}_d^*(\omega) \widetilde{B}_d(\omega) d\omega}, \tag{7.20}$$

where $\widetilde{B}_d(\omega)$ is the Fourier spectrum of the magnetic field at the outer boundary of dynamo generation region (For Earth, it is the core-mantle boundary), $\widetilde{B}_d^*(\omega)$ is the conjugate of $\widetilde{B}_d(\omega)$, and $F(\omega)$ is the physical attenuation factor. The power-spectrum of the magnetic field at the boundary of dynamo generation region is

$$S_d(\omega) = \widetilde{B}_d^*(\omega) \widetilde{B}_d(\omega). \tag{7.21}$$

Power-spectral analysis of the intensity of Earth's magnetic field inferred from ocean sedimental core and archaeo-magnetic data from timescale of 100 yr to 10 Myr shows that the power spectrum on Earth's surface is proportional to $1/\omega$ (Pelletier, 1999). Since the conductivity of Earth's mantle is low, the significant physical attenuation for the internally generated signal is for the scale of 4 to 40 years (Currie, 1968). For the signal with a timescale larger than 100 years, the attenuation effect by the mantle layer is negligible. Therefore, the power-spectrum at the core-mantle boundary for Earth can be inferred to be proportional to $1/\omega$. Assuming Jupiter's dynamo is similar to the geo-dynamo, the power-spectrum at the boundary of the dynamo generation region will likewise be proportional to $1/\omega$:

$$S_d(\omega) = \widetilde{B}_d^*(\omega)\widetilde{B}_d(\omega) \propto \frac{1}{\omega}. \tag{7.22}$$

Therefore, we can take numerical integration for different size of the dynamo generation zone. The results are shown in figure 7.3. From this figure, we find that in order to match the observed secular variation, the size of the dynamo generation region is about $0.86R_J$. The conductivity at this radius is about 2×10^4 S m^{-1}, which is 10 times smaller than the measured conductivity of the metallic hydrogen.

7.6 Attenuation of the magnetic field in the presence of the dynamo effect

In the semi-conducting layer, the turbulent flow of the electrically conducting fluid and the shear of the zonal wind will interact with the outgoing magnetic field from the dynamo generation zone. The correct description of this problem is the coupled Navier-Stokes equation with the magnetic induction equation. The complete solution of this problem is beyond the scope of this chapter. Here, we specify the flow and analyze the influence of the flow to the magnetic field. We consider this by making use of a very simple model in which the turbulent flow of the electrical conducting fluid
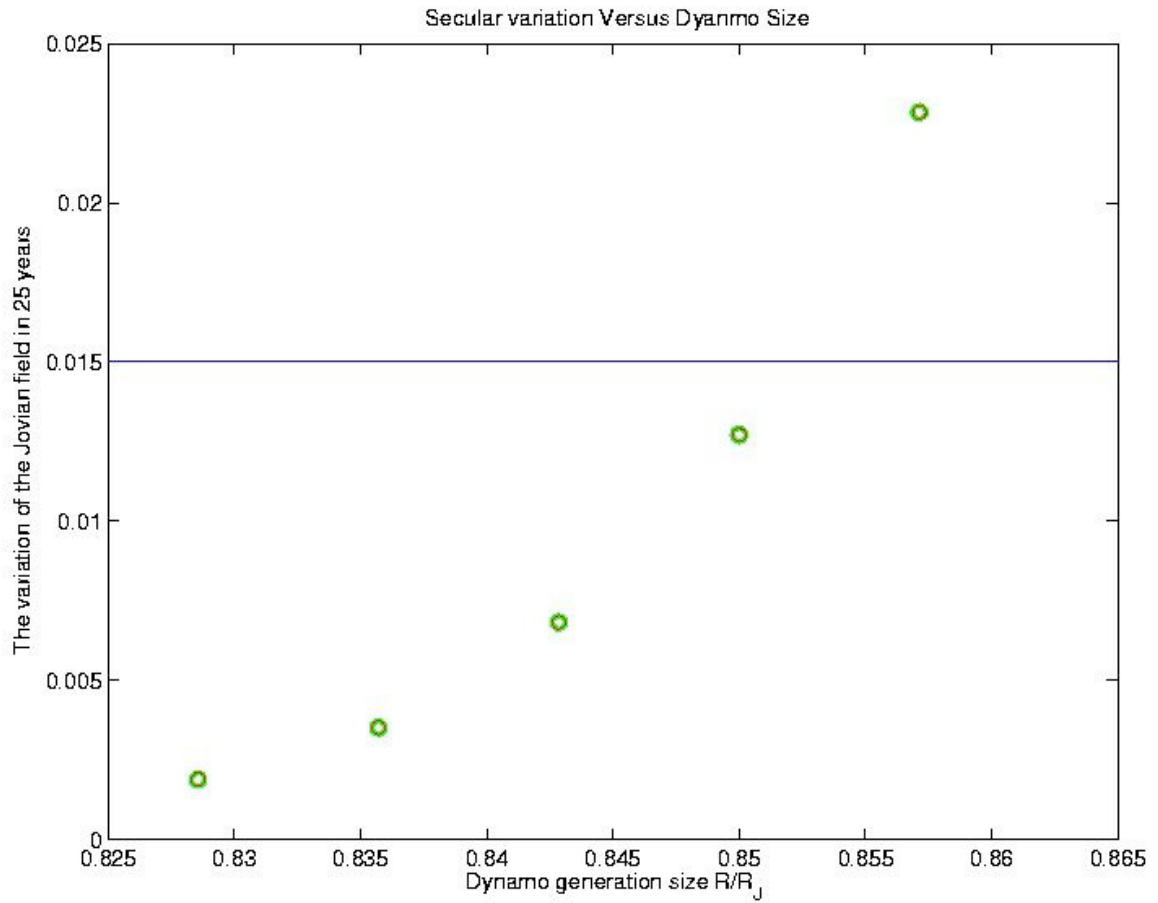
Figure 7.3 The calculated magnetic field versus the different dynamo size.

generates the poloidal field from the toroidal field by means of the α-effect (Moffatt, 1978), and the vertical shear of the zonal winds produce the toroidal magnetic field from the poloidal field through the ω-effect. In this section, we assume that there is a source of dynamo generation in the deep interiors of the giant planets and analyze the changes of the magnetic field produced by the semi-conducting layer outside of the dynamo generation region in the presence of α and ω effects. The electrical conductivity drops exponentially outwards from the dynamo generation region in this semi-conducting layer with scale height about $1/b \sim 1000 \, \text{km}$, which is much less than the radius of the Jupiter: $bR_J \gg 1$. Therefore, we can use the thin shell assumption. Under this assumption, Cartesian coordinates are adequate.

Let z be along the vertical direction, x be along the north-south (latitudinal) direction, and y be along the east-west (zonal) direction. Using these Coordinates, the magnetic field $\mathbf{B}$ can be written as the summation of the toroidal magnetic field $\mathbf{B}_T$ and the poloidal magnetic field $\mathbf{B}_P$:

$$\mathbf{B} = \mathbf{B}_T + \mathbf{B}_P, \tag{7.23}$$

while

$$\mathbf{B}_P = \nabla \times (A\mathbf{e}_y), \tag{7.24}$$

and

$$\mathbf{B}_T = B\mathbf{e}_y, \tag{7.25}$$

where A and B are two scalars. Here we assume that the magnetic field is azimuthally symmetric, so A and B are the functions of x, z, t only. For the rapidly rotating planet, the magnitude of the zonal flow is generally much larger than the flow in the vertical and meridional direction. Thus, we only consider the influence due to the zonal flow. Assume the gradient of the zonal flow to be γ, A and B satisfy the following equations:

$$\frac{\partial A}{\partial t} = \lambda(z)\nabla^2 A + \alpha B, \tag{7.26}$$

and

$$\frac{\partial B}{\partial t} = \frac{\partial}{\partial z}\left(\lambda(z)\frac{\partial B}{\partial z}\right) + \lambda(z)\frac{\partial^2 B}{\partial x^2} - ik\gamma A. \tag{7.27}$$

These equations admit the local solution: $A = A(z)\exp(pt+ikx)$ and $B = B(z)\exp(pt+ikx)$, where k is the latitudinal wave number. If $Re(p)$ is smaller than zero, the solution decays with time, and the magnetic field cannot be generated. If $Re(p)$ is larger than zero, the solutions for A and B grow with time, the magnetic field can be generated by means of α and ω effect. If $Re(p) = 0$, the solution is migrating magnetic waves.

7.6.1   No α-effect and no ω-effect

Consider first the simplest case: the modification of the magnetic field generated in the dynamo region simply comes from the electromagnetic screening effect. In this case, we do not consider the influence of the flow. Under the thin shell assumption, the analysis in the Cartesian geometry is almost the same as the previous analysis in the spherical geometry. In this section, we get a simpler expression for the attenuation effect produced by the semi-conducting hydrogen layer in Cartesian geometry.

In this case, the magnetic induction equation can be simplified as

$$\frac{\partial A}{\partial t} = \lambda(z)\nabla^2 A. \tag{7.28}$$

Let the outer margin of the dynamo generation region be $z = 0$. Since the electrical conductivity drops exponentially from the dynamo generation region with scale height $1/b$, the magnetic diffusivity can be written as $\lambda(z) = \lambda_0\exp(bz)$, where λ_0 is the magnetic diffusivity at the outer boundary of the dynamo generation region. The equation (7.28) has the local solution $A = A(z)\exp(pt + ikx)$. Change the variable from z to ζ: $\zeta = 2\sqrt{\frac{p}{\lambda_0 b}}\exp\left(-\frac{bz}{2}\right)$. $A(\zeta)$ satisfies the following equation:

$$p\left[\frac{d^2 a}{d\zeta^2} + \frac{1}{\zeta}\frac{dA}{d\zeta} - \left(1 + \frac{4}{\beta^2\zeta^2}\right)A\right] = 0, \tag{7.29}$$

where β is defined as $\beta = b/k$. The latitudinal wavelength for the dipole magnetic field is about $1/k = R_J/2$. Under the thin shell approximation, we have $\beta \gg 1$. The solution for this equation is $\ell_{2/\beta}(\zeta)$(Abramowitz and Stegun, 1995), where $\ell_{2/\beta}(\zeta)$ is the first or second kind of the modified Bessel function: $I_{2/\beta}(\zeta)$ or $K_{2/\beta}(\zeta)$. Choosing $\Re(\sqrt{p}) > 0$, we obtain that $\zeta \to 0$ ($z \to +\infty$) corresponds to the place outside of the planet, and $\zeta = 2\sqrt{\frac{p}{\lambda b}}$ ($z = 0$) represents the outer margin of the dynamo generation region. Without considering the influence due to α-effect and ω-effect, the magnetic field decays outside of the dynamo generation region. The solution for equation (23) is

$$A(\zeta) = A_0 I_{2/\beta}(\zeta). \tag{7.30}$$

Since the electrical conductivity is an exponential function of z, the asymptotic limit is already reached for a few bz, it is not necessary to impose a separate boundary condition at the planet surface or to account for the spherical geometry. The physical attenuation factor F_a can be written as

$$F_a = \frac{\lim_{z \to \infty} \exp(kz) I_{1/\beta}(\zeta)}{I_{2/\beta}\left(2\sqrt{\frac{p}{\lambda_0 b^2}}\right)} = \frac{\left(\sqrt{\frac{p}{\lambda_0 b^2}}\right)^{2k/b}}{I_{2/\beta}\left(2\sqrt{\frac{p}{\lambda_0 b^2}}\right)}. \tag{7.31}$$

Here, the geometric attenuation factor $\exp(-kz)$ has been removed. Let $p = i\omega$, where ω is the frequency of the magnetic field and is a real number. For small p (low frequency), the attenuation factor F can be simplified to

$$F_a = \frac{1}{1 + \frac{p}{\lambda_0 b^2}} = \frac{1 - \frac{i\omega}{\lambda_0 b^2}}{1 + \left(\frac{\omega}{\lambda_0 b^2}\right)^2}. \tag{7.32}$$

Clearly, $\omega \sim \lambda_0 b^2$ defines the frequency at which the significant attenuation is starting to occur. The semi-conducting layer can significantly modifying the phase of the outgoing field even without significantly modify the amplitude of the field. For example, at $\omega \sim 0.1\lambda_0 b^2$, there is only a 1% reduction in field amplitude, but a 10% shift in phase. For very low frequency $\omega \to 0$, the attenuation factor approaches 1, which means that there is no attenuation effect at low frequency. The semi-conducting hy-

drogen layer behaves as a low pass filter.

For the large p, the attenuation factor can be simplified as

$$F = \sqrt{4\pi} \left(\frac{p}{\lambda_0 b^2} \right)^{1/4} \exp \left(-2\sqrt{\frac{p}{\lambda_0 b^2}} \right). \tag{7.33}$$

For the high frequency variation, the attenuation factor is an exponential function of p. The semi-conducting hydrogen layer significantly reduces the high frequency component of the magnetic field through the electromagnetic screening effect.

7.6.2 Finite α-effect and no ω-effect: no time dependence

Here we consider the influence of the turbulent flow in the semi-conducting layer to the outgoing magnetic field. The turbulent flow can interact with the toroidal magnetic field and produce poloidal magnet field through α-effect (Moffatt, 1978). For the interior of Jupiter, the turbulent flow can come from convection with the typical magnitude 1 cm s^{-1} (Guillot et al., 2004). In this section, we assume there is no shear acting on the zonal winds and ignore the influence of the ω-effect. In steady state, the magnetic induction equation can be written as:

$$\lambda(z)\nabla^2 A + \alpha B = 0 \tag{7.34}$$

and

$$\frac{\partial}{\partial z} \left(\lambda(z) \frac{\partial B}{\partial z} \right) - \lambda(z) k^2 B = 0. \tag{7.35}$$

Here A and B admit the following local solutions: $A = \exp(pt + ikx)A(z)$ and $B = \exp(pt + ikx)B(z)$. Change of variables from z to ζ: $\zeta = \exp\left(-\frac{1}{2}bz \right)$, $B(\zeta)$ satisfies the following equation:

$$\frac{d^2 B}{d\zeta^2} - \frac{1}{\zeta}\frac{dB}{d\zeta} - \left(\frac{2k}{b} \right)^2 \frac{B}{\zeta^2} = 0, \tag{7.36}$$

and $A(\zeta)$ satisfies

$$\frac{d^2 A}{d\zeta^2} + \frac{1}{\zeta}\frac{dA}{d\zeta} - \left(\frac{2k}{b}\right)^2 \frac{A}{\zeta^2} + \frac{4\alpha B}{\lambda_0 b^2} = 0. \tag{7.37}$$

The particular solution for equation (7.36) is $B = B_0\zeta^2$, where B_0 is a constant. Substituting this particular solution into equation (30) yields $A = A_0\zeta^{2k/b} + A_1\zeta^4$. Here A_0 is a constant and $A_1 = -\frac{\alpha B_0}{4\lambda_0 b^2}$. Analogous to the attenuation factor, we define a "reduction factor" F_R, where F_R is the ratio of the radial field outside of planet ($z \to +\infty$) to the radial field at the outer boundary of the dynamo generation region ($z = 0$) after removing the geometric attenuation effect. In this case, the reduction factor is

$$F_R = \frac{1}{1 - \frac{\alpha B_0}{4\lambda_0 b^2 A_0}}. \tag{7.38}$$

Define q to be the ratio of the actual toroidal field to the radial field (poloidal field) at the outer boundary of the dynamo generation region:

$$q = \frac{B_0}{ik\left[A_0 - \frac{\alpha B_0}{4\lambda_0 b^2}\right]}. \tag{7.39}$$

The reduction factor F_R can be written as a function of q:

$$F_R = \frac{1 + \frac{ik\alpha}{4\lambda_0 b^2}}{1 - \frac{ik\alpha}{4\lambda_0 b^2}(1 - q)}. \tag{7.40}$$

If we assume that the magnetic field generated by the dynamo is isotropic at the outer margin of the dynamo generation region, i.e., the magnitude of the toroidal field is the same as the magnitude of the poloidal field, we have $q = 1$ and the reduction factor F_R can be simplified as

$$F_R = 1 + \frac{ik\alpha}{4\lambda_0 b^2}. \tag{7.41}$$

For the dipole field, the latitudinal wave number of the magnetic field is: $k \sim \frac{2}{R_J} \sim 3 \times 10^{-8}$ m^{-1}. Choosing the scale height of the magnetic diffusivity to be $1/b \sim 1000$ km; the magnitude of the α-effect to be 0.01 m s^{-1}; the outer margin of

the dynamo generation region to be: $\sim 0.87 R_J$, which corresponds to the electrical conductivity $\sigma_0 = 5 \times 10^3$ S m^{-1}, we obtain $\frac{k\alpha}{4\lambda_0 b^2} \sim 2$. It means that the α-effect significantly increases the magnitude of the outgoing poloidal magnetic field even in the low conductivity region. If the electrical conductivity at the outer boundary of the dynamo generation region is higher (λ_0 is lower) or the scale height ($1/b$) is larger, the induced poloidal magnetic field produced by the α-effect is larger.

7.6.3 Finite α-effect and no ω-effect: with time dependence.

In this section, we consider the modification of the time-dependent magnetic field by the α-effect. The time-dependent outgoing magnetic field from the dynamo region is enhanced by the poloidal field generation through the α-effect, and is reduced by the electromagnetic screen effect produced in the semi-conducting layer at the same time. The magnetic field observed on the surface of the planet is the combination of these two effects. In this case, the magnetic induction equation can be written as

$$\frac{\partial A}{\partial t} = \lambda(z)\frac{\partial^2 A}{\partial z^2} - \lambda(z)k^2 A + \alpha B, \tag{7.42}$$

and

$$\frac{\partial B}{\partial t} = \frac{\partial}{\partial z}\left(\lambda(z)\frac{\partial B}{\partial z}\right) - \lambda(z)k^2 B. \tag{7.43}$$

Do variable transformation from z to ζ: $\zeta = 2\sqrt{\frac{p}{\lambda_0 b^2}}\exp\left(-\frac{bz}{2}\right)$, the equation for B can be rewritten as

$$\frac{d^2 B}{d\zeta^2} - \frac{1}{\zeta}\frac{dB}{d\zeta} - \left(\zeta^2 + \frac{4k^2}{b^2}\right)\frac{B}{\zeta^2} = 0. \tag{7.44}$$

For the thin shell approximation ($b \gg k$), the term $\frac{4k^2}{b^2}\frac{B}{\zeta^2}$ can be neglected. Then, the equation (36) has the following solution (Abramowitz & Stegun, 1970):

$$B = B_0 \zeta I_1(\zeta), \tag{7.45}$$

where B_0 is a constant. Substitute this solution into the equation of A, and do the

same variable transformation. Thus,

$$\frac{d^2 A}{d\zeta^2} + \frac{1}{\zeta}\frac{dA}{d\zeta} - \left(\zeta^2 + \frac{4k^2}{b^2}\right)\frac{A}{\zeta^2} + \frac{\alpha B_0 \zeta I_1(\zeta)}{p} = 0. \tag{7.46}$$

The solution for this equation is: $A = A_0 I_{2k/b}(\zeta) + \frac{\alpha B_0}{2p}\left(\zeta I_1(\zeta) - \frac{1}{2}\zeta^2 I_0(\zeta)\right)$. In this case, the "reduction factor" F_R can be written as

$$F_R = \frac{\lim_{z\to\infty} A_0 \exp(kz) I_{2/\beta}(\zeta)}{A_0 I_{2/\beta}\left(2\sqrt{\frac{p}{\lambda_0 b^2}}\right) + \frac{\alpha B_0}{2p}\left(\zeta_0 I_1(\zeta_0) - \frac{1}{2}\zeta_0^2 I_0(\zeta_0)\right)}, \tag{7.47}$$

where ζ_0 is the value of ζ at $z = 0$: $\zeta_0 = 2\sqrt{\frac{p}{\lambda_0 b^2}}$. Let F to be the physical attenuation factor produced by the magnetic diffusion in the semi-conducting hydrogen layer without the α-effect

$$F = \frac{\lim_{z\to\infty} \exp(kz) I_{2/\beta}(\zeta)}{I_{2/\beta}\left(2\sqrt{\frac{p}{\lambda_0 b^2}}\right)} = \frac{\left(\sqrt{\frac{p}{\lambda_0 b^2}}\right)^{2k/b}}{I_{2/\beta}\left(2\sqrt{\frac{p}{\lambda_0 b^2}}\right)}. \tag{7.48}$$

As before, define q to be the radio of the actual toroidal field to the actual radial field at the outer boundary of the dynamo generation region ($z = 0$).

$$q = \frac{B_0 \zeta_0 I_1(\zeta_0)}{ik\left[A_0 I_{2/\beta}\left(2\sqrt{\frac{p}{\lambda_0 b^2}}\right) + \frac{\alpha B_0}{2p}\left(\zeta_0 I_1(\zeta_0) - \frac{1}{2}\zeta_0^2 I_0(\zeta_0)\right)\right]}. \tag{7.49}$$

Substituting F and q into the definition of the reduction factor F_R, we have that the reduction factor F_R can be simplified as

$$F_R = \frac{F\left[1 - \frac{ik\alpha f}{2p}\right]}{1 - \frac{ik\alpha f}{2p}(1 - q)}, \tag{7.50}$$

where f is defined as

$$f = \frac{\zeta_0 I_1(\zeta_0) - \frac{1}{2}\zeta_0^2 I_0(\zeta_0)}{\zeta_0 I_1 \zeta_0}. \tag{7.51}$$

In the low frequency limit ($|p| \to 0$), F_R can be approximated to

$$F_R = \frac{F\left[1 + \frac{ik\alpha}{4\lambda_0 b^2}\right]}{1 + \frac{ik\alpha}{4\lambda_0 b^2}(1 - q)}. \tag{7.52}$$

Since $F \to 1$ as $|p| \to 0$ (there is no physical attenuation for the steady state field), the reduction factor F_R in the low frequency limit will reduce to the exact same result as that for the steady state solution. As before, we let the real part of p equal zero and analyze the outer boundary of the dynamo generation region. We express p as $p = i\omega$. As the frequency of the field ω increases, the screening effect by the semi-conducting layer increases, which decreases the value of the reduction factor F_R. For the high frequency field ($\omega \to +\infty$), the magnitude of F_R approaches zero. Evidently, $\omega \sim \lambda_0 b^2$ is the important frequency for the transition from low frequency to high frequency behavior. If we take the conductivity of the outer boundary of the dynamo generation zone to be the same conductivity as the conductivity of metallic hydrogen $\sigma_0 = 2 \times 10^5$ S m^{-1}, and take the effective thickness of the semi-conducting layer to be 1000 km, we can plot out the absolute value of the reduction factor versus the period of the magnetic field for $\alpha = 0.01$ m s^{-1} and $\alpha = 0.0$ m s^{-1} (see figure 7.4). Figure 7.4 shows that the reduction factors keep being constant at the low frequency for both α values, and decay as the frequency of the field increases. However, the constants are different for both cases. Without α-effect, the constant is 1; for the typical value of α in the interior of Jupiter ($\alpha = 0.01$ m s^{-1}), the constant is about 60. It means that the α-effect makes the poloidal magnetic field 60 times stronger than the pre-existing field if the dynamo generation boundary is chosen to be the transition zone from the metallic hydrogen to molecular hydrogen.

7.6.4   No α-effect and finite ω-effect: no time dependence.

On the surface of Jupiter, the speed of the observed zonal wind is about 100 m s^{-1}(Ingersoll, 1990). The descending of the probe in Galileo spacecraft supports the idea that the zonal wind in Jupiter penetrates to the deep interior along the cylindrical surface.
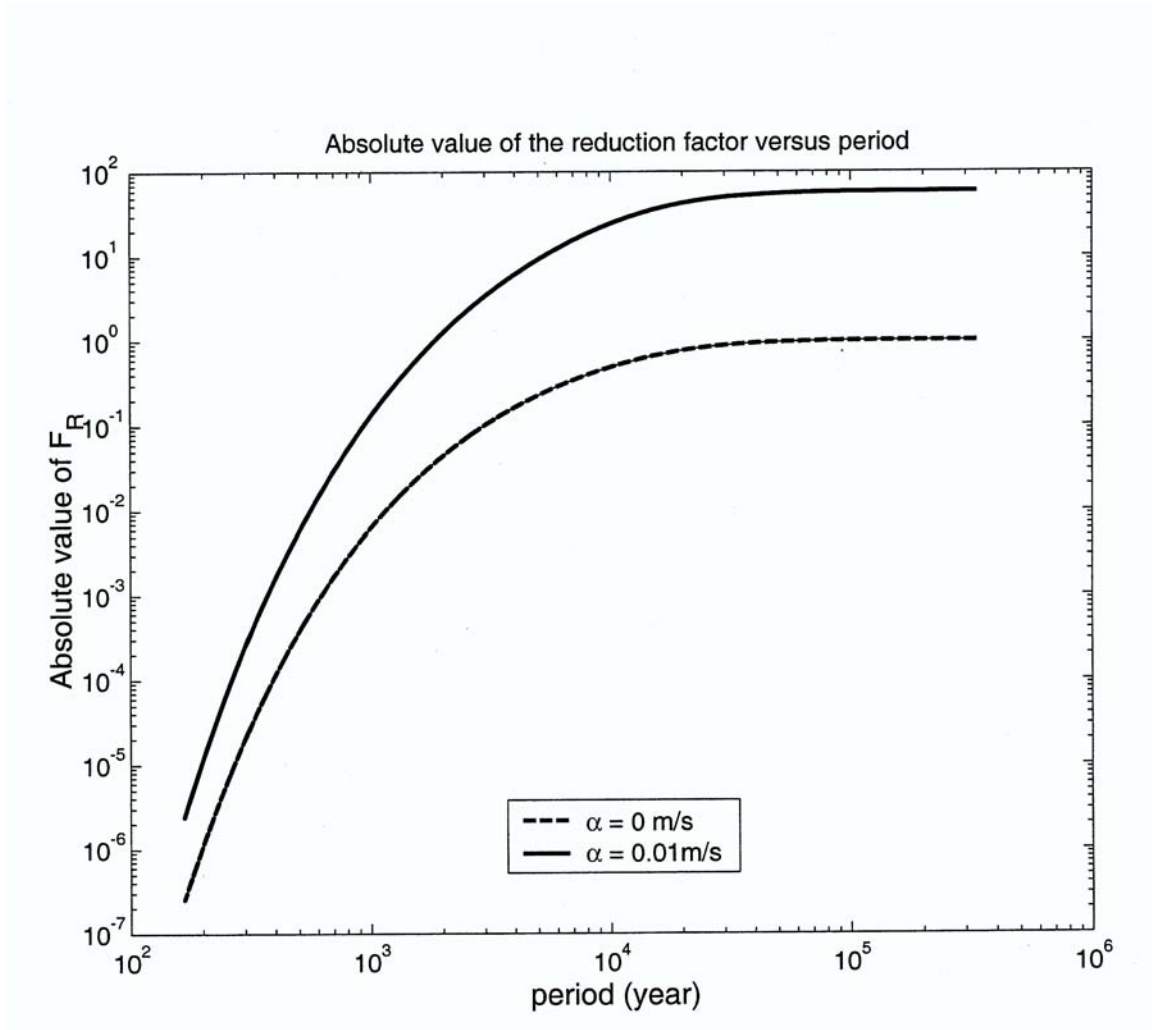
Figure 7.4 The absolute value of the reduction factor versus the period of the magnetic field for the different assumption of the magnitude of the α-effect.

In the deep interior of the planet, the electrical conductivity of material is high and the magnetic field line is fixed in the fluid. The relative velocity between the fluid and the magnetic field is small. Comparing the measurement from the Voyager spacecraft with that from the Galileo spacecraft, the dipole tilt is found to increase 0.3° over 25 period, which infers an upper bound for the relative velocity between the magnetic field and the flow in the deep interior of Jupiter to be about 0.1 cm s^{-1} (Guillot et al., 2004). Therefore these deep penetrating zonal winds have to be truncated in the interior of Jupiter. But, the position of the truncation zone is not clear. One hypothesis is that the zonal wind is truncated by Jupiter's magnetic core (Busse, 1983; Ingersoll & Pollard, 1982). In this case the magnetic field is assumed to be generated in the metallic core region. However, since the definition of the metallic core is not clear at all, this hypothesis could not give us a clear transition zone. The second hypothesis is: the zonal winds are truncated in the solid core of Jupiter (Stevenson, 1982). The third hypothesis is that the penetrating zonal flow is truncated in the weather layer.

In this section, we assume the vertical shear γ is uniformly distributed in the layer. The upper bound of the shear is taken to be: $\gamma = b\Delta u$, where $1/b$ is the effective thickness of the semi-conducting layer, and Δu is the difference between the zonal wind velocity on the surface of the planet u_s to the zonal wind velocity in the truncation zone. Since the velocity in the truncation zone is approximately zero, we obtain $\Delta u = u_s$. The lower bound of the vertical shear can be approximated as $\gamma = \frac{\Delta u}{R_J}$, where R_J is the radius of Jupiter.

Unlike the α-effect, the ω-effect produces a toroidal field from the vertical shear of the zonal winds. The toroidal field is not observable on the surface of the planet, but is of interest for understanding the total strength of the field. Here, we consider only the modification of the outgoing field by ω-effect. In steady state, the magnetic

induction equation can be written as

$$\lambda(z)\Delta^2 A = 0, \tag{7.53}$$

$$\frac{\partial}{\partial z}\left(\lambda(z)\frac{\partial B}{\partial z}\right) - \lambda(z)k^2 B - ik\gamma A = 0. \tag{7.54}$$

These equations have the local solutions in Cartesian geometry: $A = \exp(ikx)A(z)$, $B = \exp(ikx)B(z)$. For the equation of A, the solution is $A = A_0 \exp(-kz)$, where A_0 is a constant. We define $\zeta = \exp\left(-\frac{1}{2}bz\right)$, so the solution for A can be rewritten as $A = A_0\left(\zeta\right)^{2k/b}$. Substituting the solution of A to the equation of B, we have

$$\frac{d^2 B}{d\zeta^2} - \frac{1}{\zeta}\frac{dB}{d\zeta} - \left(\frac{2k}{b}\right)^2 \frac{B}{\zeta^2} = \frac{4ik\gamma A}{\lambda_0 b^2}. \tag{7.55}$$

We construct a particular solution that does not change the bottom boundary condition of B, i.e., a solution that has no current that goes to (or from) $z \to -\infty$, so we choose: $B = B_0\zeta^2 + B_1\zeta^{2+\frac{2k}{b}} - B_1\zeta^2$, where B_1 is a constant: $B_1 = \frac{2i\gamma A_0}{\lambda_0 b}$. In the regime $bz \leq 1$, the induced toroidal field is significant:

$$B_1\zeta^{2+\frac{2k}{b}} - B_1\zeta^2 \approx -\frac{i\gamma k A_0}{\lambda - 0b^2}bz\exp(-bz). \tag{7.56}$$

Therefore, the amplitude of the induced toroidal field at a typical location z is $\left|-\frac{ik\gamma A_0}{\lambda b^2}bz\exp(-bz)\right|$. Since the amplitude of the pre-existing poloidal field at location z is $|-ikA_0\exp(-kz)|$, the ratio of the induced toroidal field to the pre-existing poloidal field is

$$\Lambda = \left|\frac{\gamma}{\lambda_0 b^2}bz\exp(-bz + kz)\right|. \tag{7.57}$$

Under the thin shell approximation, we have $b \gg k$. Furthermore, since $bz\exp(-bz)$ is an order of unity at $bz \sim \frac{1}{2}$, Λ could be approximated as $\Lambda \sim \frac{\gamma}{\lambda_0 b^2}$. We can estimate the outer boundary of the dynamo generation zone at which the induced toroidal magnetic field is on the same order of magnitude as the pre-existing poloidal field: $\Lambda \sim 1$. At this radius, the magnetic diffusivity is $\lambda_0 = \frac{\gamma}{b^2}$. We choose the effective thickness of the semi-conducting layer to be $1/b \sim 1000$ km; and the meridional

wave number to be $k = \frac{2}{R_J} \sim 3 \times 10^{-8}$ m^{-1}. The upper bound of the vertical shear is $\gamma = b\Delta u = 5 \times 10^{-5}$ s^{-1}; the lower bound of the vertical shear is $\gamma = \frac{\Delta u}{R_J} = 1.4 \times 10^{-6}$ s^{-1}. Taking the upper bound of the vertical shear, we get $\lambda_0 \sim 10^{10}$ m^2 s^{-1}, which corresponds to an electrical conductivity $\sigma_0 \sim 10^{-4}$ S m^{-1}, which is nine orders of magnitude lower than the conductivity of metallic hydrogen and is around $0.95R_J$. Similarly, if we take the lower bound of the vertical shear, we have $\lambda_0 \sim 10^9$ m^2 s^{-1}, which corresponds to an electrical conductivity $\sigma_0 \sim 10^{-3}$ S m^{-1} and is around $0.94R_J$ in Jupiter. Therefore, the place at which the induced toroidal magnetic field is in the same order as the pre-existing poloidal field is around $0.94R_J \sim 0.95R_J$ and quite near the surface. If the outer boundary of the dynamo generation zone is choosing to be at $0.90R_J$, the induced toroidal field is $10^5 \sim 10^6$ G for the penetrating zonal flow. A field with such a large magnitude is not stable due to the magnetic pressure produced by the field.

7.6.5 No α-effect and finite ω-effect: with time dependence

In this section, we consider the modification of the outgoing time-dependent field by the ω-effect. The outgoing time-dependent magnetic field is enhanced by the ω-effect and reduced by the electro-magnetic screening effect at the same time. In this case, the magnetic induction equation can be written as

$$\lambda(z)\nabla^2 A = \frac{\partial A}{\partial t}, \tag{7.58}$$

and

$$\frac{\partial}{\partial z}\left(\lambda(z)\frac{\partial B}{\partial z}\right) - \lambda(z)k^2 B - ik\gamma A = \frac{\partial B}{\partial t}. \tag{7.59}$$

As before, we change the variable from z to ζ: $\zeta = 2\sqrt{\frac{p}{\lambda_0 b^2}} \exp\left(-\frac{bz}{2}\right)$. The solution for A is $A = A_0 I_{\frac{2k}{b}}(\zeta)$ and the homogenous solution for B is $B = B_0\zeta I_1(\zeta)$ (Abramowitz & Stegun, 1970). Here we neglect the second order term. The particular solution for B is $B_1\zeta I_{1+\frac{2k}{b}}(\zeta)$, where $B_1 = \frac{2i\gamma A_0}{\lambda_0 b}\zeta_0 I_{1+\frac{2k}{b}}(\zeta_0)$. We construct a particular solution that has no electrical current flow out of the inner boundary of the dynamo generation

region $z \to -\infty$. Then, the solution of the equation B is

$$B = B_0 \zeta I_1(\zeta) + B_1 \left(\zeta I_{1+\frac{2k}{b}}(\zeta) - \zeta I_1(\zeta) \right). \tag{7.60}$$

Since $k \ll b$, $I_{1+\frac{2k}{b}}(\zeta)$ can be approximated as: $I_{1+\frac{2k}{b}} \approx I_1(\zeta)(1 - kz)$. Thus the ratio of the induced toroidal field to the poloidal field Λ is

$$\Lambda \sim \left| \frac{B_1 \left(\zeta I_{1+\frac{2k}{b}}(\zeta) - \zeta I_1(\zeta) \right)}{A_0 I_{\frac{2k}{b}}(\zeta)} \right| \sim \left| -\frac{i\gamma}{\lambda_0 b^2} bz \frac{\zeta I_1(\zeta)}{\zeta_0 I_0(\zeta_0)} \right|, \tag{7.61}$$

for $|\zeta| \le 1$, i.e., $|p| \le \lambda_0 b^2$, we have $\zeta I_1(\zeta) \sim \frac{\zeta^2}{2}$. The results are approaching the steady state solution. At large $\frac{|p|}{\lambda_0 b^2}$, the value of $\frac{\zeta I_1(\zeta)}{\zeta_0 I_0(\zeta_0)}$ decreases rapidly as the distance from the outer boundary of the dynamo generation region increases, so the toroidal field is accordingly smaller. If we choose the period of the magnetic field to be 10^4 years and the outer boundary of the dynamo generation zone to be $0.90 R_J$, the induced toroidal field is $100 \sim 1000$ times larger than the pre-existing poloidal field.

7.6.6 Finite α-effect and finite ω-effect: no time dependence.

In this section, we consider the influence of the finite α-effect and the finite ω-effect to the outgoing magnetic field in the steady state. In this case, the equations for $A(z)$ and $B(z)$ are

$$\frac{d^2 A}{d\zeta^2} - \frac{1}{\zeta} \frac{dA}{d\zeta} - \left(\frac{2k}{b} \right)^2 \frac{A}{\zeta} = -\frac{4\alpha B}{\lambda_0 b^2}, \tag{7.62}$$

and

$$\frac{d^2 B}{d\zeta^2} - \frac{1}{\zeta} \frac{dB}{d\zeta} - \left(\frac{2k}{b} \right)^2 \frac{B}{\zeta} = -\frac{4ik\gamma A}{\lambda_0 b^2}, \tag{7.63}$$

where the variable ζ has the following relation with the variable z: $\zeta = 2\sqrt{\frac{p}{\lambda_0 b^2}} \exp\left(-\frac{bz}{2} \right)$. For an α-ω dynamo, it is impossible to have a dynamo in the steady state ($R_e(p) = 0$ and $I_m(p) = 0$) (Moffatt, 1978), so there is no particular solution that satisfies the above coupled equations. Here, we calculate how a particular field is modified by suc-

cessive actions, i.e., start with the homogenous solution for the field equation (51): $A_0\zeta^{\frac{2k}{b}}$, which will induce the toroidal field: $B \sim B_1\zeta^2$ through ω-effect, then the induced toroidal field will produce the following poloidal field $A \sim A_2\zeta^4$ through the α-effect, and so on.

So as before, from $A_0\zeta^{\frac{2k}{b}}$, we get the induced B field to be $\frac{2ib\gamma}{\lambda b^2}\left(\zeta^{2+\frac{2k}{b}} - \zeta^2\right)$. Inserting this into the equation for A, the induced poloidal field can be written as $A_1\zeta^{4+\frac{2k}{b}} - A_1\zeta^4$, where A_1 is a constant $A_1 \approx \frac{1}{16}\left(-\frac{4\alpha}{\lambda_0 b^2}\right)\left(\frac{2ib\gamma A_0}{\lambda_0 b^2}\right)$, so that the ratio of the induced poloidal field to the pre-existing poloidal field is

$$\frac{A_1}{A_0} \sim \frac{k}{b}\left(\frac{\alpha}{\lambda_0 b^2}\right)\left(\frac{\gamma}{\lambda_0 b^2}\right), \tag{7.64}$$

where k/b is the typical magnitude of $\zeta^{4+\frac{2k}{b}} - \zeta^4$ relative to ζ^4 in the region $bz \leq 1$; $\frac{\alpha}{\lambda_0 b^2}$ is the magnetic Reynolds number based on α-effect; $\frac{\gamma}{\lambda_0 b^2}$ is the magnetic Reynolds number based on ω-effect. For $\alpha = 1$ cm s^{-1} and the meridional wave number $k = 3 \times 10^{-8}$ m^{-1}, the ratio of the induced poloidal field to the pre-existing poloidal field can be as large as 10^6 even at the place far out of the semi-conducting envelop $(0.94R_J)$, the larger ratio is due to the generation of the magnetic field by the α-effect and the ω-effect.

7.6.7 Finite α-effect and finite ω-effect: with time dependence

In this section, we consider the modification of the outgoing time-dependent magnetic field by finite α-effect and finite ω-effect. The time dependent magnetic field will also be attenuated by the electromagnetic screening effect produced by the semi-conducting hydrogen layer. Similar to the previous sections, we analyze the modification of the field by the successive actions, i.e., from the homogenous solution of the A field equation $A_0 I_{\frac{2k}{b}}(\zeta)$, where the variable ζ is defined as: $\zeta = 2\sqrt{\frac{p}{\lambda_0 b^2}}\exp\left(-\frac{bz}{2}\right)$. The induced toroidal magnetic field is: $\frac{2ib\gamma A_0}{\lambda_0 b^2}\left(\zeta I_{1+\frac{2k}{b}}(\zeta) - \zeta I_1(\zeta)\right)$, which in turn

produces the following poloidal magnetic field:

$$A_1 = -\frac{1}{2}\left(-\frac{4\alpha}{\lambda_0 b^2}\right)\left(-\frac{2ib\gamma A_0\alpha}{\lambda_0 b^2}\right)\left[\left(\eta I_{1+\frac{2k}{b}}(\zeta) - \frac{1}{2}\zeta^2 I_{\frac{2k}{b}}(\zeta)\right) - \left(\zeta I_1(\zeta) - \frac{1}{2}\zeta^2 I_0(\zeta)\right)\right].$$

(7.65)

Choose $\lambda_0 \sim 10^4$ m^2 s^{-1} (it is four orders of magnitude higher than that of metallic hydrogen) and assume $\frac{\gamma}{k} \sim 100$ m s^{-1}, the induced toroidal field B is accordingly about 1000 times larger than the pre-existing poloidal field: $\frac{B_1}{A_0 k} \sim 1000$. Then the ratio between the induced poloidal field versus the induced toroidal field is

$$\frac{A_1 k}{B_1} \sim \frac{\alpha k}{\lambda_0 b^2} \sim \frac{0.01 \times 3 \times 10^{-9}}{10^4(5 \times 10^{-7})^2} \sim 10^2,$$

(7.66)

so that $\frac{A_1}{A_0} \sim \frac{A_1 k}{B_1}\frac{B_1}{A_0 k} \sim 10$. Therefore, the induced field is much larger than the previous field and the induced poloidal field is much less than the induced toroidal field.

7.7 α-ω dynamo generation in large electrical conductivity variation region: Cartesian geometry

The calculation in last chapter indicates the possibility that dynamo generation might occur at the region with primarily low but highly variable conductivity. Accordingly, we assess the possible solution of simple α-ω dynamo in this region.

Consider a simple dynamo generation model: a uniform α-effect and a shear concentrated at $z = 0$, where $z \to -\infty$ expresses the region inside the dynamo generation region, and $z \to +\infty$ represents the region outside the planet. Also, we assume that there is no pre-existing magnetic field. The boundary conditions at $z = 0$

are:

$$\begin{aligned}
[A]_{z=0} &= 0, \\
\left[\frac{\partial A}{\partial z}\right]_{z=0} &= 0, \\
[B]_{z=0} &= 0, \\
\left[\lambda(z)\frac{\partial B}{\partial z}\right]_{z=0} &= -ik\gamma A|_{z=0}.
\end{aligned} \tag{7.67}$$

Similar to before, we assume the fields have the local solution: $A = A(z)\exp(pt+ikx)$ and $B = B(z)\exp(pt+ikx)$. The equations for the fields A and B could be reduced to

$$pA = \lambda(z)\frac{d^2 A}{dz^2} - \lambda(z)k^2 A + \alpha B, \tag{7.68}$$

and

$$pB = \frac{d}{dz}\left(\lambda(z)\frac{dB}{dz}\right) - \lambda(z)k^2 B. \tag{7.69}$$

For $R_e(p) > 0$, the magnitude of A,B grow exponentially with time and the magnetic field is generated by the dynamo. For $R_e(p) < 0$, the magnitude of the magnetic field A, B will decay with time, and the magnetic field cannot be generated by the dynamo. Then, $R_e(p) = 0$ is the critical condition for the dynamo generation.

For the constant conductivity case, the solution for B is $B(z) \propto \exp(mz)$ for $z < 0$, and $B(z) \propto \exp(-mz)$ for $z > 0$, and m satisfies the following equation:

$$\lambda m^2 = p + \lambda k^2. \tag{7.70}$$

The boundary condition at $z = 0$ implies that

$$\frac{\gamma}{\lambda_0 k^2}\frac{\alpha}{\lambda_0 k^2} = -4i\left(\frac{m}{k}\right)^3, \tag{7.71}$$

where $\frac{\gamma}{\lambda_0 k^2}$ is the magnetic Reynolds number based on ω-effect, and $\frac{\alpha}{\lambda_0 k^2}$ is the magnetic Reynolds number based on α-effect. Since $\gamma\alpha > 0$ in the interior of Jupiter, we

need $-4i \left(\frac{m}{k}\right)^3$ to be real. Therefore the value of m satisfies: $m = Ck \exp\left(\frac{i\pi}{6}\right)$, where C is a real constant. Since m also satisfies: $\lambda m^2 = p + \lambda k^2$, we have:

$$\lambda C^2 k^2 \left(\frac{1}{2} + \frac{i\sqrt{3}}{2}\right) = p + \lambda k^2, \tag{7.72}$$

so that $C = \sqrt{2}$, $p = i\sqrt{3}\lambda k^2$ and $\frac{\gamma}{\lambda_0 k^2} \frac{\alpha}{\lambda_0 k^2} = 8\sqrt{2}$, which completely determines the critical condition for the dynamo generation, i.e., the condition at which $R_e(p) = 0$. The magnetic Reynolds number is determined by the magnitude of the α-effect and the magnitude of the ω-effect (γ). The critical dynamo number is $8\sqrt{2}$ in this case.

For the variable conductivity dependence: $\lambda = \lambda_0 \exp(bz)$, where $b > 0$. We could assume the effective thickness of the semi-conducting layer $(1/b)$ is much less than the wavelength $(1/k)$ of the magnetic field: $b \gg |k|$. Similar to before, we let $\zeta = 2\sqrt{\frac{p}{\lambda_0 b}} \exp\left(-\frac{bz}{2}\right)$ and change the variable in the equation from z to ζ. The homogenous equation for B has the solution

$$B = \frac{\zeta K_1(\zeta)}{\zeta_0 K_1(\zeta_0)} \quad \text{if} \ \ z < 0, \tag{7.73}$$

and

$$B = \frac{\zeta I_1(\zeta)}{\zeta_0 I_1(\zeta_0)} \quad \text{if} \ \ z > 0, \tag{7.74}$$

Here ζ_0 is the value of ζ at $z = 0$: $\zeta_0 = 2\sqrt{\frac{p}{\lambda_0 b^2}}$. Note that $B \propto \exp\left(2\sqrt{\frac{p}{\lambda_0 b^2}} \exp\left(-\frac{bz}{2}\right)\right)$ as $z \to -\infty$. This is very fast decay. Physically, it comes from the screening effect of the high conductivity in this region ($z \to -\infty$). For the region $z \to +\infty$, the magnitude of the field is $B \propto \exp(-bz)$ as expected for the region outside of the dynamo generation region.

The solution for A can be written as a sum of the homogenous solution A_h plus the particular solution A_p: $A(\zeta) = A_h(\zeta) + A_p(\zeta)$. The homogenous solution is

$$A_h(\zeta) = A_{h-} K_{\frac{2k}{b}}(\zeta) \quad \text{if} \ \ z < 0, \tag{7.75}$$

and

$$A_h(\zeta) = A_{h^+} K_{\frac{2k}{b}}(\zeta) \quad \text{if} \quad z > 0, \tag{7.76}$$

where A_{h^-} and A_{h^+} are two constants. The particular solution is

$$A_p(\zeta) = \frac{\alpha}{2p} \frac{\zeta K_1(\zeta) + \frac{1}{2}\zeta^2 K_0(\zeta)}{\zeta_0 K_1(\zeta_0)} \quad \text{if} \quad z < 0, \tag{7.77}$$

and

$$A_p(\zeta) = \frac{\alpha}{2p} \frac{\zeta I_1(\zeta) + \frac{1}{2}\zeta^2 I_0(\zeta)}{\zeta_0 I_1(\zeta_0)} \quad \text{if} \quad z > 0. \tag{7.78}$$

Since both A and the derivative of A are continuous at ζ_0, we have

$$A_{h^+} I_{\frac{2k}{b}}(\zeta_0) - A_{h^-} I_{\frac{2k}{b}}(\zeta_0) = \frac{\zeta_0 \alpha}{4p} \left(\frac{K_0(\zeta_0)}{K_1(\zeta_0)} + \frac{I_0(\zeta_0)}{I_1(\zeta_0)} \right), \tag{7.79}$$

and

$$A_{h^+} I_{\frac{2k}{b}}(\zeta_0) = A_{h^-} I_{\frac{2k}{b}}(\zeta_0). \tag{7.80}$$

If we assume that the effective thickness of the semi-conducting layer is much smaller than the wavelength of the dipolar magnetic field, then we have $b \ll |k|$. Let the value of A at ζ_0 is A_0, which can be approximated as

$$A_0 = \frac{\alpha}{2p}. \tag{7.81}$$

From the boundary condition of B at $z = 0$, we have

$$-\frac{\lambda_0 b \zeta_0}{2} \left(\frac{K_0(\zeta_0)}{K_1(\zeta_0)} + \frac{I_0(\zeta_0)}{I_1(\zeta_0)} \right) = -\frac{\alpha}{2p} ik\gamma. \tag{7.82}$$

Suppose there exists a solution in which $|\zeta| \ll 1$, then we can do some approximation for the Bessel functions:

$$I_0(\zeta_0) \sim 1, \tag{7.83}$$

$$I_1(\zeta_0) \sim \frac{\zeta_0}{2}, \tag{7.84}$$

$$K_0(\zeta_0) \sim -\ln(\zeta), \tag{7.85}$$

$$K_1(\zeta_0) \sim \frac{1}{\zeta}. \tag{7.86}$$

Therefore, the left hand side of the equation (68) equals to $-\lambda_0 b$ and the equation can be simplified as

$$-\lambda_0 b = -\frac{\alpha}{2p} ik\gamma. \tag{7.87}$$

This equation requires p to be pure imaginary number. In this case, the solution of the α-ω dynamo equation is an oscillating dynamo waves.

To get the critical dynamo number, we must consider the finite k/b. If we assume $k \ll b$, we have

$$I_{\frac{2k}{b}}(\zeta_0) \approx I_0(\zeta_0) - \frac{2k}{b} K_0(\zeta_0), \tag{7.88}$$

and

$$K_{2k}b(\zeta_0) \approx K_0(\zeta_0). \tag{7.89}$$

Therefore, A_0 is larger than the previous estimate by $-\frac{2k}{b} K_0(\zeta_0) \frac{\alpha\zeta_0}{4pI_1(\zeta_0)}$. Returning to the previous equation for p (equation (68)), we assume there exists a solution in which $|\zeta_0| \ll 1$, then

$$-\lambda_0 b \frac{1}{2} \left(1 - \frac{1}{2}\zeta_0^2 \ln\left(\frac{\zeta_0}{2}\right)\right) = -\frac{\alpha}{2p} \left(1 + \frac{2k}{b} \ln\left(\frac{\zeta_0}{2}\right)\right) ik\gamma. \tag{7.90}$$

To the first order approximation, we take $p = iC_1$, where C_1 is a real number. So we have the above equation can be changed to

$$-\lambda_b = -\frac{\alpha}{C_1} k\gamma. \tag{7.91}$$

And the constant C_1 can be expressed as $C_1 = \frac{\alpha k\gamma}{\lambda_0 b}$. And we also have

$$\frac{C_1}{\lambda_0 b^2} = \frac{k}{b} \frac{\alpha}{\lambda_0 b} \frac{\gamma}{\lambda_0 b} > 0. \tag{7.92}$$

The dynamo wave could exist in this case. Therefore, we have

$$\zeta_0^2 = \frac{4iC}{\lambda_0 b^2}. \tag{7.93}$$

And the value of $\ln\left(\frac{\zeta_0}{2}\right)$ is $\ln\left(\frac{\zeta_0}{2}\right) = \frac{i\pi}{4} + \ln\left(\frac{C}{\lambda_0 b^2}\right)$.

To do the second order approximation, we let $p = iC_1 + C_2$, where both C_1 and C_2 are real numbers. Since we are interested in the critical dynamo generation condition (p is purely imaginary), we can treat $C_2 \to 0$ in this approximation. Therefore we have:

$$\frac{C_2}{C_1} = -\frac{2C_1}{\lambda_0 b^2}\ln\left(\frac{C_1}{\lambda_0 b^2}\right) - \frac{k}{b}\frac{\pi}{2}. \tag{7.94}$$

In the critical situation, we have the real part of p approaches zero: $C_2 \to 0$, so that,

$$-\frac{2C_1}{\lambda_0 b^2}\ln\left(\frac{C_1}{\lambda_0 b^2}\right) = \frac{k}{b}\frac{\pi}{2}. \tag{7.95}$$

And the critical dynamo number $D_{crit} = \frac{C_1}{\lambda k b} = \frac{\alpha}{\lambda_0 b}\frac{\gamma}{\lambda_0 b}$ satisfies the following equation:

$$D_{crit} = \frac{\pi/4}{-\ln\left(\frac{k}{b}D_{crit}\right)} > 0. \tag{7.96}$$

In this case, the proper description for the critical condition for the generation of the α-ω dynamo is based on the effective thickness of the semi-conducting layer $1/b$, the characteristic turbulent velocity α, the magnitude of the vertical shear of the zonal winds, and the electrical conductivity in the outer boundary of the dynamo generation region. If the effective thickness of the layer $1/b$ is different from the meridional wave length $1/k$, the critical dynamo number for the exponentially varying conductivity profile ($D_{crit} = \frac{\alpha}{\lambda_0 b}\frac{\gamma}{\lambda_0 b}$) is different from the critical dynamo number for the constant conductivity case ($D_* = \frac{\alpha}{\lambda_0 k}\frac{\gamma}{\lambda_0 k}$). Notice this constraint for the dynamo number requires that $\frac{k}{b} \ll 1$. If $\frac{k}{b} \geq 1$, the correct dynamo number will be $D_* \sim 8\sqrt{2}$.

Here are some examples for the value of D_{crit} and D_* corresponding to different

k/b:

$$\frac{k}{b} = 0.01 \qquad D_{crit} = 0.12 \qquad D_* = 1200; \tag{7.97}$$

$$\frac{k}{b} = 0.04 \qquad D_{crit} = 0.15 \qquad D_* = 94; \tag{7.98}$$

$$\frac{k}{b} = 0.1 \qquad D_{crit} = 0.2 \qquad D_* = 20. \tag{7.99}$$

It is clear that the difference between D_{crit} and D_* is larger for the smaller value of k/b.

7.8 Conclusions and discussions

The descent of the probe from Galileo to Jupiter's atmosphere supports the idea that the zonal winds are the surface expression of the deep penetrating cylindrical flow. Busse (1976) suggests that the zonal flow is formed by the drifting convection column from the deep interior. From the observation of the magnetic field, it is clear that the magnetic field of the planets is varying on a thousand-year timescale. Therefore, the zonal flow in the deep interior must have small value. Otherwise, the magnetic field will not be stable and will produce much larger variation than observed field variation. Analogous to Earth, the cylindrical flow has to be truncated at the surface of the magnetic core. Outside of the magnetic core region, the interaction between the magnetic field and the zonal flow does not need to be taken into account. However, since Jupiter's conductivity profile is a smooth function instead of a step function, and the region of less conductivity is composed of fluid rather than solid, the magnetic core will not to be confined in the metallic core anymore. What is the definition for the metallic core? It is far from obvious. In this paper, we use two approaches to understand the definition of the magnetic core for the giant planet. The first approach is to study the electromagnetic effect produced by the semi-conducting hydrogen layer. In this case, we neglect the interaction between the magnetic field and the flow, and only consider the attenuation of the magnetic field produced by the screening effect. In combination with the observation of the magnetic field from the Galileo space-

craft and the Voyager spacecraft, and the shockwave experiments, we find the outer boundary of the dynamo generation region is at about $0.86R_J$. The conductivity of the outer boundary of the magnetic core corresponds to conductivity, which is three orders of magnitude less than that of a typical metal.

Second, we conduct a preliminary estimation of the influence of the flow to the magnetic field in the semi-conducting molecular hydrogen envelope. If the semi-conducting envelope contains zonal flows that are comparable to those observed in the atmosphere, then toroidal fields exceeding thousands of Gauss are easily generated. In the presence of modest conversion of toroidal to poloidal field (for example that predicted by an α-effect with amplitude suggested by convective motions), dynamo generation of field can occur at radii where the conductivity is many orders of magnitude below that of a metal. The fields generated in this region (and the magnetic Reynolds number that characterize their generation) are dictated by a length scale comparable to the scale height of the electrical conductivity, which is much smaller than the radius of the planet.

As a consequence of these two conclusions, we must expect significant currents and their associated magnetic fields and significant MHD fluid dynamical effects well outside the region of metallic or near metallic conductivity.

Bibliography

Abramowitz, M. and I. Stegun 1970. *Handbooks of Mathematical Functions* Dover Publication, Inc., New York, pp 358–359

Anderson J. D., J. K. Campbell, R. A. Jacobson, D. N. Sweetnam, and A. H. Taylor 1987. Radio science with Voyager 2 at Uranus - results on masses and densities of planet and five principle satellites. *J. Geophys. Res.* **92**, 14877–14833

Ashcroft, N. W. 1968. Metallic hydrogen - a high temperature superconductor. *Phys. Rev. Lett.* **21**, 1748–1749.

Atkinson, D. H., A. P. Ingersoll and A. Seiff 1997. Deep zonal winds on Jupiter: update of Doppler tracking the Galileo probe from the orbiter. *Nature* **338**, 649–650.

Atkinson, D. H., J. B. Pollack and A. Seiff 1998. The Galileo probe Doppler wind experiment: measurement of the deep zonal wind on Jupiter. *J. Geophys. Res* **103**, 22911–22928.

Aurnou, J. M., and M. H. Heimpel 2004. Zonal jets in rotating convection with mixed mechanical boundary conditions. *Icarus* **169**, 492–498.

Backus, G. E., R. H. Estes, D. Chinn and R. A. Langel 1987. Comparing the jerk with other global models of the geomagnetic field from 1960 to 1978 *J. Geophys. Res.* **92**, 3615–3622.

Burrows, A., M. S. Marley and C. M. Sharp 2000. The near-infrared and optical spectra of methane dwarfs and brown dwarfs. *Ap. J.* **531**, 438–446.

Busse, F. H. 1976. Simple model of convection in the Jovian atmosphere. *Icarus* **29**, 255–260.

Busse, F. H. 1983. A model of mean zonal flows in the major planets. *Geophys. Astrophys. Fluid. Dyn.* **23(2)**, 153–174.

Busse, F. H. 1994. Convection driven zonal flows and vortices in the major planets. *Chaos* **4**, 123–134.

Busse, F. H. 2000. Homogeneous dynamo in planetary cores and in the laboratory. *Ann. Rev. Fluid Mechanics* **32**, 383–408.

Campbell J. K. and S. P. Synnott 1989. Gravity field of the Jovian system from Pioneer and Voyager tracking data. *Astron. J.* **90**, 364–372

Campbell J. K. and J. D. Anderson 1989. Gravity field of the Saturnian system from Pioneer and Voyager tracking data. *Astron. J.* **97**, 1485–1495

Coe, R., M. Prevot and P. Camp 1995. New evidence for extraordinary rapid change of the geomagnetic field during a reversal. *Nature* **374**, 687–692.

Connerney, J. E. P., N. F. Ness and M. H. Acuna 1982. Zonal harmonic model of Saturn's magnetic field from Voyager 1 and 2 observations. *Nature* **298**, 44–46.

Connerney, J. E. P. 1993. Magnetic field of the outer planets. *J. Geophys. Res.* **98**, 18659–18679.

Courtillot, V., J. L. Le Mouel, and J. Ducruix 1984. On Backus' mantle filter theory and the 1969 geomagnetic impulse *Geophys. J. Roy. Astro. Soc.* **78**, 619–625.

Currie, R. G. 1967. Magnetic shielding properties of the Earth's mantle. *J. Geophys. Res.* **72**, 2623–2628.

Currie, R. G. 1968. Geomagnetic spectrum of internal origin and lower mantle conductivity. *J. Geophys. Res.* **73**, 2779–2783.

Davies M. E., V. K. Abalakin, M. Bursa, T. lederle, J. H. Lieske, et al. 1986. Report of the IAUIAG COSPAR working group on cartographic coordinates and rotational elements of the planets and satellites: 1985. *Celest. Mech.* **39**, 102–113.

Dessler, A. J. 1983. Coordinate systems. *Physics of the Jovian magnetosphere* Cambridge University Press, New York, pp. 498–504

Desch, M. D., and M. L. Kaiser 1981 Voyager measurement of the rotation rate of Saturn's magnetic field. *Geophys. Res. Lett* **8**, 253–256

Galopeau P. H. M. and A. Lecacheux 2000. Variation of Saturn's radio rotation period measured at kilometer wavelengths. *J. Geophys. Res.-Space Physics*, **105(A6)**, 13089–13101

Glatzmaier, G. A. 2005 A saturnian dynamo simulation. *American Geophysical Union Fall Meeting 2005, San Francisco, CA*

Guillot, T. 1999 A comparison of the interiors of Jupiter and Saturn. *Plan. Space Sci.*, **47**, 1183–1200

Guillot, T., D. J. Stevenson, W. B. Hubbard and D. Saumon 2004 The interior of Jupiter. *Jupiter: The Planet, Satellites and Magnetosphere* Cambridge University Press, New York, pp 35–57

Guillot, T. 2005. The interior of giant planets: Models and outstanding questions. *Annu. Rev.Earth Planet Sci.*, **33**, 493–530

Gurnett, D. A., et al. 2005. Radio and plasma wave observations at Saturn from Cassini's approach and first orbit. *Science* **307**, 1255–1259.

Heimpel, M., J. Aurnou and J. Wicht 2005. Simulation of equatorial and high latitude jets on Jupiter in a deep convection model. *Nature* **438**, 193–196

Hollerbach R. 2000. A spectral solution of the magnetoconvection equation in a spherical geometry. *Int. J. Num. Methods Fuilds* **32**, 773–797

Holmes, N. C., M. Ross and W. J. Nellis 1995. Temperature measurements and dissociation of shock-compressed liquid deuterium and hydrogen. *Phys. Rev. B* **59**, 15835–15845

Hubbard, W. B. 1968. Thermal structure of Jupiter. *Astrophys. J.* **152(3P1)**, 745–754.

Hubbard, W. B., W. J. Nellis, A. C. Mitchell, N. C. Holmes, S. S. Limaye, and P. C. McCandless 1991. Interior structure of Neptune - comparison with Uranus. *Science* **253**, 648–651.

Hubbard W. B., J. C. Pearl, M. Podolak and D. J. Stevenson 1995. The interior of Neptune. *Neptune and Triton* University of Arizona Press, Tucson, pp 109–138

Hubbard, W. B., T. Guillot, and J. I. Lunine 1997. Liquid metallic hydrogen and the structure of brown dwarfs and giant planets. *Phys. Plasmas.* **4(5)**, 2011–2015

Ingersoll, A. P. and J. N. Cuzzi 1969. Dynamics of Jupiter's cloud bands. *J. Atmos. Sci.* **26**, 981–985.

Ingersoll, A. P. and D. Pollard 1982. Motion in the interiors and atmosphere of Jupiter and Saturn -scale analysis, anelastic equations, barotropic-stability criterion. *Icarus* **52**, 62–80.

Ingersoll, A. P., R. F. Beebe, B. J. Conrath and G. E. Hunt 1984. Structure and dynamics of Saturn's atmosphere. *Saturn* University of Arizona Press, Tucson, pp 195–238

Ingersoll, A. P. 1990. Atmospheric dynamics of the outer planets. *Science* **248**, 308–315.

Ingersoll, A. P., C. D. Barnet, R. F. Beebe, F. M. Flasar, D. P. Hinson, S. S. Limaye, L. A. Sromovsky and V. E. Suomi 1995. Dynamic meteorology of Neptune. *Uranus.* University of Arizona Press, Tucson, pp 613–682.

Kaiser, M. L., et al. 1984. Saturn as a radio source. *Saturn* University of Arizona Press, Tucson, pp 378–415

Knittle, E. and R. Jeanloz 1986. High pressure metallization of FeO and implication for the Earth's core. *Geophys. Res. Lett* **13**, 1541–1544.

Knittle, E., R. Jeanloz, A. C. Mitchell and W. J. Nellis 1986. Metallization of $Fe_{0.94}O$ at elevated pressures and temperatures observed by shock-wave electrical resistivity measurements. *Sol. State. Comm.* **59**, 513–515.

Lay, T., Q. Williams and E. J. Garnero 1998. The core-mantle boundary layer and deep Earth dynamics. *Nature* **392**, 461–468.

Lindal G. F., G. E. Wood, G. S. Levy, J. D. Anderson, D. N. Sweetnam, et al. 1981. The atmosphere of Jupiter-an analysis of the Voyager ratio occultation measurements. *J. Geophys. Res.* **86**, 8721-8727

Lindal G. F., D. N. Sweetnam and V. R. Eshleman 1985. The atmosphere of Saturn-an analysis of the Voyager ratio occultation measurements. *Astron. J.* **90**, 1136-1146

Lindal, G. F. 1992 The atmosphere of Neptune - an analysis of radio occultation data acquired with Voyager 2. *Astron. J.* **103**, 967–982.

Magalhaes, J. A., A. Seiff and R. E. Young 2002. The stratification of Jupiter's troposphere at the Galileo probe entry site. *Icarus* **158**, 410–433

Manga M. and R. Jeanloz 2002. Implication of a mantle-bearing chemical boundary layer in D" for mantle dynamics *Geophys. Res. Lett* **23**, 3091–3094

Magro, W. R., D. M. Ceperley, C. Pierleoni, and B. Bernu 1996. Molecular dissociation in hot, dense hydrogen. *Phys. Rev. Lett* **76**, 1240-1243

Marley, M. S., P. Gomez and P. Podolak 1995. Monte Carlo interior models for Uranus and Neptune. *J. Geophys. Res.* **100**, 23349-23354

Marley M. S. and C. P. Mckay 1999. Thermal structure of Uranus' atmosphere. *Icarus* **138**, 268–286

McDonald, K. L. 1957. Penetration of the geomagnetic secular field through a mantle with variable conductivity. *J. Geophys. Res* **62**, 117–141

Mitchell A. C. and W. J. Nellis 1982. Equation of state and electrical-conductivity of water and ammonia shocked to the 100 GPA (1 MBAR) pressure range. *J. Chem. Phys.* **76(12)**, 6273-6281

Moffatt, H. K. 1978. *Hydromagnetic field generation in electrically conducting fluid* Cambridge University Press

Nellis, W. J., D. C. Hamilton, N. C. Holmes, H. B. Radousky, F. H. Ree, A. C. Mitchell and M. Nicol 1988 The nature of the interior of Uranus based on studies of planetary ices at high dynamic pressure. *Science* **240**, 779-781

Nellis, W. J., A. C. Mitchell, P. C. McCandless, D. J. Erskine and S. T. Weir 1992. Electronic energy gap of molecular hydrogen from electrical conductivity measurements at high shock pressures. *Phys. Rev. Lett.* **68**, 2937–2940

Nellis, W. J., M. Ross and N. C. Holmes 1995. Temperature measurements of shock-compressed liquid hydrogen: implication for the interior of Jupiter *Science* **269**, 1249–1252

Nellis, W. J., S. T. Weir and A. C. Mitchell 1996. Metallization and electrical conductivity of fluid hydrogen in Jupiter. *Science* **273**, 936–938

Nellis, W. J., S. T. Weir and A. C. Mitchell 1999. Minimum metallic conductivity of fluid hydrogen at 140 GPa (1.4 Mbar). *Phys. Rev. B.* **59**, 3434–3449

Pearl J. C. and B. J. Conrath 1991. The albedo, effective temperature, and energy balance of Neptune, as determined from Voyager data. *J. Geophys. Res. Suppl.* **96**, 18921–18929

Pelletier, J. D. 1999. Paleointensity variation of Earth's magnetic field and their relationship with polarity reversals. *Physics of the Earth and Planetary Interiors* **110**, 115–128

Podolak M., W. B. Hubbard and D. J. Stevenson 1991. Model of Uranus' interior and magnetic field *Uranus* University of Arizona Press, Tucson, pp 29–61

Podolak M, J. I. Podolak and M. S. Marley 2000. Further investigations of random models of Uranus and Neptune. *Planet. Space. Sci.* **48**, 143–151

Porco, C. C., et al. 2003 Cassini imaging of Jupiter's atmosphere, satellites and rings. *Science* **299**, 1541–1547

Porco, C. C., et al. 2005 Cassini imaging science: initial results on Saturn's atmosphere. *Science* **307**, 1243–1247

Roberts, P. H. and A. M. Soward 1992. Dynamo theory. *Ann. Rev.Fluid Mechanics* **24**, 459–512

Glatzmaier G. A. and P. H. Roberts 1995. A 3-dimensional convective dynamo solution with rotating and finitely conducting inner core and mantle. *Phys. Earth Planet. Inter.* **91**, 63–75

Russel, C. T., Z. J. Yu, K. K. Khurana and M. G. Kivelson 2001. Magnetic field changes in the inner magnetosphere of Jupiter. *Adv. Space Res.* **28(6)**, 897–902.

Russel, C. T., Z. J. Yu, K. K. Khurana and M. G. Kivelson 2001. Magnetic field changes in the inner magnetosphere of Jupiter. *Adv. Space Res.* **28(6)**, 897–902.

Russel, C. T., Z. J. Yu, K. K. Khurana, S. P. Joy and M. G. Kivelson 2001. Secular variation of the Jovian magnetic field from singular value decomposition analysis *American Astronomical Society, DPS meeting* **33**, 1097.

Saumon, D. and G. Chabrier 1992. Fluid hydrogen at high density: pressure ionization. *Phys. Rev. A.* **46**, 2084–2100

Saumon, D. and T. Guillot 2004. Shock compression of deuterium and the interiors of Jupiter and Saturn. *Astrophys. J.* **609**, 1170–1180

Shankland, T., J. Peyronneau and J. P. Poirier 1993. Electrical conductivity of the lower mantle *Nature* **366**, 453–455

Smith, E. J., L. Davis Jr. and D. E. Jones 1976. Jupiter's magnetic field and magnetosphere *Jupiter* University of Arizona Press, Tucson, pp 788–829

Smith, B. A. and G. E. Hunt 1976. Motions and morphology of clouds in the atmosphere of Jupiter. *Jupiter* University of Arizona Press, Tucson, pp 564-585

Stevenson D. J. and N. W. Ashcroft 1974. Conductions in fully ionized liquid-metals *Phys. Rev. A* **9(2)**, 782–789.

Stevenson D. J. and E. E. Salpeter 1976. Interior models of Jupiter. *Jupiter* University of Arizona Press, Tucson, pp 85–112

Stevenson D. J. and E. E. Salpeter 1977. The phase diagram and transport properties for hydrogen-helium fluid planets. *Astrophys. J. Suppl. Ser.* **35**, 221–237.

Stevenson D. J. 1982. Interiors of the giant planets. *Ann. Rev. Earth Planet Sci.* **10**, 257–295.

Taylor, G. I. 1923. Experiments on the motion of solid bodies in rotating fluids. *Proc. R. Soc. A* **104**, 213–218.

Tyler G. L., D. N. Sweetnam, J. D. Anderson, S. E. Borutzki and J. K. Campbell 1989. Voyager radio science observations of Neptune and Triton. *Science* **246**, 1466-1473.

Vasavada A. R. and A. P. Showman 2005. Jovian atmospheric dynamics: An update after Galileo and Cassini. *Rep. Prog. Phys.* **68**, 1935-1996.

Warwick J. W., D. R. Evans, J. H. Roming, C. B. Sawyer, M. D. Desch, et al. 1986. Voyager 2 radio observations of Uranus. *Science* **233**, 102–106.

Warwick J. W., D. R. Evans, G. R. Peltzer, R. G. Peltzer, J. H. Roming, et al. 1989. Voyager planetary radio astronomy at Neptune. *Science* **246**, 1498–1501.

Weir, S. T., A. C. Mitchell and W. J. Nellis 1996. Metallization of fluid molecular hydrogen at 140 Gpa. *Phys. Rev. Lett.* **76**, 1860–1863.

Wood, B. and J. Nell 1991. High temperature electrical conductivity of the lower mantle phase (MgFe)O *Nature* **351**, 309–311.

Young, R. E. 2003. The Galileo probe: How it has changed our understanding of Jupiter. *New Astron. Rev.* **47**, 1–51.

Zharkov V. N. and V. P. Trubitsyn 1976. Structure, composition, and gravitational field of Jupiter. *Jupiter* University of Arizona Press, Tucson, pp 133–175